

Ship detection products based on complex SAR data in TOPS mode

Marianne Myrnes

Master thesis in Energy, Climate and Environment, EOM-3901, June 2015

Abstract

With the increasing need for monitoring ship traffic in both coastal and open oceans, ship detection is an important application of synthetic aperture radar (SAR). This thesis investigates image products suitable for ship detection for complex data acquired in Terrain Observation by Progressive Scans (TOPS) mode.

The research was based on studying how contrast enhancement algorithms suitable for SLC data is adaptable to complex data acquired in TOPS mode. Secondly it investigated if by processing the TOPS raw data with a different focusing scheme had any affect on the image product. The evaluation of image products were done by well known contrast measurements such as peak to clutter ratio (PCR) and target to clutter ratio (TCR). The speckle content was measured by the coefficient of variation (CV). The improved subaperture cross-correlation (SCM) algorithm developed by Brekke et al.[1] was extended to fit the dual polarization case of Sentinel-1 IW mode. The polarimetric extension was based on the full polarimetric SCM extension proposed by Souyris et al.[2]. Single, and dual polarization SCM algorithms were compared to the Polarimetric whitening filter and Aegir-Pol. Aegir-Pol is a polarimetric fusion between co-pol and cross pol widely used by the Norwegian Defence Research Establishment. Kongsberg Spacetec Near Real Time (NRTSAR) processor was used to focus TOPS raw data. The focusing was done with various bandwidths and window weighting functions.

The results showed that all contrast enhancement algorithms were adaptable to SLC data in TOPS mode. SCM processed for the VH channel and for the polarimetric extension yielded best image products in terms of TCR and PCR. In this relation a small overlap between the subapertures is needed. The SCM image products experienced a minor increase in TCR and PCR with increasing focusing bandwidth and the choice of window function had most effect on TCR and PCR considering the shortest bandwidth. NRTSAR focused TOPS SLC data with maximum overlap between azimuth bursts. Using this area as an alternative subaperture was investigated, but no observation of improved CV was observed.

Acknowledgements

Working with this Master thesis has been an enriching ending of my student career in the EKM programme.

First I would like to thank Kongsberg Spacetec AS for providing me with an office and a friendly working environment. In this relation I must thank for the extreme amounts of coffee consumed and lastly for giving me the opportunity to work with a very interesting project.

A special thanks goes to my supervisors; Stian Normann Anfinsen, Lars-Petter Gjøvik and Ole Morten Olsen. Thank you for your contagious enthusiasm and for sharing your knowledge. Thank you for reading through my thesis and for giving me advice. I am very grateful for the opportunity to work with NRTSAR and all your help and assistance are very much appreciated.

Thank you, Camilla Brekke, for sharing your work with the SCM algorithm, for reading through my thesis and for giving me advice.

To the wonderful girls at EKM 09 including Martine, thank you. Long hours at the study hall would not have been bearable without you. Especially Tina and Kirsti, the memories of our adventure to Hong Kong are hidden in my heart.

To my family, thank you for your love and encouragement and for always being there for me. Last, but not least, to my dear Kristoffer, thank you for your patience and support throughout my study career, late dinners and for always making me smile.

*Marianne Myrnes
Tromsø, May 2015.*

Contents

Abstract	i
Acknowledgements	iii
List of Figures	ix
List of Tables	xiii
List of Abbreviations	xv
1 Introduction	1
1.1 Motivation and contribution	3
1.2 Objectives	4
1.3 Structure of thesis	5
2 Synthetic Aperture Radar	7
2.1 Basic Principles of imaging radars	8
2.1.1 Imaging geometry	8
2.1.2 Resolution	8
2.2 SAR processing	11
2.3 SAR processing algorithms	14
2.3.1 The Range Doppler Algorithm	14
2.3.2 The ω_k Algorithm	16
2.3.3 The Chirp-scaling Algorithm	17
2.4 Speckle	17
2.5 Scattering	18
2.5.1 Surface scattering	18
2.5.2 Double bounce scattering	19
2.5.3 Bragg scattering	19
2.5.4 Volume scattering	19
2.6 Radar Cross Section	20
2.7 Polarization	20
2.7.1 Scattering matrix	21

3	Terrain Observation by Progressive Scans	23
3.1	ScanSAR	24
3.1.1	ScanSAR acquisition	25
3.1.2	Scalloping	25
3.1.3	ScanSAR resolution	26
3.2	TOPS	27
3.2.1	TOPS acquisition	28
3.2.2	TOPS resolution	29
3.2.3	TOPS focusing	30
3.3	Kongsberg Spaceteq Near Real Time processor	34
3.3.1	Impulse Response	35
3.3.2	Window functions	36
3.3.3	Bandwidth	37
3.4	TOPS Deramping	38
3.4.1	Results deramping TOPS data with ESA IPF and NRT-SAR	40
4	Ship detection	45
4.1	SAR imaging of the ocean	46
4.1.1	SAR imaging of Ships	47
4.2	Contrast Measures	48
4.2.1	Target to clutter ratio	48
4.2.2	Peak to clutter ratio	48
4.2.3	Coefficient of variation	48
4.3	Constant False Alarm Rate	49
4.3.1	Sea clutter statistics	49
4.4	Subaperture cross-correlation magnitude	51
4.4.1	Algorithm 1: Subaperture Cross-correlation Magnitude	54
4.5	Polarimetric contrast enhancement methods	57
4.5.1	Algorithm 2: Polarimetric subaperture cross-correlation magnitude	57
4.5.2	Algorithm 3: Polarimetric whitening filter	60
4.5.3	Algorithm 4: Aegir with fusion of polarimetric channels	61
4.6	Ship detection adaption to Sentinel-1 TOPS mode	61
4.6.1	Ship detection in TOPS mode overlap regions	62
4.6.2	NRTSAR Processing parameters	63
4.6.3	TOPS Dwell time	63
5	Data	65
5.1	Sentinel-1 acquisition modes	65
5.2	Data formats	68
5.3	Scenes	68
5.4	Subimages for subaperture cross correlation magnitude analysis	71

6	Results and Discussion	75
6.1	Experiment 1: Performance analysis of subaperture processing with TOPS SLC data focused by ESA IPF.	76
6.1.1	Dual polarization subaperture cross-correlation magnitude	76
6.1.2	Contrast and speckle measures	77
6.1.3	Contrast and speckle measurements for subimage no. 1	78
6.1.4	Contrast and speckle measurements for subimage no. 11	83
6.1.5	Prewhitening of the subapertures	87
6.1.6	Dwell time and center time difference between subapertures.	91
6.1.7	Summary of performance analysis of subaperture processing with TOPS data from ESA IPF.	93
6.2	Experiment 2: Comparison of image products obtained from TOPS SLC data.	94
6.2.1	Dual polarization PWF	94
6.3	Experiment 3: Performance analysis of subaperture processing with TOPS data, focused by NRTSAR.	101
6.3.1	Comparison of subaperture image products focused by NRTSAR with varying processing bandwidth and Hamming window coefficients.	104
6.4	Experiment 4: Comparison of image products obtained from TOPS SLC data focused by NRTSAR, with varying Hamming window coefficients and focusing bandwidths	108
6.5	Experiment 5: Investigation of azimuth burst overlap in TOPS SLC IW3 data.	110
6.5.1	Azimuth burst overlap acquired from focusing with ESA IPF and NRTSAR	110
6.5.2	Subaperture cross correlation magnitude on overlap subimages	112
6.5.3	Speckle measurements in overlap area	114
7	Conclusions	119
7.1	Further work	121
	Bibliography	123
8	Appendix	129
8.1	Graphical representation of the correlation between the time-frequency support and aquisition geometry, TOPS	129
8.2	Target to clutter ratio and peak to clutter ratio computed with target vectors from Pauli baseses	131

8.3	Subaperture cross correlation magnitude impact of varying processing bandwidth and Hamming window coefficient. . .	133
-----	--------------------------------------------------------------------------------------------------------------------	-----

List of Figures

1.1	High level ship detection flow chart	2
2.1	SAR geometry of side-looking radar with squint angle, adapted figure from [12].	9
2.2	Range cell migration of a single target in 2D processor memory	13
2.3	SAR Focusing algorithms, Range Doppler Algorithm(RDA), $\omega - k$ Algorithm and Chirp Scaling Algorithm (CSA). Image adapted from [12]	14
2.4	Speckle, Random walk in 2D [16].	17
2.5	Dihedral scattering/corner reflection. Figure taken from [17]	19
3.1	ScanSAR imaging geometry with three sub-swaths	24
3.2	Azimuth time/frequency support for raw data in ScanSAR	26
3.3	TOPS imaging geometry, V_S : velocity of satellite [19].	27
3.4	Reduction of azimuth resolution compared to SPOT imaging mode	28
3.5	Azimuth time and doppler frequency relation in TOPS mode.	29
3.6	TFD support for TOPSAR data	30
3.7	Sentinel-1 SLC Processing Algorithm [19]	32
3.8	NRTSAR and ship detection flow chart. <i>Kongsberg Spacetec, All Rights Reserved</i>	34
3.9	Impulse response from a single point target	35
3.10	Azimuth frequency spectrum before and after the deramping procedure [32].	39
3.11	Deramping SLC product focused by ESA IPF,	41
3.12	Deramping SLC product focused by ESA IPF	42
3.13	Deramping SLC product focused by NRTSAR	43
4.1	Illustration of the devision of subapertures from the azimuth spectrum	52
4.2	Illustratopm of the correlation process for coherent targets and sea	53
4.3	flowchart of the SCM algorithm	55

4.4	Extraction of subapertures from the azimuth frequency spectrum	56
4.5	Overlap area of two successive bursts in azimuth	62
5.1	Acquisition modes for Sentinel-1, image from [59]	66
5.2	Three subswaths with six burst, IW mode	67
5.3	Background	71
5.4	Amplitude images of VV channel representing subimage no.1 and 12	72
5.5	Amplitude images of VV channel representing subimage no.15 and 18	72
6.1	VH and VV channel of subimage no. 1	80
6.2	CV for subimage no. 1	80
6.3	TCR for subimage no. 11.	81
6.4	PCR for image no. 11.	81
6.5	Subimage no. 1, original VH image and normalized surface plot.	82
6.6	Subimage no 1, SCM-VH image and normalized surface plot.	82
6.7	VH and VV channel of subimage no. 11.	84
6.8	CV for subimage no. 11.	84
6.9	TCR for subimage no. 11.	85
6.10	PCR for subimage no. 11	85
6.11	Original subimage no. 11, VH channel and normalized surface plot	86
6.12	Subimage no. 11, SCM-POL image and normalized surface plot	86
6.13	Prewhitening procedure in SCM algorithm.	87
6.14	PCR for prewhitened subimage no. 1	89
6.15	Cv for prewhitened subimage no. 1	89
6.16	PCR for prewhitened subimage no. 11	90
6.17	CV for prewhitened subimage no. 11	90
6.18	TCR and window sizes for PWF algorithm	95
6.19	PCR and window sizes for PWF algorithm	96
6.20	Polarimetric Whitening filter and Aegir-Pol results for subimage no 1	98
6.21	Original VH amplitude image and SCM-VH	98
6.22	Polarimetric whitening filter and Aegir-Pol result for subimage no. 11	99
6.23	Original VH aplitude image and SCM-VH for subimage no. 11	99
6.24	Surface plot of PWF and Aegir-POL, subimage no. 11	100
6.25	Outline of bandwidth and Hamming window coefficient options chosen for focusing with NRTSAR	102
6.26	Hamming windows with different coefficients	102
6.27	Comparison of CV from SCM computed for subimage no. 1	103

6.28	Comparison of PCR computed for subimage no. 1	104
6.29	SCM for subimage no. 18, NRTSAR, HWC 0.5 and varying focusing bandwidths	105
6.30	PCR for SCM images obtained from subimage no. 13, fixed bandwidth 314 Hz, varying HWC	106
6.31	PCR for SCM images obtained from subimage no. 13, fixed bandwidth 340 Hz, varying HWC	107
6.32	NRTSAR, Overlap, Burst no. 2 and 3 from TOPS SLC IW3 . .	111
6.33	ESA IPF, Overlap, Burst no. 2 and 3 from TOPS SLC IW3 . .	111
6.34	Overlap area of burst no. 2 and subimage area	112
6.35	Overlap area of burst no. 3 and subimage area	112
6.36	Combinations of subaperture extractions in overlap area . .	114
6.37	CV measurements from overlap subimage no. 1	115
6.38	CV measurements from overlap subimage no. 2	116
6.39	CV measurements from SCM-VV computations in overlap area	117
6.40	Intensity profile in azimuth SCM-VV	117
8.1	Graphical representation of the correlation between figure 3.3 and 3.5	130
8.2	Peak to clutter ratio computed with target vectors from Pauli bases	131
8.3	Target to clutter ratio computed with target vectors from Pauli bases	132

List of Tables

3.1	Hamming window coefficients for each subswath, TOPS IW, ESA IPF	37
3.2	Hamming window coefficients, IRW, PSLR and ISLR measured from point target analysis, ESA IPF	37
3.3	Processing bandwidth for each subswath in ESA IPF	38
5.1	System parameters for Sentinel-1, table is adapted from [60]	66
5.2	Details for Sentinel-1 acquisition modes, table is adapted from [60]	67
5.3	System details for scenes covering the Norwegian sea	69
5.4	System parameters for scenes covering Bremerhaven, Germany and Portsmouth, England. The table show details for both SLC format and raw format, Sentinel-1 IW mode. Details taken from metadata of each product. Images retrieved from ESA's Sentinel-1 Scientific Data Hub [62]	70
5.5	Dimension details for Dataset 1.	73
6.1	TCR and PCR measurements for the SCM algorithms	78
6.2	SCM with prewhitening, TCR and PCR results	88
6.3	Dwell time and time difference between subapertures	92
6.4	TCR and PCR measurements for SCM, PWF, and Aegir-Pol	97
6.5	Bandwidths used in azimuth focusing with NRTSAR	101
6.6	Maximum values of TCR and PCR when using the Aegir-POL algorithm, representing the three selected subimages. HWC represents the Hamming window coefficient	109
6.7	Maximum values of TCR and PCR when using the PWF algorithm, representing three selected sub-images. HWC represents the Hamming window coefficient	109
8.1	SCM evaluation Hamming window coefficient and bandwidth	133
8.2	Aegir-POL, TCR and PCR when varying Hamming window coefficient and bandwidth, representing subimage 1.	133
8.3	PWF, TCR and PCR when varying Hamming window coefficient and bandwidth, representing subimage 1.	133

8.4	Subaperture cross correlation magnitude, PCR and TCR when varying Hamming window coefficient and bandwidth, representing subimage 13.	134
8.5	Aegir-Pol, PCR and TCR when varying Hamming window coefficient and bandwidth, representing subimage 13.	134
8.6	PWF, PCR and TCR when varying Hamming window coefficient and bandwidth, representing subimage 13.	134
8.7	Subaperture cross correlation magnitude, TCR and PCR when varying Hamming window coefficient and bandwidth, representing subimage 18.	135
8.8	Aegir, TCR and PCR when varying Hamming window coefficient and bandwidth, representing subimage 18.	135
8.9	PWF, TCR and PCR when varying Hamming window coefficient and bandwidth, representing subimage 18.	135

List of Abbreviations

AAP	Azimuth Antenna Pattern
CCF	Cross-Correlation Function
CFAR	Constant False Alarm Rate
ESA	European Space Agency
EW	Extra Wide swath mode.
HWC	Hamming Window Coefficient
GRD	Ground Range Detected
IPF	Instrument Processing Facility
IRW	Impulse Response Width
ISLR	Integrated sidelobe ratio
ISP	Instrument Source Packet
IW	Interferometric Wide swath mode.
NDRE	Norwegian Defence Research Establishment
NRTSAR	Near Real Time Synthetic Aperture Radar
PCR	Peak to Clutter Ratio
RCMC	Range Cell Migration Correction
PDF	Probability Density Function
PSLR	Peak to Sidelobe Ratio
SAR	Synthetic Aperture Radar
SCM	Subaperture Cross-correlating Magnitude
SLC	Single Look Complex
SLI	Single Look Intensity
SRC	Secondary Range Compression
TCR	Target to clutter ratio
TOPS	Terrain Observation by Progressive Scans



Introduction

In our increasingly globalized society, the demand for global trade have caused the ship traffic to grow in the world's oceans [3][4]. Considering the High North, the Arctic sea ice decline make the Northeast passage a possible busy shipping route in the future. This prediction is supported by the proposed oil and gas projects in the Barents Sea which raise the risk of oil pollution in our coastal areas.

With the increasing need for monitoring ship traffic in both coastal and open oceans, ship detection is an important application of synthetic aperture radar (SAR). SAR is operational day and night regardless of weather conditions. This makes it possible to observe and gather valuable information from areas which are hazardous and hard to reach physically. Considering the marine environment, piracy, illegal fishing and smuggling are among other international issues that SAR contribute to combat.

This thesis investigates the ship detection possibilities for the recently launched Sentinel-1 satellite. Sentinel-1 is the first in a family of six Sentinel satellites that are currently being developed by the European Space Agency (ESA) for the specific needs of the Copernicus program [5]. The main goal of the program is to provide information with importance to climate change, environmental politics, ocean surveillance, research and safety [6] [7].

A high level outline on the process of ship detection is shown in figure 1.1. In general, ship detection algorithms produce an output with a list of possible

target positions. In the process, parameters such as ship size, speed and heading are normally also produced. This output is then *manually* inspected by operators to separate out the actual ships from false alarms. This thesis will consider the orange box, which is a pre-processing stage of ship detection. Here the goal is to produce an image with enhanced ship to sea contrast which in turn lowers the rate of false alarms.

The utilities of Sentinel-1 images for maritime surveillance has been done by the European Commission [8]. The report points out the need for improvement of the existing automatic ship detection algorithms to better deal with false alarms. An improved ship detection algorithm in terms of false alarms means that less personnel are required for manual discrimination, and thus both time and cost expenditure will decrease.

In the case of emergencies, fast detection is crucial in order to alert coastguards and rescue units. Wide area coverage is also important in order to get a global perspective. Downlink and processing of large SAR images, which are used in ship detection, may take several hours. Therefore attention should be paid to improve both the processing schemes of SAR images and ship detection algorithms. The following chapters evaluate existing ship detection algorithms especially in terms of their suitability of Sentinel-1 data. In addition it enters into the processing of Sentinel-1 data, and compares the ship to ocean contrast in images processed by two different focusing schemes.

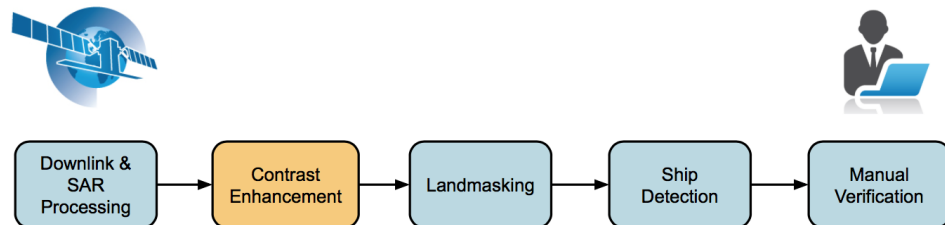


Figure 1.1: High level ship detection flow chart, elements in the figure are taken from [9]

1.1 Motivation and contribution

Sentinel-1 delivers SAR images to operational services including maritime surveillance systems. Two of the sensor modes provide images with a wide area coverage. These are the Interferometric Wide swath mode (IW), and the Extra Wide swath mode (EW). For wide swath imaging over ocean areas, Sentinel-1 uses the newly proposed TOPS (Terrain Observations with Progressive Scans) mode instead of the conventional ScanSAR mode. Sentinel-1 data are provided in single-look complex (SLC) format with access to phase information as well as the magnitude of the SAR backscatter signal. Previously SLC data have been a rare commodity in the setting of operational maritime surveillance. This is partly because there has not been available sensor modes supporting a combination of SLC data and wide coverage. In the cases where complex data have been relevant, it has been limited from operational services by high cost.

Sentinel-1 provides routine daily acquisitions and The Copernicus program makes a great amount of satellite data available to all users, including SLC data and unprocessed raw data. This makes it possible to perform thorough analysis and validation of ship detection on SLC data on a variety of ocean conditions. To the authors knowledge, no validation on ship detection for TOPS SLC data is done before. In Haram *et al* [8] the use of SLC data is not assessed in detail and they mention that the potential for ship detection on SLC products needs further validation.

Referring to the third box in figure 1.1, a ship detection algorithm usually needs a land mask to prevent false detections on land. The land mask is built from external coastline maps, that have limited accuracy. Haram *et al* [8] points out that SLC images have an advantage over Ground Range Detected (GRD) products. In SLC images it is possible to compute the complex coherency, which is expected to be different over land and sea. This can be utilized to produce more accurate land masks.

The availability of unfocused raw data opens up the possibility to improve and design processors which can be tuned to satisfy desired SAR applications. In relation of ship detection it is first of all processing speed, resolution and contrast between ship and ocean that can be influenced. This thesis describes the focusing scheme used by ESA, *Instrument Processing Facility* (IPF) to produce TOPS SLC images, and summarizes the alternative processing algorithms existing in the literature. Raw data are focused by Kongsberg Spacotec Near Real Time (NRT) processor. This processor focuses data at near real time and makes blocks of processed data available during downlink. Hereafter it will be denoted as NRTSAR. This means that the ship detection can be executed simultaneous with data reception, and before complete data products have

been finalized. In this thesis adjustments of processing parameters have been done to evaluate the adaption to ship detection.

1.2 Objectives

The overall goal of this thesis is twofold. First it is to investigate how contrast enhancement algorithms used in ship detection is suitable for complex data acquired in TOPS mode. In this relation we want to evaluate the output of these algorithms as products suitable for ship detection. This is done by examining speckle and contrast measurements. Secondly we want to investigate if by processing the TOPS raw data with a different focusing scheme with adjustable focusing bandwidth and weighting function will affect the performance of the algorithms.

The specific aim is to:

- investigate improvements of the existing SCM algorithms, and the possibility of a data fusion of the available polarizations VV and VH.
- evaluate the TOPS SLC dwell time and possible limitations of the SCM algorithm regarding the sea decorrelation time.
- evaluate existing and adjusted SCM algorithms by contrast measures such as target to clutter ratio (TCR) and peak to clutter ratio (PCR).
- compare the SCM images against other contrast enhancement products, were algorithms suitable for complex data is used.
- evaluate TCR and PCR for various sizes of subapertures and different sea states.
- evaluate TOPS SLC data processed by NRTSAR with adjustable processing parameters such as window function and bandwidth.
- investigate if by utilizing azimuth burst overlap in TOPS SLC in subaperture processing will give higher TCR and PCR

1.3 Structure of thesis

- Chapter two presents basic SAR theory, including imaging geometry, resolution, polarization and data processing.
- Chapter three is divided into two main parts. The first part presents the ScanSAR mode and TOPS mode, where there is an emphasis on the data focusing. The second part introduces the processor of Kongsberg Spacetec, and describes the adjustable processing parameters. Lastly the TOPS deramping procedure is explained. A discussion of the deramping performed in the experimental part is also included.
- Chapter four describes the theory of SAR imaging of ocean and ship detection. Here, the emphasis is on subaperture ship detection algorithms, and other algorithms suitable for complex data, such as the Polarimetric Whitening filter PWF.
- Chapter five presents the data used in the experimental part.
- Chapter six starts by describing each analysis, followed up by the results and a discussion of the analysis, respectively.
- Chapter seven concludes the findings in this thesis, and gives suggestions about future work.

/2

Syntetic Aperture Radar

Remote sensing consists of two basic processes; recording and analyzing measurements of objects and surfaces that the instruments have not been in physical contact with. The data are collected by utilizing the properties of electromagnetic waves. Electromagnetic waves carry information about their source and surroundings both when propagating in vacuum and through a medium. This information can be encoded in the wave *frequency, phase, intensity* and *polarization* [10].

In satellite remote sensing one distinguishes between two overall classes of sensor systems; passive and active. The passive system only collects radiation from external sources, while active systems have sensors that both generate and detect electromagnetic pulses [11].

Synthetic aperture radar (SAR) belongs to the family of active sensors that operates in the microwave region of the electromagnetic spectrum with wavelengths from 1 mm to 1m, or frequencies from 3×10^8 to 3×10^{11} Hz. The atmosphere is largely transparent to microwaves, which makes SAR operational around the clock in all weather conditions. SAR sensors were developed in the 1950s for military purposes, but the first civilian spaceborne SAR, SeaSAT was launched in 1978 with the objective of achieving higher spatial resolution and larger coverage than previous airborne imaging radars [12].

This chapter gives a brief introduction to remote sensing and SAR. First some basic principles regarding geometry, resolution and signal processing is ex-

plained. Three relevant processing algorithms are introduced before moving on to different scattering mechanisms and polarization.

2.1 Basic Principles of imaging radars

A radar system transmits coherent EM pulses towards a surface area of interest. Depending on the surface properties, some of the energy in the radar pulse is then backscattered towards the sensor. The sensor receives information from a target as long as it is within the *footprint*, which is the oval shaded area in figure 2.1 [10].

2.1.1 Imaging geometry

Figure 2.1 shows a typical side-looking radar instrument. The along-track direction is called *azimuth*, which is parallel to the velocity vector of the sensor. *Range* is the direction in which the EM pulses are transmitted. The distance from the radar to the point target on the ground is called *slant range* R , while the projected distance on the ground is named *ground range*.

The incidence angle θ_i is the angle between the radar beam and ground surface normal vector. This angle increases when moving across the swath from near to far range. The look angle θ_{look} is the angle between the nadir and the near range. R is the distance from the sensor to the target. For the zero squinted case, i.e, when looking perpendicular to the flight direction, this resembles to R_0 , which is the closest distance from the sensor and the target. The shaded oval area on the ground is referred to as the beam *footprint* and is related to the antenna beam pattern and the sensor/Earth geometry. The θ_{squint} describes the beam pointing direction.

2.1.2 Resolution

One pixel in a radar image represents a resolution cell, which is a limited area on the ground. Within this resolution cell the backscatter coefficients are added and stored as a value. The stronger the signal received from the resolution cell, the greater the pixel value [11]. Spatial resolution identifies the smallest square distance that two points on the ground can have and still be separated by the sensor. [11]. Considering radar systems, the spatial resolution differs in azimuth and range direction.

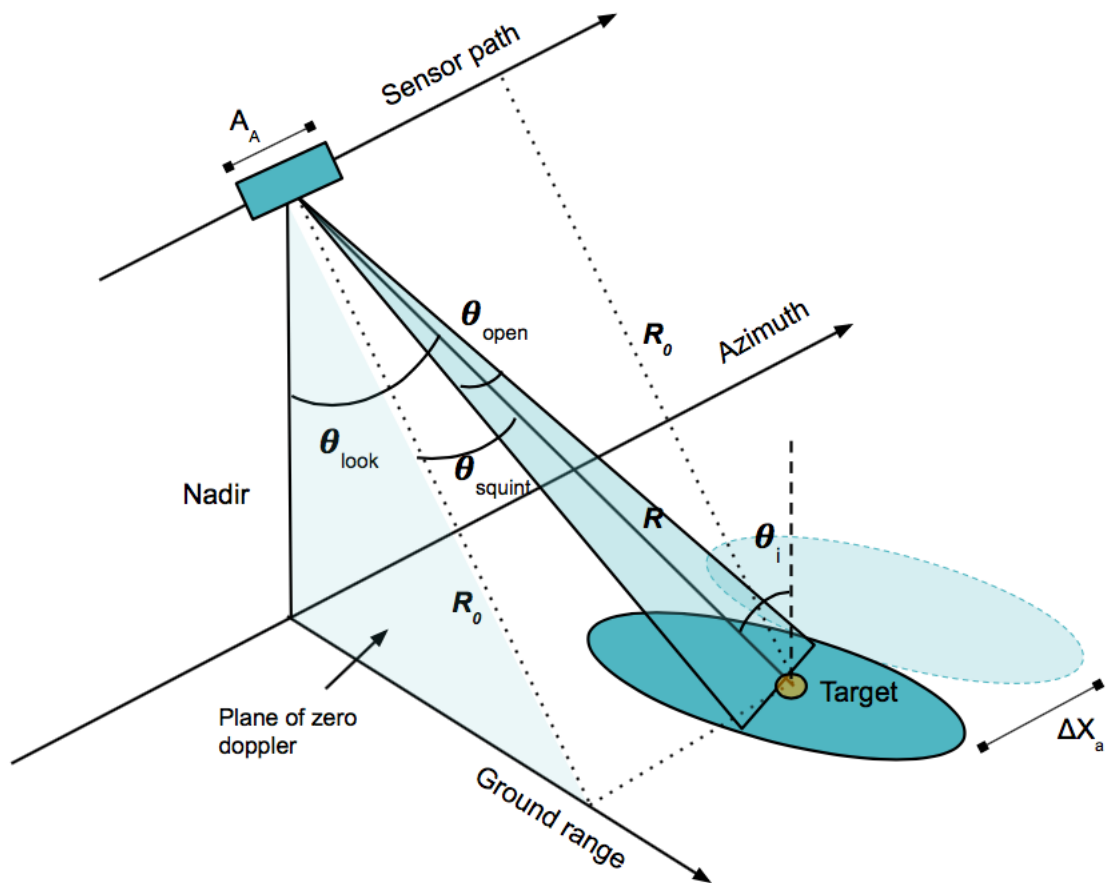


Figure 2.1: SAR geometry of side-looking radar with squint angle, adapted figure from [12].

2.1.2.1 Resolution in range

The length of the pulse emitted defines the resolution in range:

$$\Delta R_r = \frac{c}{2} \tau_p, \quad (2.1)$$

where τ_p is the pulse length and c is the speed of light. When converted to ground range, the resolution is defined as:

$$\Delta x_r = \frac{\Delta R_r}{\sin \theta_{look}}, \quad (2.2)$$

where θ_{look} is the look angle shown in figure 2.1. From these equations it is clear that shorter pulse length gives better ground range resolution. To save energy needed by the transmitter and to avoid reducing the pulse length, the transmitted pulse is frequency modulated by a dispersive filter, resulting in a so called *chirp* pulse. When the signal is received, compression is done by an inverse dispersive filter and thus giving an effective pulse length $\tilde{\tau}_p = \frac{2\pi}{\Delta\omega}$, which is shorter than the original pulse length τ_p (reduced from microseconds to nanoseconds) and is dependent on the bandwidth $\Delta\omega$. The larger bandwidth, the better resolution in range:

$$\Delta \tilde{R}_r = \frac{c}{2} \tilde{\tau}_p, \quad (2.3)$$

where $\tilde{\tau}_p$ is the effective pulse length and $\Delta \tilde{R}_r$ is the range resolution obtained with a chirp pulse, while c is the speed of light.

2.1.2.2 Resolution in azimuth

Considering a *real aperture radar*, the spatial resolution in azimuth is given by the footprint size and the distance to the object R :

$$\Delta x_a = R \theta_{open} = R \frac{\lambda}{A_A}, \quad (2.4)$$

where θ_{open} is the opening angle, A_A is the antenna length, and Δx_a is also known as the synthetic aperture length. This implies that in order to separate two targets, they can not exist in the same footprint. For satellites the distance to the target can be relatively large, and thus one has to synthesize a larger antenna to obtain a good resolution, hence the name SAR. The synthesizing is done by utilizing the *Doppler shift* introduced by the relative velocity of the

sensor and the target. In azimuth the received signal from one point target is built up of many pulses and the synthetic aperture radar (SAR) uses the so called Doppler shift history of the echoes to separate the surface pixels. The received signal from a point target P will have a positive Doppler shift as the radar beam approaches P . The Doppler shift will decrease to zero, and become negative as the point scatter leaves the beam. Neighboring targets will have Doppler histories that are replicas of P but shifted in azimuth time τ [11]. This method makes the resolution independent of the distance to the target and it is only given by the antenna length A_A :

$$\Delta\tilde{x}_a = \frac{A_A}{2}. \quad (2.5)$$

2.2 SAR processing

As mentioned earlier the transmitted pulse is a chirp signal. The chirp signal is a linear frequency modulated (FM) signal. This means that the instantaneous frequency f of the signal is a linear function of time. The transmitted pulse can be defined as [12]:

$$s(t) = \text{rect}\left(\frac{t}{T}\right) \exp\{j\pi Kt^2\}, \quad (2.6)$$

where

$$\text{rect}\left(\frac{t}{T}\right) = \begin{cases} 1 & \text{if } \left|\frac{t}{T}\right| \leq \frac{1}{2} \\ 0 & \text{otherwise} \end{cases},$$

and t is the time in seconds, K is the linear FM rate in Hertz per second, and T is the pulse duration in seconds. The phase $\phi(t)$ is given by the exponential term $\phi(t) = \pi Kt^2$, and the instantaneous frequency f is the derivative with respect to time:

$$f = \frac{1}{2\pi} \frac{d\phi(t)}{dt} = Kt \quad (2.7)$$

which means that the frequency is a linear function of time t with slope K .

After interacting with the surface, the backscattered signal from one point target, referred to as the *raw data*, can be described in two dimensions by azimuth time τ and the range time τ_r as:

$$s_R(\tau_r, \tau) = A_0 \omega_r \left(\tau_r - \frac{2R(\tau)}{c} \right) \omega_a(\tau - \tau_c) \exp \left\{ -j \frac{4\pi f_0 R(\tau)}{c} \right\} \\ \times \exp \left\{ j\pi K_R \left(\tau_r - \frac{2R(\tau)}{c} \right)^2 \right\} \quad (2.8)$$

where

- A_0 : a complex constant
- τ_r : range time
- τ : azimuth time reference to the closest approach
- τ_c : beam center offset time
- ω_r : range envelope - rectangular function
- ω_a : azimuth envelope - sinc-squared function
- f_0 : radar center frequency
- K_r : range chirp FM rate
- $R(\tau)$: the instantaneous slant range

Equation 2.8 represents the *demodulated baseband* signal received from a point target. This means that in range the signal is now at baseband, but in azimuth the signal may have a nonzero center frequency, denoted as the Doppler centroid frequency f_{ac} .

The reason that the nonzero center frequency occurs azimuth is because of the already mentioned Doppler shift. This is an overall small effect, but it is very noticeable when observed in the azimuth direction, which makes it fundamental in azimuth processing [12]. The red dots in figure 2.2 show the azimuth and range extent of a signal received from a single point target stored in a two-dimensional *raw data* memory. Seen from figure 2.2, the target responses have a displacement in range, called range cell migration (RCM). RCM occurs because as the sensor moves in azimuth the range to the target varies with azimuth time. The relationship between range distance and azimuth time is defined in equation 2.9.

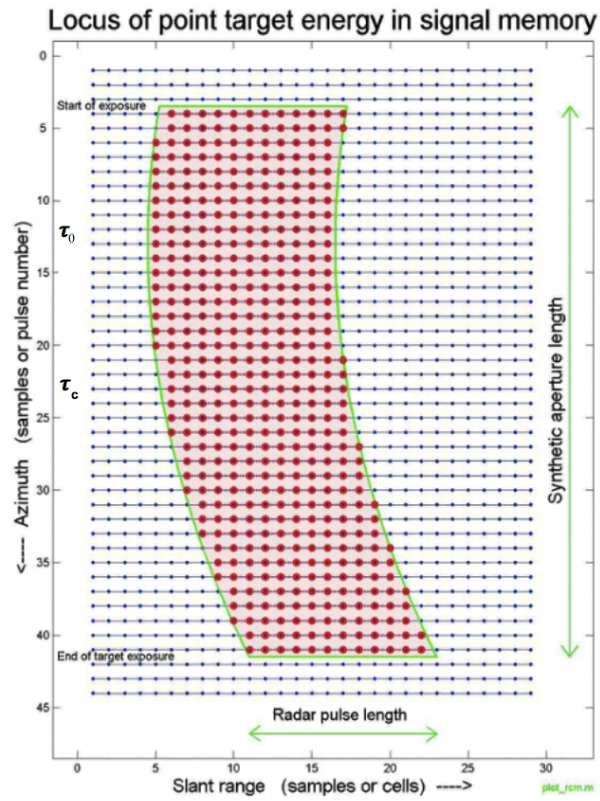


Figure 2.2: Range cell migration of a single target in 2D processor memory, τ_c : beam center crossing time, τ_0 : zero Doppler. Image taken from [12]

2.3 SAR processing algorithms

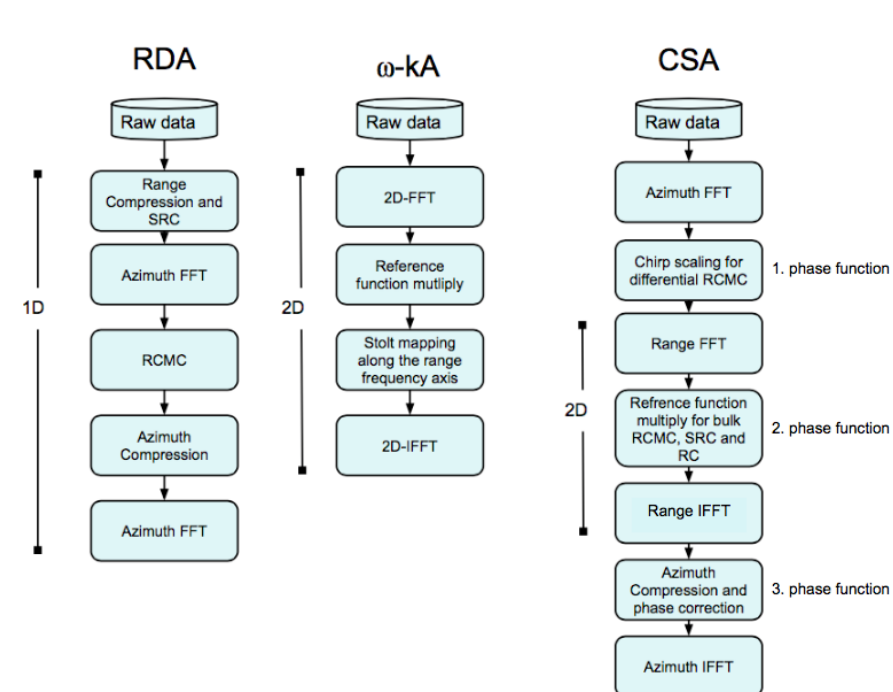


Figure 2.3: SAR Focusing algorithms, Range Doppler Algorithm(RDA), $\omega-k$ Algorithm and Chirp Scaling Algorithm (CSA). Image adapted from [12]

In the next sections three different processing schemes used on Stripmap SAR are briefly introduced. The details of each algorithm are complex and a complete description out of the scope for this thesis, but the details is given in[12].

2.3.1 The Range Doppler Algorithm

The Range Doppler Algorithm (RDA) is the oldest processing algorithm, developed in 1976-1978 for processing of SEASAT SAR data [12][13][14]. A version of the RDA algorithm suitable for *the high squint case*, meaning for wide beam satellites, is used for processing Sentinel-1 SLC data [15]. There are three main steps in RDA: range compression, range cell migration correction (RCMC) and azimuth compression as illustrated in figure 2.3.

Regarding the low squint case, one can assume the range equation $R(\tau)$ to have a parabolic form, which means that a linear FM signal in the time domain is transformed to a linear FM signal in the azimuth frequency domain. When the squint angle is increased, it is more accurate to express *the range equation* on

a hyperbolic form:

$$R^2(\tau) = R_0^2 + V_r^2 \tau^2. \quad (2.9)$$

Here R_0 is the slant range at which the radar is closest to the target and τ is the azimuth time. V_r denotes *the effective radar velocity*, which takes into account the curved earth geometry, and can be approximated by $V_r \approx \sqrt{V_s V_g}$. Here V_s is the satellite velocity and V_g is the ground velocity. The most accurate processing algorithms update this parameter at regular intervals in range, as these parameters vary with orbit position and range. The high squint case leads to a strong coupling between azimuth and range, which can be resolved using a filtering process called secondary range compression (SRC)[12].

2.3.1.1 Range compression and SRC filtering

The range compression is done by multiplying a *matched filter* to the received signal of equation 2.8 in the frequency domain. The matched filter is generated by taking the complex conjugate of the FFT of the zero padded pulse replica of equation 2.8.

The range compressed signal output can be denoted as:

$$s_{RC} = IFFT\{S_{rd}H_{rg}(f_r)\}. \quad (2.10)$$

Here S_{rd} is the range Fourier transform of equation 2.8, and IFFT represents the inverse fast Fourier transform. $H_{rg}(f_{\tau_r})$ is the matched filter in the range frequency domain. After range compression, the SRC filter is applied to s_{RC} by the filter function:

$$H_{src}(f_r) = \exp \left\{ -j\pi \frac{f_r^2}{K_{src}(R_0, f_a)} \right\}, \quad (2.11)$$

where K_{src} is the FM rate of the SRC filter.

2.3.1.2 Range Cell Migration Correction

Equation 2.9 indicates that the instantaneous slant range $R(\tau)$ changes with azimuth time τ . RCMC is a correction of the range delay of a point target as the target passes through the antenna beam. This is known as range migration.

The hyperbolic range equation in (2.9) can thus be written as:

$$R_{rd}(f_a) = \frac{R_0}{D(f_a, V_r)}, \quad (2.12)$$

where $D(f_a, V_r)$ is the migration factor, which is the cosine of the instantaneous squint angle corresponding to the azimuth frequency f_a . The RCMC is then equal to [15]:

$$RCMC(f_a, R_0) = R(f_a) - R_0 \quad (2.13)$$

2.3.1.3 Azimuth compression

Azimuth compression is done in a similar way as range compression. The only difference is that this is applied to each azimuth line and the matched filter is more complex, given by:

$$H_{az} = \exp \left\{ j \frac{4\pi R_0 D(f_a, V_r) f_0}{c} \right\} \quad (2.14)$$

By applying this filter the phase of each target is cancelled, except for a linear phase component, which gives each target its unique position in the output array [12].

2.3.2 The ωk Algorithm

The ωk Algorithm (ωkA) is the algorithm scheme outlined in the middle of figure 2.3. This algorithm consists of only four main operations, where all are done in the two-dimensional frequency domain. The original derivation of the algorithm was done in the *wavenumber domain*, which is a two-dimensional frequency domain represented by the *range angular frequency* $\omega = 2\pi f_0$ and the *azimuth wavenumber* k_i , where i represents either azimuth or range direction and has units of radians per meter instead of radians per second. The multiplication with a reference function focuses targets at a chosen reference range. The reference range is usually the mid-swath range, and only the target at this position is correctly focused. This stage compensates for the RCM and the range-azimuth coupling mentioned in 2.3.1. The *Stolt Interpolation* operation focuses the remainder of the targets. One important factor in the ωkA is that for both operations the effective radar velocity V_r is assumed to be constant in range [12].

2.3.3 The Chirp-scaling Algorithm

The Chirp-scaling Algorithm (CSA) is shown as the rightmost algorithm scheme in figure 2.3. The scheme consists of three phase operations, whereas the subsequent operations are similar to those in RDA. Both the first and second phase function operations correct for the range cell migration in contrast to RDA where one used an interpolator for RCMC. The main idea behind this processing algorithm is that if a linear FM signal is shifted in frequency, it will be shifted in time after pulse compression. By introducing this shift before the compression, one can correct for the range cell migration in a more efficient way. The first phase operation is referred to as the *differential RCMC*. Here a *chirp scaling function* is applied to correct the *difference* in RCM between signals at different ranges, resulting in that all signals have the same RCM. In the second phase operation referred, to as *bulk RCMC*, the remaining RCMC is done.

The chirp scaling function can be expressed as a linear or nonlinear function depending on whether one assumes the effective radar velocity and the FM rate to be constant or varying in range.

2.4 Speckle

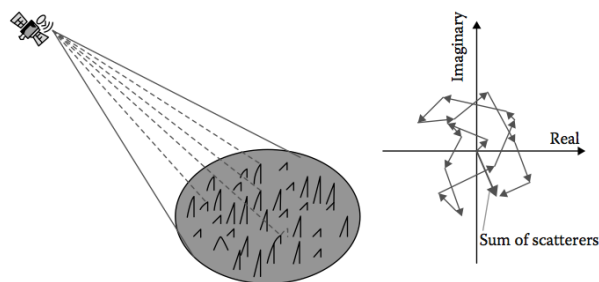


Figure 2.4: Speckle, Random walk in 2D [16].

Speckle is inherent in all coherent imaging systems and is shown as a strong brightness variation between neighboring pixels. When looking at a *homogeneous* surface area covering a resolution cell, there will be random scattering points due to the different microstructures at the surface. The returns from these scattering points will add vectorially as shown in figure 2.4, and result in a amplitude vector A and phase vector ϕ :

$$Ae^{j\phi} = \sum_{j=1}^{N_s} A_j e^{i\phi_j} \quad (2.15)$$

Here A_j is the amplitude, and ϕ_j the phase and from the j 'th scattering point in the resolution cell. The scattering points within a resolution cell are randomly distributed, and if there is sufficient numbers of them, *the central-limit theorem* applies. This means that one considers A_j and ϕ_j as independent random variables, and ϕ_j are uniformly distributed between $0 - 2\pi$. Thus the real and the imaginary parts of the complex amplitude obey a *Gaussian* probability density function (pdf), and it is well known that the single look amplitude and intensity fluctuations of speckle patterns follow a Rayleigh and negative exponential pdf.

The observed pixel intensity $I(x, y)$ will therefore consist of the true value from the target $\tilde{I}(x, y)$ and speckle η :

$$I(x, y) = \tilde{I}(x, y)\eta(x, y) \quad (2.16)$$

Speckle give rise to constructive and destructive interference between the various scatters, which results in so called salt-and-pepper noise which worsens the contrast in a SAR image.

2.5 Scattering

Scattering is a generic term for radiation dispersed in different directions as a EM wave interacts with different media. We have three main types of scattering mechanisms: surface scattering, double-bounce scattering and volume scattering.

2.5.1 Surface scattering

Surface scattering, known as *single bounce scattering*, occurs when the transmitted pulse has a single interaction with the medium. This happens in different degrees dependent on the surface roughness. For perfectly smooth surfaces, the radiation is reflected in a specular manner. For slightly rougher surfaces, the radiation is more dispersed but is scattered in a dominant direction. Regarding very rough surfaces the radiation gets more diffuse and is scattered in all directions. The roughness is mainly dependent on the surface height of deviation, the sensor wavelength and incidence angle. This means that the radar is depending on a relatively rough surface to receive a backscattered signal.

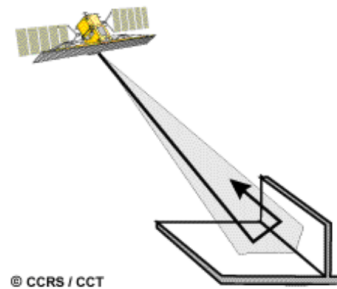


Figure 2.5: Dihedral scattering/corner reflection. Figure taken from [17]

2.5.2 Double bounce scattering

Double bounce scattering is shown in figure 2.5. The structure which causes it is referred to as a dihedral corner reflector if we have two perpendicular surfaces, or trihedral if we have three perpendicular surfaces. Ships and most man made structures are typically characterized by this type of scattering mechanisms.

2.5.3 Bragg scattering

From periodic surfaces such as ocean waves, the scattering can be described by the Bragg resonance given by:

$$\lambda_s = \frac{n\lambda_r}{2 \sin \theta_i}. \quad (2.17)$$

Here λ_s is the wavelength of the periodic surface, λ_r is the radar wavelength, and θ_i is the incidence angle.

2.5.4 Volume scattering

When the transmitted signal penetrates the surface we have a type of scattering called *volume scattering*. The penetration depth is inversely proportional to the radar frequency, but also depends on the dielectric constant. The amount of scattering that reaches out of the media and back to the radar is dependent on the volume geometry, density and moisture content.

2.6 Radar Cross Section

The radar equation describes the ratio of transmitted radiation P_t and received radiation R_r from a sensor [10]:

$$\frac{P_r}{P_t} = \left[\frac{P'_G}{P_G} G_g A_g \right] \frac{G A_e}{(4\pi r^2)^2} \quad (2.18)$$

This equation is derived by considering the ground as a receiving and reflective antenna. P_G is the receiving power from the ground and P'_G is the reflecting power from the ground. G and G_g are gain factors from the antenna and the ground respectively. The distance between the ground and the antenna is denoted r , where as A_e and A_g is the area of the antenna and the ground, respectively. The ground terms inside the brackets $[\cdot]$ constitute the *radar cross section* (RCS) σ , which tells us something about how "visible" a target/surface is to the radar. Often the normalized radar cross section $\sigma_0 = \sigma/A_g$ is used, and referred to as the *backscatter coefficient*.

2.7 Polarization

According to Maxwell's equations the electromagnetic wave is defined by an electric field and by a magnetic field that oscillate in a synchronized manner. These are perpendicular to each other and transverse to the direction of propagation in free space. The polarization refers to the *orientation* of the electric field. The orientation can be described by two orthogonal basis vectors \mathbf{H} and \mathbf{V} which represents, the linear horizontal and vertical polarizations [11].

The polarization of radar systems is used to better understand the complex scattering mechanisms of the surface of interest. The radar's transmit and receive polarizations depend on the available polarization modes of the SAR sensor. Onboard Sentinel-1 the polarization mode is either single or dual. A single polarization mode means that the radar transmits only one of the polarizations \mathbf{H} or \mathbf{V} , and also receive only one polarization. In dual polarization mode the radar transmits only one polarization, but receives both polarizations, which results in the combinations $(\mathbf{HH}, \mathbf{HV})$ or $(\mathbf{VV}, \mathbf{VH})$ where the first letter describes the transmitted signal, and the second letter describes the received polarization.

2.7.1 Scattering matrix

The characteristic of the RCS depend on the field polarity of the transmitter and the receiver, referring to the previous section 2.6. The relationship between the RCS and polarization is stated as follows:

$$\sigma_{pq} = 4\pi r^2 \frac{|E_{Sq}|^2}{|E_{Ip}|^2} \quad (2.19)$$

Here the P_G and P'_G is replaced with the incident electromagnetic field on a resolution cell E_{Ip} , where $p \in \{H, V\}$ specifies the polarization. E_{Sq} is the scattered electromagnetic field measured in polarizations $q \in \{H, V\}$. It can be shown that the scattering process measured by a full-polarimetric radar can be expressed in terms of a scattering matrix \mathbf{S} [16]:

$$\underline{\mathbf{E}}_S = \frac{e^{-jkr}}{r} \mathbf{S} \underline{\mathbf{E}}_I, \quad (2.20)$$

where $\underline{\mathbf{E}}_S$ is a vector holding the orthogonal components of the scattered wave, and $\underline{\mathbf{E}}_I$ represents the orthogonal component of the incident wave. The $\frac{e^{-jkr}}{r}$ represents the propagation effects, amplitude and phase. r is the range distance between the sensor and the target and k is the wavenumber of the electromagnetic field. \mathbf{S} is a 2×2 matrix which consists of four complex elements, \mathbf{S} is also known as the Sinclair matrix. The diagonal elements represents the co-polarized information while the off-diagonal elements represents the cross-polarized information.

$$[\mathbf{S}] = \begin{bmatrix} S_{HH} & S_{HV} \\ S_{VH} & S_{VV} \end{bmatrix} \quad (2.21)$$

The scattering matrix can be vectorized by *target vectors* \mathbf{k} in order to extract physical information. The representation is as follows:

$$\mathbf{k} = V(\mathbf{S}) = \frac{1}{2} \text{Trace}(\mathbf{S}\Phi) \quad (2.22)$$

Here Φ is a set of 2×2 basis matrices constructed as orthogonal set under the Hermitian inner product. Trace is the sum of the diagonal elements of Φ . There exists several basis sets, but two well known linear combinations are obtained from the Pauli and the Lexciographic matrices.

The Pauli spin matrix basis set Φ_P is defined as:

$$\Phi_P = \sqrt{2} \left\{ \begin{bmatrix} 1 & 0 \\ 0 & 1 \end{bmatrix} \begin{bmatrix} 1 & 0 \\ 0 & -1 \end{bmatrix} \begin{bmatrix} 0 & 1 \\ 1 & 0 \end{bmatrix} \begin{bmatrix} 0 & -j \\ j & 0 \end{bmatrix} \right\} \quad (2.23)$$

where the corresponding complex target vector \mathbf{k}_P is defined as:

$$\mathbf{k}_P = \frac{1}{\sqrt{2}} \begin{bmatrix} S_{HH} + S_{VV} \\ S_{HH} - S_{VV} \\ S_{HV} + S_{VH} \\ j(S_{HV} - S_{VH}) \end{bmatrix} \quad (2.24)$$

The Lexicographic matrix basis set Φ_L is defined as:

$$\Phi_P = 2 \left\{ \begin{bmatrix} 1 & 0 \\ 0 & 0 \end{bmatrix} \begin{bmatrix} 0 & 1 \\ 0 & 0 \end{bmatrix} \begin{bmatrix} 0 & 0 \\ 1 & 0 \end{bmatrix} \begin{bmatrix} 0 & 0 \\ 0 & 1 \end{bmatrix} \right\} \quad (2.25)$$

where the corresponding target vector \mathbf{k}_L is defined as:

$$\mathbf{k}_L = \frac{1}{\sqrt{2}} \begin{bmatrix} S_{HH} \\ S_{HV} \\ S_{VH} \\ S_{VV} \end{bmatrix} \quad (2.26)$$

\mathbf{k}_P has an advantage over \mathbf{k}_L since it is closely related to the physical properties of the scattering medium.

/ 3

Terrain Observation by Progressive Scans

SLC images acquired in TOPS mode have special spectral characteristics. In order to correct these, knowledge about the acquisition is necessary. This thesis interpret and deals with TOPS SLC images produced from two different focusing schemes with adjustable parameters. An understanding of the various processing schemes is needed in order to compare these outputs, and especially make processing adjustments advantageous for ship detection.

This chapter describes the principles behind TOPS acquisition and focusing and highlights areas of data processing that have to be taken into account when dealing with SAR data acquired in TOPS mode. In order to understand the special features, the chapter begins with a brief introduction to ScanSAR [18] and describe its differences compared to TOPS mode. The chapter ends by introducing Kongsberg Spacetec NRTSAR and the adjustable parameters.

A SAR is operated in different imaging modes to accommodate different needs for spatial resolution and coverage. Considering the imaging mode briefly discussed in section 2.1, data are acquired by transmitting a periodic sequence of pulses, which are processed into a continuous image. This is referred to as the *Stripmap* mode. At the expense of resolution in azimuth it is possible to form a continuous image without using all the transmitted pulses. The transmitter is then turned on and off cyclically and will illuminate portions of the scene

with bursts of N_p pulses. This is useful in cases where one have restrictions regarding power and downlink capacity, but can also be utilized to illuminate other range swaths and obtain wide-swath coverage [12].

When it comes to wide-swath coverage, which is of interest in ship detection, the conventional mode up till now has been ScanSAR. Sentinel-1 represents a change in this respect, the instrument provides two different SAR imaging modes which provides wide area coverage:

- Interferometric Wide Swath Mode.
- Extra Wide Swath Mode.

Both Interferometric Wide Swath Mode and Extra Wide Swath mode uses the newly proposed TOPS technique which also provides a wide swath coverage [19].

3.1 ScanSAR

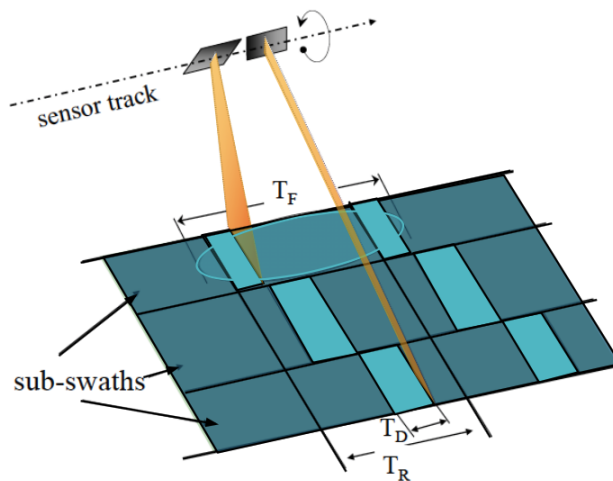


Figure 3.1: ScanSAR imaging geometry with three sub-swaths. T_F : Footprint time, T_D : Dwell time, T_R : period of bursts, figure adjusted from [19]

In ScanSAR the azimuth antenna beam point is held fixed and the elevation beam is periodically switched to obtain large illumination area consisting of several sub-swaths [18]. In ScanSAR image processing, each sub-swath is

processed separately, and after the imaging all the sub-swaths are combined to form the resulting image. Figure 3.1 illustrates the imaging geometry of a ScanSAR with three sub-swaths. Typically, each sub swath covers 100 km to 150 km, but it can be widened by allowing a lower azimuth resolution or by taking fewer looks. The number of looks is determined by the burst duration time T_B . It is possible to extract two or more looks from each burst if T_B is such that two or more burst cycles of a given beam can be completed within the footprint time T_F . The sensor acquires a finite sequence of bursts for a dwell time T_D , repeated with a period T_R . T_F/T_R gives the number of looks imaged [12].

3.1.1 ScanSAR acquisition

In ScanSAR only a certain number of bursts is collected at a time. Figure 3.2 shows the time/frequency relation of the raw data acquisition in azimuth for ScanSAR. In signal processing these type of diagrams are referred to as *spectrograms*. Spectrograms are three dimensional representation of a signal with respect to time, frequency and spectral energy. The rectangular boxes represent the received frequency by two consecutive bursts acquired within the T_F . The horizontal side of the boxes shows the burst duration T_B and the vertical side represents the total Doppler bandwidth for one burst. In the literature these boxes are referred to as the time frequency domain (TFD) support for the raw data. Here τ is the time in azimuth, where the origin is assumed to be at the center of the first burst. $P_1 - P_4$ are four targets at their zero-Doppler time. The lines represent the Doppler history of each target, where the negative slope is given by the Doppler rate k_R . Since the azimuth antenna beam point is held fixed during T_D , the azimuth antenna pattern (AAP) is also fixed during this time. The shading within each rectangular box represents the third dimension of the diagram, this is the amplitude weighting of the AAP. The light tone represents high antenna weight and the dark tone represents low weighting. Concerning the first burst, the Doppler histories from point target P_1 , P_2 and P_3 are shown and it is clear that each target is weighted differently by the AAP. B_a represents the bandwidth for each target.

3.1.2 Scalloping

As stated above, the amplitude weighting of the AAP varies from target to target dependent on where it is located in the azimuth direction. This implies that image quality parameters also will vary in the azimuth direction [20]. *Scalloping* is an unwanted radiometric variation shown in the resulting SAR image as a sequence of bright and dark stripes oriented in the range direction.

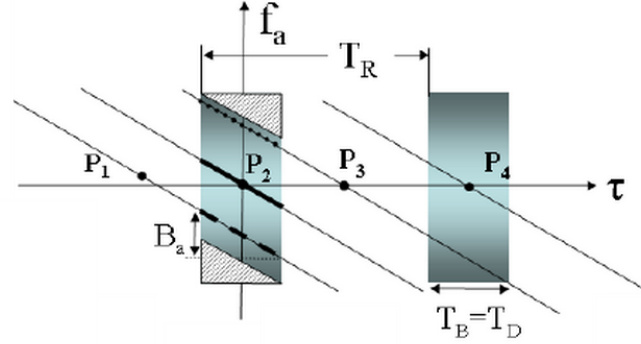


Figure 3.2: Spectrograms of azimuth time/frequency support for raw data in ScanSAR,
 f_a : Frequency in azimuth.
 τ : Time in azimuth.
 T_R : Period between each burst.
 $P_1 - P_4$: Targets at different azimuth locations.
 B_a : Doppler bandwidth of a single target. Figure is obtained from [19].

This effect is mainly due to the fact that each target is seen by different parts of the AAP. This variability follows in the azimuth signal processing of the raw data and can only be corrected if one has knowledge about the SNR, the beam shape or an accurate Doppler centroid estimation. The effect is reduced by multilook processing [12]. The azimuth ambiguity ratio and the noise equivalent σ_{NE}^0 will also vary as a consequence of the varying azimuth antenna pattern for each target.

3.1.3 ScanSAR resolution

Compared to the resolution in Stripmap mode each subswath has to share the synthetic aperture length, and thus there is a tradeoff between azimuth resolution and swath width [18]. Referring to the same parameters in equation (2.5) the resolution in azimuth is for a *one-look* system is given by

$$\Delta \tilde{x}_{a(ScanSAR)} \approx N_s \frac{A_A}{2}, \quad (3.1)$$

where N_s is the number of subswaths.

3.2 TOPS

TOPS mode was proposed to solve the problems with azimuth varying ambiguities in ScanSAR [19]. Figure 3.3 shows the image geometry of TOPS. Here the antenna is rotated in both azimuth and range direction. As the beam is elevated in the range direction it is simultaneously swept from back to forward in the azimuth direction during the acquisition of long bursts. Compared to Spot mode, as shown in figure 3.4, the antenna is rotated in the opposite direction and this causes a worsening of azimuth resolution [21]. Compared to the standard Stripmap mode the sensor acquires backscatter from a longer area given the same time span. This makes it possible to switch the antenna to different subswaths in range similar to ScanSAR. The difference is that TOPS exploits the sweeping, and manages to return to the ending of the first subswath scan, producing a *one look system*. The direction of the beam center in TOPS mode is given by [19]:

$$\phi_{dc} = k_{\phi}\tau, \quad \text{with } k_{\phi} < 0. \quad (3.2)$$

Here k_{ϕ} denotes the antenna rotation at a negative rate [rad/s] and τ is the azimuth time.

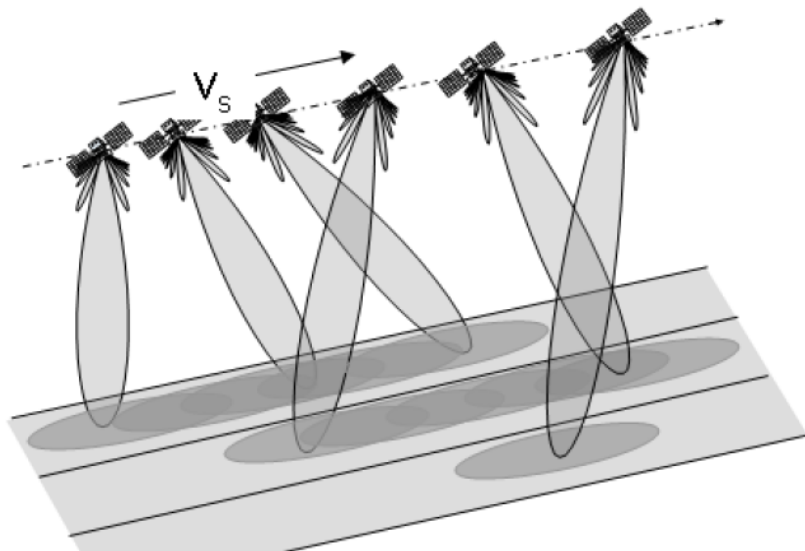


Figure 3.3: TOPS imaging geometry, V_S : velocity of satellite [19].

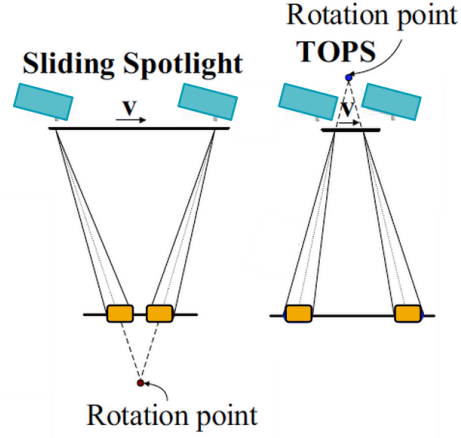


Figure 3.4: Reduction of azimuth resolution compared to SPOT imaging mode, figure obtained from [21]

3.2.1 TOPS acquisition

Figure 3.5 shows the time-frequency relation of the raw data acquisition in TOPS. As in Figure 3.2 regarding ScanSAR, four point targets $P_1 - P_4$ are represented at their zero Doppler time, where the oblique lines represent the Doppler history of each target. The negative slope is given by the Doppler rate k_R , which is the rate of change of the Doppler frequency:

$$k_R = \frac{2V_s^2}{\lambda R} \quad (3.3)$$

Here it is assumed a simplified rectilinear geometry, meaning that the curved earth geometry is neglected, hence the velocity is denoted as the satellite velocity V_s . In contrast to ScanSAR the antenna rotation introduces a Doppler centroid rate which is responsible for the shape of the TFD support. When the radar is moving in opposite direction to where the antenna is pointing, this induces negative frequency. When the antenna is pointing in the same direction as the radar, the frequency is positive. The Doppler centroid rate is given by:

$$k_a = \frac{\partial(-\frac{2v_s}{\lambda} \sin(\phi_{dc}(\tau)))}{\partial \tau} \simeq -\frac{2v_s}{\lambda} k_\phi \quad (3.4)$$

The narrow vertical boxes which show the weighting of the AAP indicate that during one burst interval the antenna is swept such that each target is "seen" by the the complete AAP (except those at the edges of the burst). Figure 8.1 in Appendix A shows a more intuitive illustration of the relation between figure 3.3 and 3.5. The equal weighting of the AAP on each target results in a *nonvarying* resolution in azimuth and no scalloping.

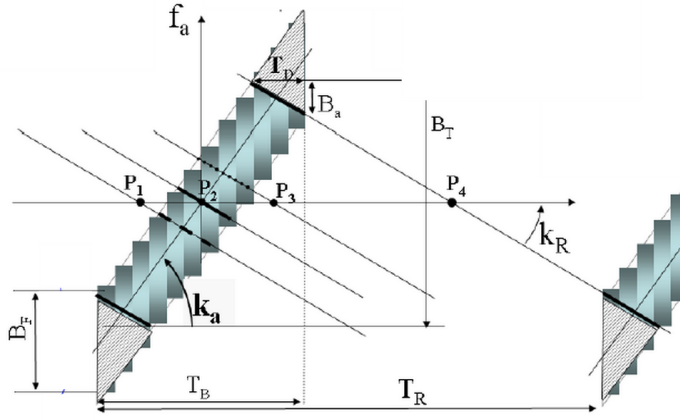


Figure 3.5: Azimuth time and doppler frequency relation in TOPS mode.

- f_a Frequency in azimuth
 - τ : Time in azimuth $P_1 - P_4$ Targets,
 - B_a : Bandwidth of a target
 - B_F : Footprint bandwidth,
 - B_T :Total Doppler bandwidth,
 - k_a : Doppler centroid rate,
 - k_R : Doppler FM rate,
 - T_B : Burst duration,
 - T_D : Dwell time,
 - T_R : Period between two bursts.
- Figure obtained from [19]

3.2.2 TOPS resolution

The rotating antenna is illuminating a target with a footprint on the ground that is shrunken by a factor α with respect to standard Stripmap mode:

$$\alpha = 1 + \frac{R_0 |k_\phi|}{v_s} \gg 1. \quad (3.5)$$

In equation 3.5, R_0 is the shortest distance between the sensor and a target, v_s is the sensor velocity and k_ϕ is the antenna rotation rate. This means that with respect to Stripmap SAR the resolution is α times coarser, and the synthetic aperture length in TOPS mode can be denoted as $L_T = \alpha L$ where L is the antenna length in Stripmap SAR. This gives the resolution in azimuth:

$$\Delta \tilde{x}_{a(TOPS)} \approx \alpha \frac{A_A}{2}. \quad (3.6)$$

3.2.3 TOPS focusing

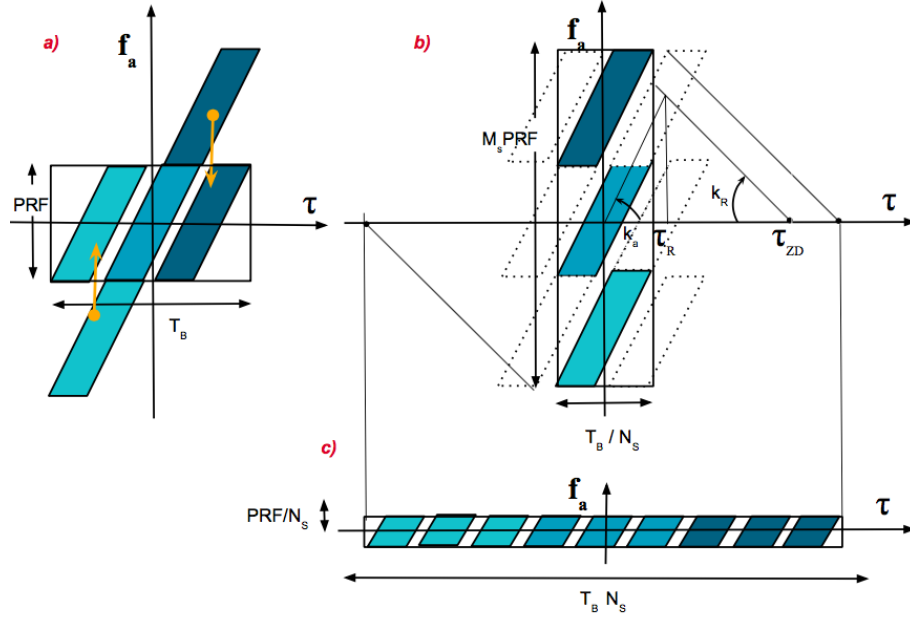


Figure 3.6: TFD support for TOPSAR data, a) range compressed data, unfolded and folded; b) data after spectral expansion by mosaicking shown by the dotted lines and folding in time domain; c) focused data folded in frequency domain. Figure obtained from [19].

A TOPS focusing algorithm has some issues to handle. First of all, even though the Doppler bandwidth for each target is less than the PRF, the total bandwidth may span several PRFs and thus cause aliasing and *folding* in the frequency domain. If one assumes that the total bandwidth $B_T \simeq k_a T_B$, the folding will occur M_s times in the f_a :

$$M_s \simeq \frac{B_T}{PRF} = \frac{k_a T_B}{PRF}. \quad (3.7)$$

This folding will increase with the length of the burst [19].

Several focusing techniques are proposed in the literature. The diversity comprises the focusing algorithms introduced in section 2.3 with various improvements. This section will continue with presenting the algorithms discussed in [19], followed by the focusing scheme used in Sentinel-1 for Level-1 SLC processing. Finally, other relevant focusing schemes are introduced.

De Zan & Monti Guarnieri [19] claims that in theory a phase preserving Stripmap processor can be used to focus the TOPS raw data. Here one assumes that the data are already compressed in range. The procedure can be divided into three steps: *Unfolding*, *focusing* and *subsampling*. First, the data are unfolded in frequency domain by upsampling M_s times. This is done by zero-padding in the time domain to extend the duration of the burst: $T_R = N_s T_B$. The TFD support will then span a range $[N_s T_B, M_s PRF]$. Here, a Stripmap processor comes into play. The final step by subsampling the data $M_s N_s$ times leaves the TFD support as in figure 3.6 c). This is highly inefficient with respect to processing time and data space.

The more effective focusing scheme proposed in [19] is shown in figure 3.6. This procedure is based on a mix of ScanSAR and SPOT focusing, divided into a pre- and postprocessing step and with the use of a $\omega - k$ processor, referring to subsection 2.3.2. The preprocessing step corresponds to the preprocessor for SPOT mode described in [22]. Here the range compressed bursts are unfolded in the frequency domain by expanding the sampling rate to fit the total bandwidth. This is done by oversampling the data M_s times in the frequency domain, leaving the sampling frequency equal to $M_s PRF$ as in figure 3.6 b). This is done by the following steps:

- *Mosaicking*: This is shown as the dotted lines in figure 3.6 b), where we have M_s times replication.
- *Deramping*: The spectrum is multiplied by the following chirp signal applied in the frequency domain:

$$\phi(f_a) = \exp \left\{ j\pi \frac{1}{k_a} (f_a - f_{ac})^2 \right\} \quad (3.8)$$

where the f_{ac} is the Doppler centroid frequency.

- Low-pass filtering and downsampling is done to remove the unwanted spectral contributions.
- Reramping the data with a reference conjugate of equation 3.8:

$$\phi(f_a) = \exp \left\{ -j\pi \frac{1}{k_a} (f_a - f_{ac})^2 \right\} \quad (3.9)$$

This leaves the TFD support as shown in figure 3.6b). Next the data are focused by the $\omega - k$ processor before the postprocessing step. In the post-processing step the data are unfolded and resampled again, with the same procedure as

described above, but now in the time domain. This means that the deramping equation 3.8 is changed to:

$$\phi(\tau) = \exp \{-j\pi k_t (\tau - \tau_{ref})^2\}, \quad (3.10)$$

where

$$k_t = \frac{k_a k_R}{k_a + k_R}. \quad (3.11)$$

Here k_t accounts for the stretch of the time axis between the raw data and the focused data. Applying the time deramping and reramping results in the focused data shown in figure 3.6 c).

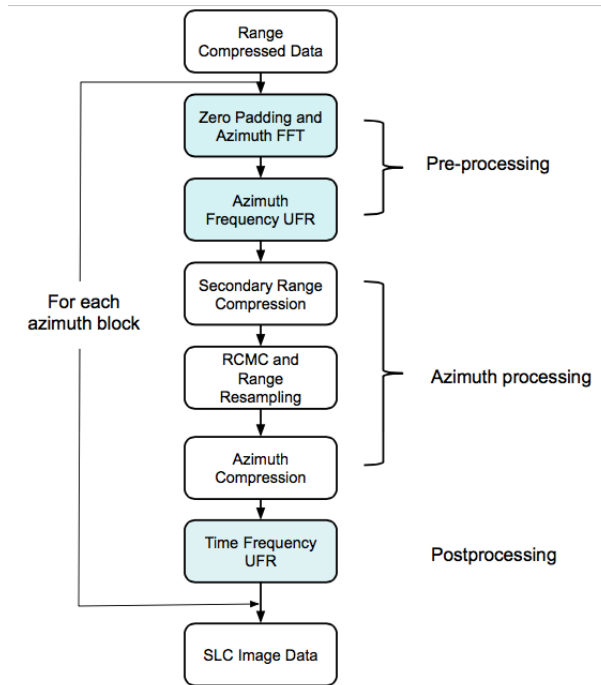


Figure 3.7: Sentinel-1 SLC Processing Algorithm [19]

The Sentinel-1 Level-1 SLC Processing Algorithm, IPF, is shown in figure 3.7 and explained in detail in [15]. For simplicity only the azimuth processing is considered. The processing is done individually for each burst in each sub-swath and the resulting SLC image is then included in azimuth time order, into a single sub-swath image.

The azimuth preprocessing step consists of zero-padding, FFT, unfolding and resampling (UFR) in the frequency domain. The unfolding and resampling is done in the same way as explained above. This is applied to each azimuth line in a burst where the input azimuth line has the same TFD support as shown

in figure 3.6 a). Next the azimuth processing is done by *the Range-Doppler Algorithm (RDA)* as described in section 2.3.1. For efficiency reasons the RCMC is accompanied with resampling in range. Lastly comes the postprocessing step, which is the unfolding and resampling in the *time domain* as described previously for the frequency domain.

Prats et al.[23] points out the computational burden by using a pre- and post-processing step and that a dedicated processor must be developed if efficient focusing is desired. They proposed a version of the *The Extended Chirp Scaling (ECS)* algorithm as an alternative for the azimuth processing of TOPS data. Compared to the chirp scaling algorithm in section 2.3.3 the first five steps are similar, but the azimuth compression stage is replaced by a frequency scaling operation that equalizes the azimuth FM rate at each range cell [12]. The unfolding is avoided by dividing the data in azimuth blocks, called sub-apertures with an overlap of 5%. The processing is done individually on each block by ECS functions, before the supapertures are assembled and the final azimuth compression is performed.

Engen and Larsen [24] have proposed an effective preprocessing algorithm that focuses the entire azimuth aperture without oversampling, zero-padding or subaperture processing. They comment on the focusing scheme shown in figure 3.6 which is inefficient with respect to processing time and the number of data points that must be used in the zero padding. They suggest that a possible improvement is to transform the frequency folded data in figure 3.6 a) directly to the time folded representation, without the unfolding step. They propose a Moving Band Chirp Z-transform (MBCZT) as a solution. They claim that the MBCZT can be used in both the transformation between frequency folded data in 3.6 a) to b), and from the focused time folded data to the focused frequency folded data in 3.6 c), where the latter one uses an inverse MBCZT. In the paper they have used a ωkA for the focusing step, but mention that any Stripmap processor can be used.

Adriano et al. [25] report results from an image scalloping analysis done for both ScanSAR and TOPS mode obtained with TerraSAR-X. The results show that the scalloping of the TOPS image was 0.3 dB against 1.2 dB in the ScanSAR image.

3.3 Kongsberg Spacotec Near Real Time processor

Kongsberg Spacotec have proposed a SAR processor based on the algorithm from Engen and Larsen [24] briefly described in section 3.2.3. This is an effective algorithm compared to the ESA IPF. Kongsberg Spacotec claim that their processor is *four times faster* than the ESA IPF. Near Real Time (NRT) processing is obtained using pipelined parallel processing.

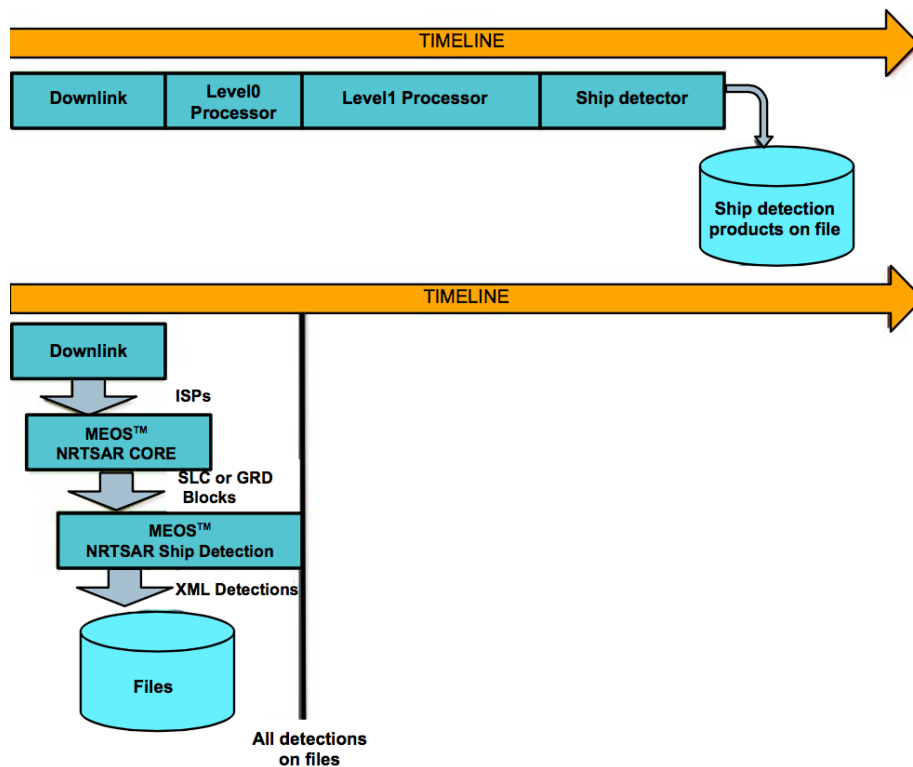


Figure 3.8: NRTSAR and ship detection flow chart. *Kongsberg Spacotec, All Rights Reserved*

Figure 3.8 shows how the processing time is shortened with the NRTSAR. The upper time flow chart shows the traditional sequential processing used by ESA IPF. Here the *Level0* represents the processing of the ISP stream to raw data and *Level1* represents the processing from raw data into SLC or GRD products. After these steps and when the image is fully processed, a ship detector is used. In the lower flow chart the *NRTSAR CORE* processes blocks of Instrument Source Packet (ISP) streams as they are downlinked. These blocks are further processed by *NRTSAR* into SLC data. This means that a ship detector can be

introduced in an earlier stage of the processing chain, and thus can be applied to blocks of data before the total image is fully processed.

In this thesis a prototype of the NRTSAR is used where one can adjust the following parameters: output spacing, processing bandwidth and window functions. The following sections will roughly explain the output from the processor.

3.3.1 Impulse Response

In signal processing *the impulse response* represents the behavior of a system by describing its response to receiving a theoretical delta function as input. In terms of satellites, the impulse response describes the imaging performance of a radar. Referring to the SAR processing in section 2.2, the impulse response is the output after focusing a single point target. A trihedral corner reflector is the most commonly used object for generating an impulse response in a test image. The impulse response is also known as the point spread function and is shown in figure 3.9.

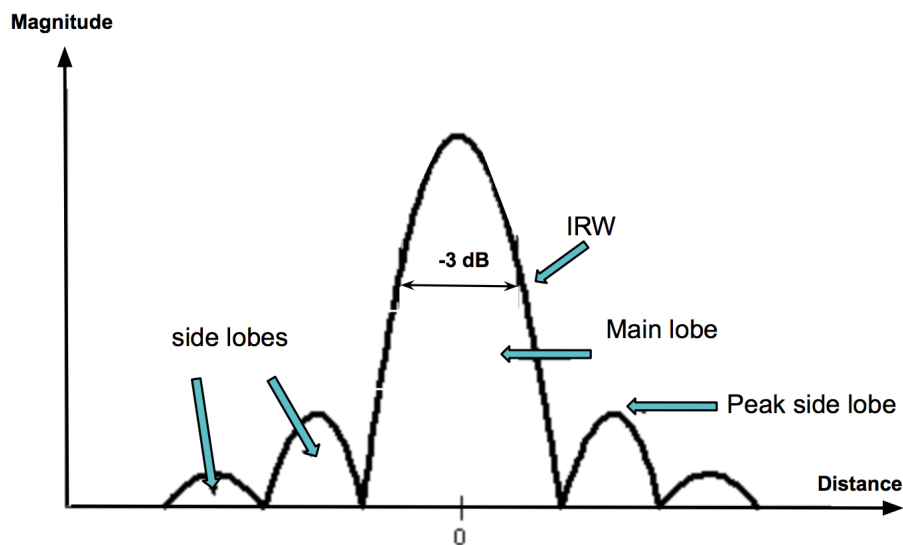


Figure 3.9: Impulse response from a single point target. Figure taken from [26]

Figure 3.9 shows that the impulse response can be approximated as a sinc-like function. Here the *main lobe* represents the central peak where the high energy is located and the *sidelobes* represents the smaller peaks located on either side of the main lobe.

The quality of the impulse response is determined by how well the pixel is represented by the energy that originates from the location of the point target, respectively. A good impulse response have less energy representing the surrounding pixels. The impulse response width (IRW) is defined as the width of the main lobe measured -3 dB below the peak value. The resolution is associated with the IRW. The narrower the IRW, the higher the resolution. The peak to sidelobe ratio (PSLR) is defined as the ratio of the peak in largest side lobe to the peak in the main lobe measured in decibels. The integrated sidelobe ratio (ISLR) is defined as the integrated energy of all the sidelobes to the energy in the main lobe. This means that both the ISLR and the PSLR should be *small* in order to obtain high local contrast in the image. In practice this means that it is desired to avoid that dark areas in the image do not get obscured by energy from nearby strong scatters. Usually the PSLR and ISLR ratio is too large, since it masks out nearby weaker targets in the image. One way of reducing this is to use a smoothing window.

3.3.2 Window functions

In terms of raw data processing and pulse compression referring to section 2.3, a window function or window apodization is applied to the signal spectra. The window function is symmetric and adds weight to the signal spectra. The center of the aperture is weighted higher than the ends. The window functions has a smoothing effect and reduces the leakage of energy from the main lobe to the side lobes of the signal spectrum. More specifically the window broadens the main lobe (the nearest side lobe is absorbed), but lowers the side lobes.

When applying a window, the resolution degrades as a consequence of reduction in the effective signal bandwidth and because of the broadened main lobe [12]. Several window functions have been developed with different weighting coefficients [27] where the Kaiser, Taylor and Hamming windows are commonly used in SAR processing schemes [28] [29]. When choosing an appropriate window, one has to evaluate the tradeoff between side lobes and resolution. This means that the overall goal is to gather the highest energy in the main lobe for a given ISLR.

A Hamming window with different coefficients depending on sub swaths is used in IPF focusing of Sentinel-1 SLC data. The different coefficients with respect to subswath are represented in table 3.1.

In a point target analysis done on the ESA IPF, different ISLR, PSLR, and IRW broadening factors were measured for different Hamming windows, referring to table 3.2. Here we see that the lower window coefficients, the lower ISLR and PSLR, and equivalently broader IRW. Section 4.6.2 evaluates how the

Hamming Window Coefficients for TOPS IW mode		
Swath	Azimuth	Range
IW1	0.70	0.75
IW2	0.75	0.75
IW3	0.75	0.75

Table 3.1: Hamming window coefficient for each subswath in TOPS IW mode used by ESA IPF. Table taken from [15].

adjustment of window functions may have an impact in ship detection.

Hamming Window Coefficient	IRW Broadening Factor	PSLR [dB]	ISLR[dB]
0.52	1.54	-36.22	-37.39
0.6	1.32	-31.6	-26.18
0.61	1.3	-30.34	-25.22
0.62	1.28	-29.29	-24.35
0.63	1.27	-28.33	-23.55
0.65	1.24	-26.79	-22.07
0.70	1.18	-24.07	-19.10
0.72	1.16	-23.27	-18.10
0.73	1.15	-22.55	-17.63
0.75	1.13	-21.22	-16.75

Table 3.2: Hamming window coefficients, IRW, PSLR and ISLR measured from point target analysis from ESA IPF. Table taken from [15]

3.3.3 Bandwidth

Figure 3.6 c) shows that the total available processing bandwidth $B_{a(IPF)}$ for each target is PRF/N_s after the unfolding and folding procedure in ESA IPF. In the NRTSAR processor $B_{a(NRTSAR)}$ is limited to $\frac{1}{4}PRF$ for a TOPS system with three subswaths [30]. This means that $B_{a(IPF)} > B_{a(NRTSAR)}$. The PRF is different for each subswath and therefore different bandwidths are used to process data from each subswath. The SLC images processed by ESA IPF, has B_a for each sub-swath shown in table 3.3. In the prototype of NRTSAR used in the experimental part, this bandwidth is adjustable.

The total bandwidth B_T is also adjustable. To date the ESA IPF process data with a fixed B_T . This ensures that all targets experience the complete AAP and minimal overlap is achieved. In order to adjust the overlap areas between

Processing bandwidth by ESA IPF for TOPS IW mode		
Swath	Azimuth [Hz]	Range [Hz]
IW1	327	5.65 e7
IW2	313	4.83 e7
IW3	314	4.27 e7

Table 3.3: Processing bandwidth corresponding to each subswath used on TOPS IW data by ESA IPF, table taken from [31].

bursts, one needs to access the frequencies located in gray shaded areas shown in the TFD support, referring to figure 3.5. In these areas, the target does not experience the full AAP and they have less dwell time. However, by expanding the Doppler bandwidth B_T to cover the overlap areas, one will access new areas in the beginning and at the end of each sub-swath and increase the overlap area between bursts. These areas will contain less intensity but may be utilized to detect targets. Considering near real time processing, this means that a larger burst area is accessible at an earlier stage. By allowing a higher B_T in the NRTSAR processing, the processor will run slower, because of the handling of larger blocks of data. Thus a tradeoff between overlap area and processing time must be made. The overlap area is briefly explored in the context of ship detection in the experimental part 6.3.

3.4 TOPS Deramping

The Sentinel-1 SLC products from TOPS mode have some special spectral characteristics in azimuth. If a spectrogram is produced from the SLC image, it will still show a linear frequency rate, and the azimuth spectra are distorted due to the linear frequency modulation. In order to perform any spectral operations or perform basic operations like resampling, a *deramping procedure* is necessary for each burst. Figure 3.10 show the distortion in the azimuth spectrum (left) and how this is corrected by the deramping procedure (right). The deramping is done by multiplying each azimuth line with the chirp defined in equation 3.12:

$$\phi(\tau) = \exp \left\{ -j\pi k_t (\tau - \tau_{ref})^2 \right\}. \quad (3.12)$$

Here τ is the azimuth time corresponding to zero Doppler azimuth time in the middle of the burst. k_t is the Doppler centroid rate in the focused SLC image:

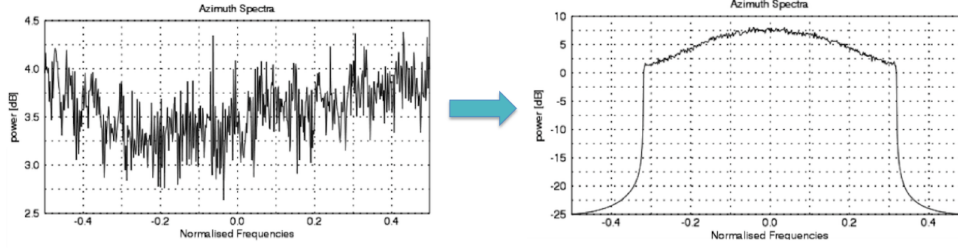


Figure 3.10: Azimuth frequency spectrum before and after the deramping procedure [32].

$$k_t = \frac{k_a k_r}{k_r - k_a}, \quad (3.13)$$

where k_a is the Doppler centroid rate in raw data, and k_r is the Doppler rate. These are range varying parameters, and in order to get the most accurate result k_t is must be estimated for every range sample in the image [33]. The Doppler centroid rate in the raw data is given by:

$$k_a = \frac{2v_s k_\phi}{\lambda}, \quad (3.14)$$

where k_ϕ is the constant negative azimuth steering rate, λ is the wavelength and v_s is the satellite velocity. The range/azimuth reference time τ_{ref} . It is the time in the center of azimuth as a function of range time and is computed as followed:

$$\tau_{ref} = t_{ar} - t_{ar}(0), \quad (3.15)$$

where

$$t_{ar} = -\frac{f_{dc}}{k_r}. \quad (3.16)$$

3.4.1 Results deramping TOPS data with ESA IPF and NRTSAR

In relation to each experiment done in this thesis, every SLC data product is deramped as described in section 3.4. The deramping is needed to correct the frequency spectra in both azimuth and range. In the metadata there is a velocity estimate for each second of the burst duration. The velocity estimates were linearly interpolated, and an estimate for the azimuth time in the middle of each burst was used. The metadata also contains an estimate of k_r for each burst. This estimate consists of roots of the Doppler rate polynomial denoted as a vector $[c_1, c_2, c_3]$. These are multiplied by a range time varying vector t_r in order to get an estimate for each sample in range.

Polynomials for the Doppler Centroid frequency f_{dc} are also found in the metadata. The f_{dc} is found in two categories, estimates from raw data, and estimates from orbit geometry. The SLC data focused by ESA IPF uses f_{dc} estimates from data, while the SLC data focused by NRTSAR uses f_{dc} estimates from orbit. Thus, the f_{dc} estimated from raw data is used when SLC products from ESA IPF is deramped, and f_{dc} estimates from orbit is used when SLC data is focused by NRTSAR. Both are estimated in the same manner as for the Doppler rate k_r . Experience with SLC data focused by ESA IPF has shown that for SLC images obtained in sub swath 3, (iW3) there is no f_{dc} estimate for the last burst. In these cases the f_{dc} estimate is repeated for the last two bursts.

Figure 3.11 shows how the mean azimuth frequency spectrum is corrected by the deramping procedure. This is an example where the deramping is well performed. Here we see that the azimuth spectrum is bandlimited and that the f_{dc} is shifted to zero. The shape of the spectrum show that a Hamming window is used as a weighting function in the processing. Figure 3.12, on the other hand, has several artifacts. First of all we see that the Doppler centroid frequency f_{dc} is not shifted to zero frequency. Secondly the spectrum representing VH has some strange edge effects. These effects are mentioned in a workshop paper [34] where the processor is assumed to be the cause. In the subaperture ship detection algorithms, additional spectrum shifting is done in order to shift f_{dc} to zero.

Figure 3.13 shows the deramping performed on SLC data focused by NRTSAR. The processing is done with same bandwidth and weighting function as in the ESA IPF. As mentioned in section 4.6.1, the total available processing bandwidth differs between the two processors: $B_{a(IPF)} > B_{a(NRTSAR)}$. This is the reason why the azimuth spectra in figure 3.12 and 3.11 appear to cover less bandwidth. The antenna of Sentinel-1 is steered with aZero Doppler Attitude regulation.

This accounts for the Doppler shift caused by Earth's rotation. This means that it might be more accurate to assume zero f_{dc} than estimating it. In NRTSAR there is no correction for the f_{dc} , which is assumed to be zero. ESA IPF, on the other hand, uses Doppler centroid corrections, and this may be the offset experienced in some spectra.

In ESA IPF additional pattern corrections are applied to the spectra, which is not accounted for in the NRTSAR processor. This includes an elevation pattern correction and correction of the azimuth antenna pattern.

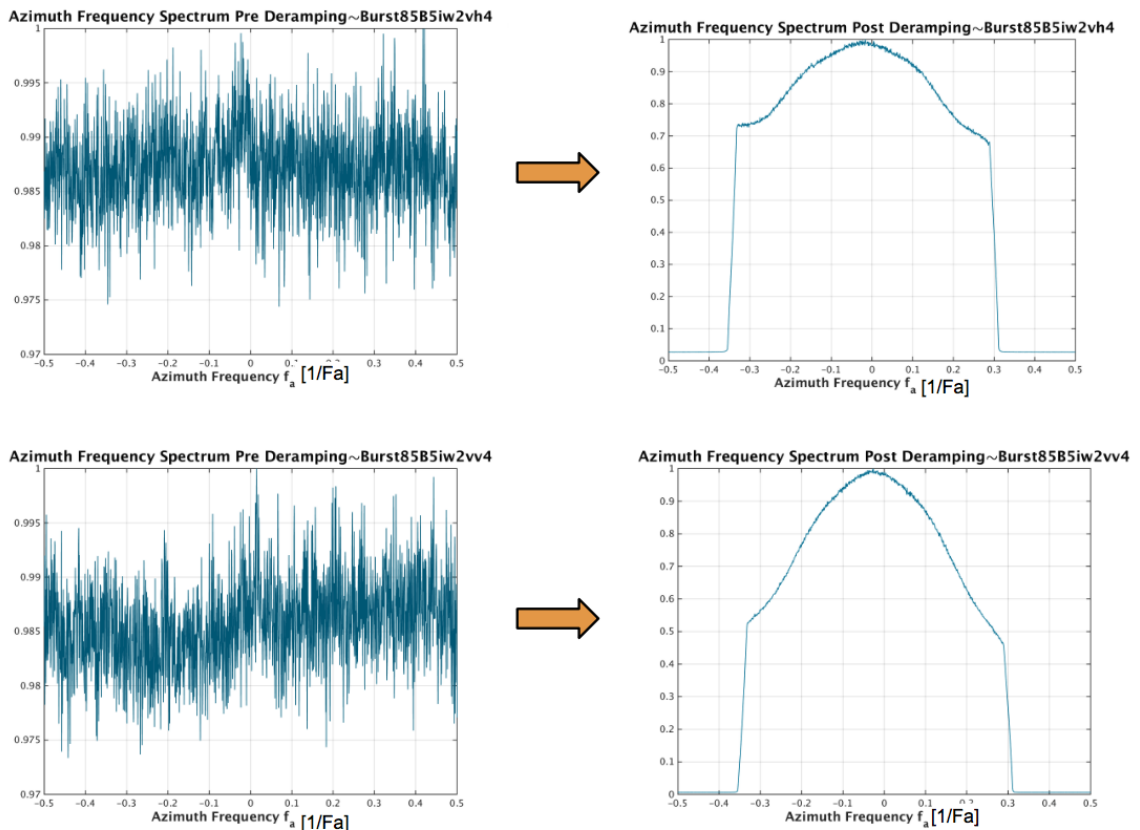


Figure 3.11: Deramping SLC product focused by ESA IPF (burst 3, IW1 from scene 85B5)
 Left: Original Spectra after processing with IPF
 Right: Spectra after deramping
 Upper row, VH polarization
 Lower row, VV polarization

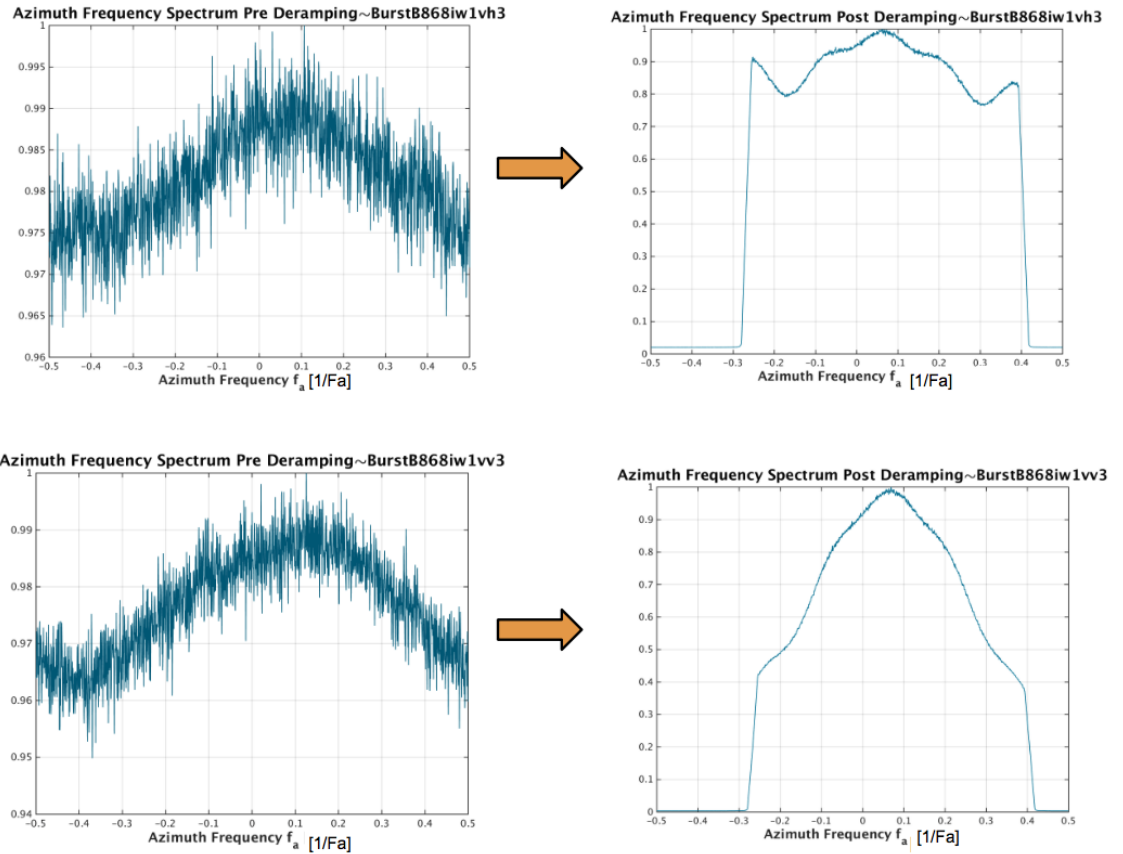


Figure 3.12: Deramping SLC product focused by ESA IPF, (burst 3, IW1 from scene B868) Left: Original Spectra after processing with IPF
 Right: Spectra after deramping
 Upper row, VH polarization
 Lower row, VV polarization

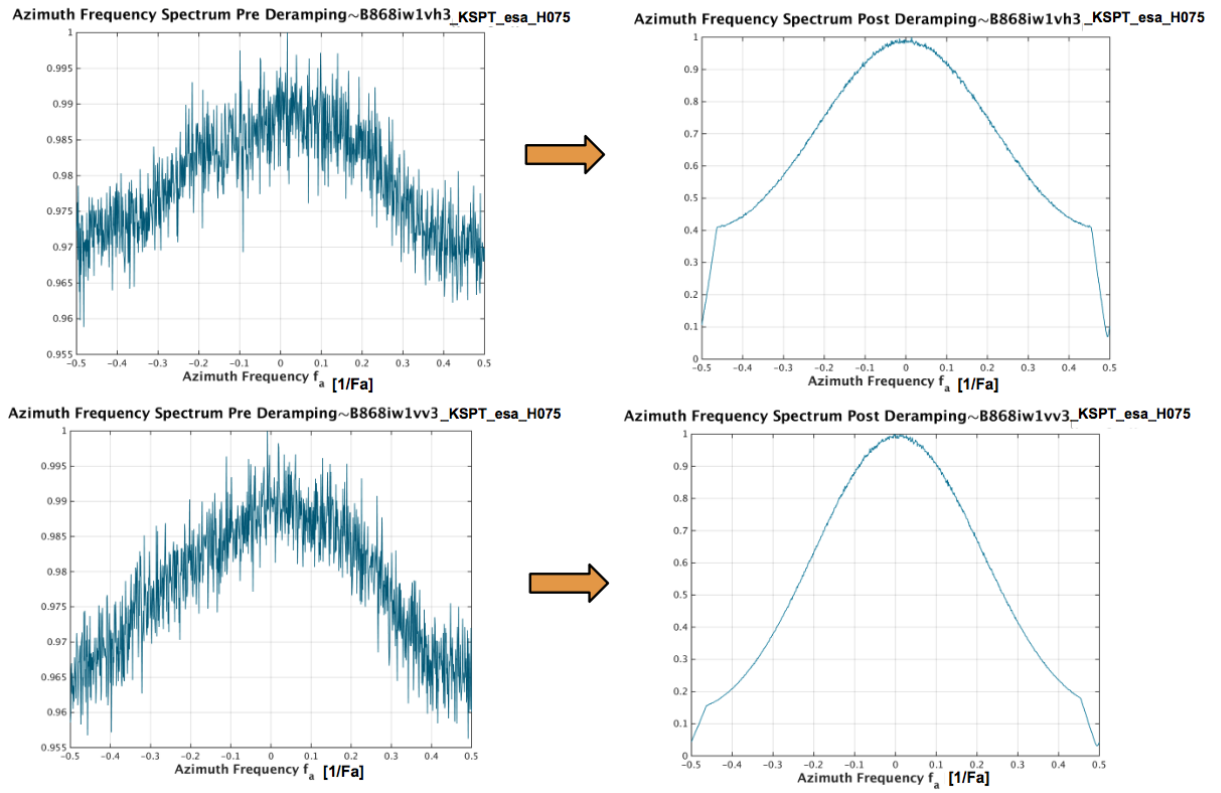


Figure 3.13: Deramping SLC product focused by NRTSAR, (burst 3, IW1 from scene B868)

Left: Original Spectra after processing with NRTSAR

Right: Spectra after deramping

Upper row, VH polarization

Lower row, VV polarization

/4

Ship detection

Ships and other ocean features were first explored in spaceborne SAR images at the launch of the SEASAT SAR system in 1978. This satellite was specially designed to image the ocean [35]. Since then a lot of research and different ship detection algorithms have been proposed. In this thesis, *products* suitable for ship detection is investigated. The actual ship detection is separated into two main parts. First, a test statistic is made and then a hypothesis test is stated. This thesis concerns the first part. The algorithms explored in this chapter produce new images that serves as a test statistic and is closely related to ship detection.

This chapter begins with describing the important SAR parameters regarding ship detection. Section 4.1 and 4.1.1 describes the SAR imaging of ocean, and ships respectively. Section 4.2 presents the quality measures commonly used to describe the ship to sea contrast, and speckle level. For the sake of completeness, the actual ship detection is described in section 4.3. Section 4.4 describes the *subaperture processing algorithms* followed by section 4.5 that deals with relevant polarimetric algorithms. Lastly, section 4.6 presents the ship detection potential for Sentinel-1 TOPS mode data.

4.1 SAR imaging of the ocean

In order to evaluate how well TOPS data are suited for ship detection it is interesting to see how the sea surface is imaged by SAR. In many ship detection algorithms the contrast between the background (ocean) and the ships are of concern, and thus it is important to understand the behavior of ocean backscatter. The high *dielectric constant* of water results in low penetration depth of microwaves and we have high reflectivity.

The ocean roughness determines how much of the signal that is backscattered to the radar. In general the ocean will appear dark on a SAR image because of low backscattering. As stated in section 2.5 the ocean roughness is dependent on the height variation of the surface in relation to the radar *wavelength or frequency*.

Wind is an obvious factor regarding the roughness of the sea. In Crisp et al. [35] the relation between the normalized radar cross section σ^0 and the wind speed v_s for a given radar incidence angle was given as:

$$\sigma^0 = |v_s|^\gamma \quad (4.1)$$

where γ is a function of radar wavelength and other such parameters. This shows a general tendency of high wind speed leading to more ocean backscatter.

The wind direction will also affect the strength of the backscatter. It is stated in Vahon et al. [36] that wind towards the radar results in stronger σ^0 compared to wind blowing away from the radar and that wind blowing across the scene result in the smallest σ^0 . Increase in *incidence angle*, referring to figure 2.1, results in a decreasing σ^0 .

The knowledge about the ocean wind and waves is important in ship detection because it can help in the selection of parameters, the evaluation of the the detection algorithm, but also give higher order information. The sea condition affects shipping routes and certain ships will most likely not be found in certain sea states. One may consider the ocean as a two-scale wave model where one consider short waves superimposed onto the larger swell waves. The smaller waves, are called ripple waves and these are related to the ocean roughness.

For incidence angles above 20 degrees, which is usually the case for operational SAR systems, the *Bragg resonance* in equation 2.17 is predominant and represents the ripple waves [35]. Equation 2.17 shows that both the incidence angle and the radar frequency changes the Bragg wavelength, and hence the ocean backscatter. Regarding the *motion effects* caused by the ocean waves,

Robinson et al. [37] claims that only the orbital motion of large swell waves will have an effect on the resulting SAR image. Depending on the viewing geometry, the orbital motion leads to a varying azimuth shift throughout the wave cycle which leads to the effect called *velocity bouncing*. This effect will not be significant for range traveling waves.

The *polarization* will also effect the ocean reflectivity. Acquisitions done in the VV polarization usually record more ocean reflectivity than in the HH channel, where the difference depends on the radar incidence angle [35] [36]. Oceanographic phenomena and other manmade objects that are likely to be found in the sea, such as heavy rain, ocean swell, sea ice, ship wakes, islands and oil rigs, can have similar backscattering behavior as ships or create image features that cause false alarms.

4.1.1 SAR imaging of Ships

In a SAR image, ships will in most cases stand out from the background as bright areas compared to the darker ocean background. The spatial *resolution* related to the ship size determines if the ship is detectable or not. The radar backscattering from ships depends on several factors regarding the ship, the surrounding area and sensor features. The important ship characteristics are the size, construction material and orientation relative to the radar. Sensor features relevant for detecting ships are, except for resolution, the polarization and incidence angle. Studies done on Radarsat-2 data have shown that the VH polarization is most suitable for ship detection when one is looking for the best contrast between the ship and the ocean [38]. This is because the ocean backscatter is lower in the VH polarization compared to the HH and VV polarization.

Ships are typically constructed by large metal sheets and comprise complex structures which result in a combination of dihedral and trihedral surface scattering mechanisms [39]. Whether or not the ship is loaded or not will also affect the radar cross section σ . Ships that have heavy loads lay lower in the water and will have a lower backscatter signal. Ships are usually accompanied by wakes and these can be used to verify that the detection is correct. Sometimes these are more detectable than the ship itself since it can cover a large area. Information regarding the image area may also be of interest, e.g., ships in oceans will in most cases be of greater size and are constructed with different materials than those located on the coast. Modelling the SAR signature of a ship is a complex task, which must also consider the radar viewing geometry. Therefore most of the literature on ship detection algorithms is based on modeling the sea backscatter alone.

4.2 Contrast Measures

In order to evaluate the quality of the ship detection products, different contrast measurements is used in the literature. This section will explain the contrast measurements used in the experimental part in section 6.1 and 6.2.

4.2.1 Target to clutter ratio

Signal to clutter ratio [40] or target to clutter ratio (TCR) is a ratio used to measure the detectability of a target embedded in ocean clutter. In conjunction with research on the polarization most suitable for ship detection, Jeremy et al. [35][41] measured TCR defined as:

$$TCR = \frac{\sigma_T}{N\sigma_C^0}, \quad (4.2)$$

where σ_T is the target RCS, N is the number of pixels in the RCS, and σ_C is the mean RCS of the ocean clutter.

4.2.2 Peak to clutter ratio

Peak to clutter ratio (PCR) is defined in Vachon et al. [42] ,

$$PCR = \frac{\max(\sigma_{target})}{\mu_{background}}, \quad (4.3)$$

where $\max(\sigma_{target})$ is the largest RCS in the defined target area, and $\mu_{background}$ is the mean RCS of the selected ocean area. PCR is also mentioned in Brekke et al.[43] when analyzing the ship to sea contrast in different polarization channels as a function of incidence angle.

4.2.3 Coefficient of variation

The coefficient of variation CV is a measure of the heterogeneity of an area. It can be used to evaluate the reduction of speckle over the different subaperture separations. The CV is defined as the standard deviation of the background area RCS, $\sigma_{background}$, divided by $\mu_{background}$:

$$CV = \frac{\sigma_{background}}{\mu_{background}} \quad (4.4)$$

We wish that there is little variation in the background, and thus the $\sigma_{background}$ must be low, and the $\mu_{background}$ high in order to have a heterogenous area.

4.3 Constant False Alarm Rate

The conventional method for ship detection is to use constant false alarm rate (CFAR). This is an *adaptive threshold algorithm* designed to search for pixel values which are unusually bright compared to those in the surrounding area. First a hypothesis of the sea clutter statistics is made. Here a probability density function (PDF) is estimated. The parameters belonging to this model are estimated locally in the image and a threshold for the statistic is chosen such that the decision rule is associated with a specific constant false alarm rate. Pixel values that lie above this threshold, are detected as possible ships [35].

4.3.1 Sea clutter statistics

Referring to section 4.1.1, the backscatter from ships are complex and dependent on several external factors. In practice we are not able to model the PDF of the ship distribution. Therefore we use sea clutter statistics to distinguish ships from sea. The hypothesis of an observation vector \mathbf{x} belonging to the sea clutter distribution f_{θ_0} or not can be stated as follows [44]:

$$H_0 : \mathbf{x} \sim f_{\theta_0}(\mathbf{x}) \quad (4.5)$$

$$H_1 : \mathbf{x} \not\sim f_{\theta_0}(\mathbf{x}) \quad (4.6)$$

Where H_0 is the hypothesis of \mathbf{x} belonging to the sea clutter, and H_1 that it belong to the unknown ship distribution.

In order to design a *criterion* that determines if \mathbf{x} belongs to the sea clutter or the ship, a threshold T is used, and a binary test is stated with the indication function $\phi(\mathbf{x})$.

$$\phi(\mathbf{x}) = \begin{cases} 0 & \text{if } \mathbf{x} < T \\ 1 & \text{if } \mathbf{x} \geq T \end{cases}$$

Defining the probability of false alarm as:

$$\alpha = P_{FA} = \int_{\mathbf{x} \in T} f_{\theta_0}(u) dx \quad (4.7)$$

and the probability of detection P_D as:

$$\beta = P_D = \int_{x \geq T} f_{\theta_1}(x) dx \quad (4.8)$$

Here f_{θ_1} is the unknown ship distribution, which must be evaluated by known ship positions. One wishes that the probability of detection, β , is large and the probability of false alarm, α , is as small as possible. Thus a *specified FAR* is set by the user. This is generally set at the order of 10^{-7} . The constant false alarm rate is defined as:

$$CFAR = 1 - \int_0^T f_{\theta_0}(x) dx \quad (4.9)$$

where T is the threshold. The parameters of the ocean pdf $f_{\theta_0}(x)$ are estimated locally. The threshold T is then found related to the CFAR. This means that the percentage of sea clutter pixels that exists above the threshold value is constant, while the T varies locally. When additional information about the ship is available, an *observed FAR* is used to measure the accuracy of the parameter estimation and the model assumptions [35].

In order to model the sea clutter one has to select a proper estimation window. Here it desired to avoid that target pixels interferes with the estimation and that the region selected must be as homogeneous as possible. Because of variation in the background the parameters are estimated locally in the image and a sliding window is often used. It is typical to choose a window or several separated windows that allows a "guard" area between the cell under test (CUT) and the estimation window. This is to ensure that no pixels in the estimation contains sidelobes from a possible target. This may be challenging in areas with high target density, e.g., near busy harbors and shipping routes.

The distribution hypothesized for the sea clutter depends on whether we have a single-look, or multilooked intensity image. A single-look intensity image is generally assumed to follow a negative *exponential distribution* while a multilooked intensity image is assumed to follow a *gamma distribution* [45].

Several versions of the CFAR algorithm exist, depending on how the assumption of homogeneous sea clutter is handled. In general the parameters are computed directly from the estimation window. In order to account for possible ships in the estimation window, order-statistic CFAR (OS-CFAR) and smallest of CFAR (SO-CFAR) has been used. In SO-CFAR the sampling window is divided into

subwindows where the mean is computed separately, and lastly the smallest mean is chosen. OS-CFAR ranks the pixel values in the estimation window and then a predefined value is selected. This value is selected based on the median, the minimum, the maximum, etc [46].

An iterative censoring scheme (IC) can be applied to any CFAR algorithm before the parameter estimation and threshold determination. In this method all high pixel values within a range is removed from the image before the sea clutter estimation. This allows the estimation window to be chosen near the CUT. Tao et al. [47] points out that it is uncertain how many of the removed pixels containing false alarms and that one should use *truncated statistics* to more precisely model the ocean clutter and to estimate the ocean clutter parameters.

4.4 Subaperture cross-correlation magnitude

The availability of phase information in complex data has been utilized in ship detection through measures of correlation between two subapertures. By computing the correlation between subapertures, one produces a new image that may be more suitable for ship detection with respect to higher ship to sea contrast. The literature comprises little research on how to model the ocean background from this particular output image. Anfinson and Brekke [48] investigated suitable distributions to fit the SCM data in terms of sea state, herein the gamma, Fisher and K-distribution. The K-distribution showed to fit the data best in homogeneous to moderate homogeneous sea clutter, while the Fisher distribution showed best results in heterogeneous areas. How to set the threshold, and perform ship *detection* is not addressed in this thesis. The output of various subaperture algorithms is evaluated in terms of the contrast measurements described in section 4.2 with respect to future ship detection.

This section will begin with a summary of the existing subaperture algorithms and continue with a more thorough review of the theory behind the subaperture algorithms used in the experimental part.

Splitting the azimuth Fourier spectrum in different subapertures is equivalent to splitting the beam width in azimuth direction. This is because of the linear relationship between frequency and time τ stated in equation 2.7. By dividing the azimuth Fourier spectrum in different subapertures we produce two or more images of the same scene. Each of the looks will have a reduced bandwidth, which results in a decreased azimuth resolution. When an SLC image is divided into subapertures, one obtains different imaging geometries and different look

separation times Δt_i between the subaperture images.

Alain Arnaud [49] was the first to apply this in the context of ship detection. The main idea is that ships have a higher phase coherence than the surrounding sea, since they are relatively stationary compared to the ocean waves. This is illustrated in figure 4.2. Arnaud refers to the raw data, and in the azimuth Fourier domain the data are split into two non-overlapping sub-sets with 25% of the bandwidth centered on positive and negative frequencies. The sub-sets are denoted as subapertures, since it is equivalent to splitting the physical beam into different sections. The split up is illustrated in one dimension in figure 4.1. Here the orange shaded area represents the frequencies for each subaperture.

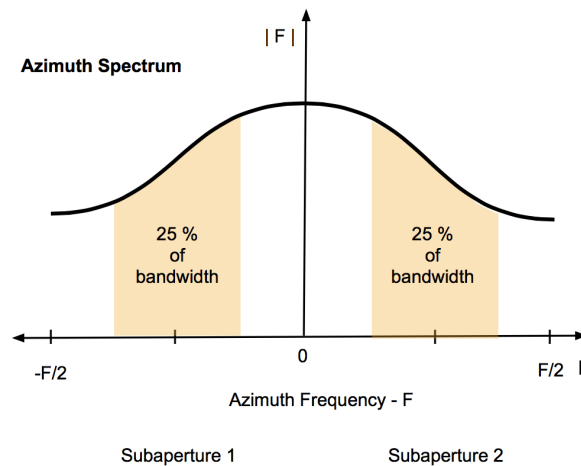


Figure 4.1: Illustration of the deviation of subapertures from the azimuth spectrum, as described in [49]. Here two subapertures (orange) covering 25% of the total bandwidth. Each subaperture is centered on negative and positive frequencies.

This produces two uncorrelated raw data sets that are further processed into two complex images. From these images, a single coherent image is produced by measuring the phase difference from pixel to pixel by a moving window. The measure of coherence varies between 0 to 1 where 0 is low coherence and 1 is high coherence. In order to classify the pixels, a threshold on the coherence is specified and pixels with coherence value above the threshold are classified as ships. Arnaud points at different improvements that can make this method more fine-tuned. In calm sea, both the separation and bandwidths of each subaperture must be broadened to ensure decorrelation of the sea. The

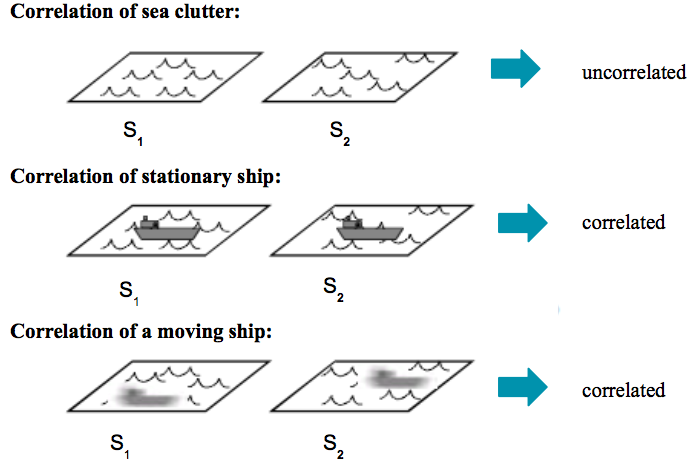


Figure 4.2: Illustration of a window from each subaperture S_1 and S_2 . When the subapertures covers ocean, the result is uncorrelated, while it is correlated when a coherent target is present. Figure taken from [50].

window size will also influence the coherence measure, and can thus be varied to improve the detection.

The use of the two-look Internal Hermitian Product (2L-IHP) was introduced by Souyris et al. [2] based on the principles of Arnaud [49]. The abbreviation 2L-IHP, or simply IHP, is commonly found in the literature but a more precise notation is the subaperture cross-correlation magnitude (SCM) which was introduced in [1]. This notation will be used from now on. Letting S_1 and S_2 define two sub-looks, the subaperture cross-correlation between two complex values s_1 and s_2 are defined as:

$$\rho = \langle s_1 \cdot s_2^* \rangle \quad (4.10)$$

where $\langle \cdot \rangle$ is a spatial averaging and the superscripted $*$ denotes the complex conjugation. The azimuth frequency spectrum is first separated into two subapertures named "azi-left" and "azi-right", the ρ is computed between the two producing a new image called ρ_{azi} . The same procedure is done by splitting the range spectra in two subapertures and compute ρ_{rge} . Finally ρ_{azi} and ρ_{rge} may be added incoherently. Thus ρ can be computed by splitting the aperture in azimuth, in range, or in both. Before applying the SCM-algorithm the SLC image is Doppler centroid corrected and a prewhitening filter is used. The center frequency of each look is aligned with each other to avoid a destructive effect of phase ramp. Souyris et al. also mention that nonstationary targets may only be visible in subparts of the spectrum and suggest a re-iteration of the process by splitting the specters further in half. This method was applied

on simulated SAR data in [51] followed by a CFAR algorithm. The results were compared to the results with a CFAR algorithm applied directly on a SLC image, with the conclusion of better detection when SCM was used.

In Johnsen and Larsen [52] A SCM image was computed from ASAR IMS SLC products before a two parameter CFAR was applied. Their results showed that the SCM image gave better TCR compared to a intensity image. Their results also showed that splitting in azimuth only gave the best overall spatial resolution and target details.

A range of different strategies to vary the subaperture bandwidth to obtain optimized results based on the sea state have been evaluated in [1]. It was found that the subaperture could have a partial overlap and still give high contrast between the ship and the ocean. They point out that in the case of overlap between the subapertures, the SCM will be undersampled, and thus an upsampling procedure is required prior to the cross-correlation computation. This leads to an improved SCM algorithm, which they name the SCM+. Hereafter this algorithm will be denoted as the SCM.

4.4.1 Algorithm 1: Subaperture Cross-correlation Magnitude

The SCM algorithm is well described in [1]. The SCM algorithm is computed for various subaperture separation times. In order to allow subapertures to overlap, they introduce upsampling, low-pass filtering and downsampling. Their dataset included three SLC quadrature polarimetric images of the same ship acquired at three different dates. The different images have slightly varying meteorological features, such as windspeed and wave height. The outline of the algorithm is shown in figure 4.3.

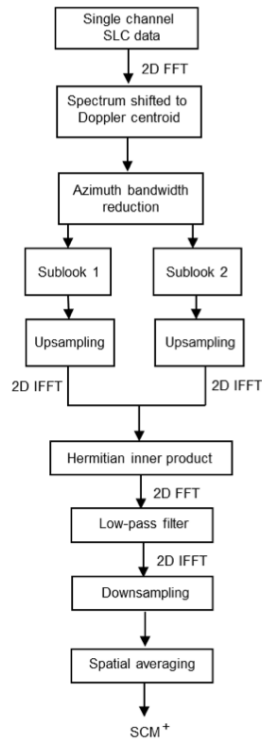


Figure 4.3: Flowchart of the SCM algorithm, taken from [1]

In the first processing stage of the algorithm the azimuth frequency spectrum is corrected. This is done by shifting the azimuth spectrum by the estimate of f_{ac} . The azimuth spectrum is then reduced to a bandwidth B . In stage four the subapertures are extracted in a manner visualized in figure 4.4.

Both subapertures are assigned the same fraction of B . Each subaperture starts at one end point of the azimuth frequency spectrum and stretches towards the other endpoint. This means that in the case where each subaperture covers 10% of B , they also contain the highest frequencies in the spectrum. The left spectrum in figure 4.4 shows two subapertures together covering 25% of B . The middle spectrum shows two subapertures covering the total available bandwidth B but with no overlap. The right spectrum shows how the overlap extends above the zero frequency point. Here each subaperture covers 75 % of B .

Brekke et al. define the normalized subaperture bandwidth $\beta = B_s/B$ where B_s is the bandwidth of each subaperture. The algorithm is run for β ranging from 0 to 1. $\beta = 1$ means total overlap of the subapertures, and $\beta = 0.5$ represents the boundary region where there is no overlap of the subapertures.

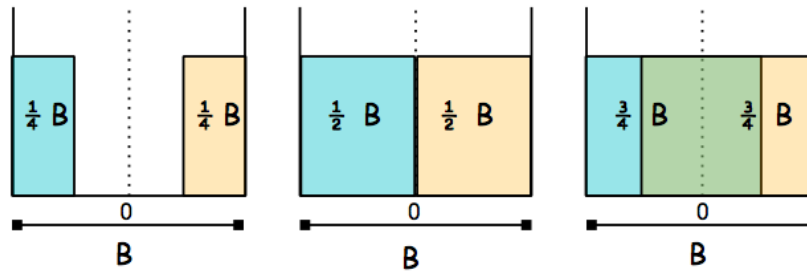


Figure 4.4: Extraction of subapertures from the azimuth frequency spectrum[1]. B : available bandwidth. In the left spectrum, two subapertures covering 25% of B is extracted. The middle spectrum shows two subapertures covering the total available bandwidth B . The right spectrum shows how the overlap extends above the zero frequency point. Here each sub aperture covers 75 % of B . Figure taken from [1]

The upsampling is done by zero-padding each subaperture to double size in both azimuth and range direction. The center frequency f_0 of each subaperture is then aligned before the subapertures are converted back to the spatial domain by an Inverse Fast Fourier Transform (IFFT). In the spatial domain the cross-correlation is computed between the subapertures by equation , except from the spatial averaging. A lowpass filter is then applied. The lowpass filter is defined from $-B/2$ to $B/2$ meaning that the resulting bandwidth of the image will never exceed the available bandwidth B .

Downsampling is executed in the spatial domain by discarding every other pixel in azimuth and range direction. This gives an image with equal size of the original image. Lastly the spatial averaging is done by a moving window. The performance of the algorithm is evaluated by the TCR and CV described in section 4.2.1 and 4.2.3, computed as a function of β . The single look intensity (SLI) image is calculated as $SLI = S_1 \cdot S_1^*$ when $\beta = 1$, such that $S_1 = S_2$. Brekke et al. mention that the SLI image will be aliased since it is equivalent to subaperture processing with total overlap between the subapertures. They define an improved SLI, referred to as SLI+. SLI+ is the output of the SCM algorithm when $\beta = 1$ and when the last averaging step is excluded.

Brekke et al. [1] compare the speckle levels by computing CV for the SLI and SLI+, and conclude that the SLI+ is an improvement in terms of speckle content. The TCR computed from the SLI+ is then used as a reference for the TCR results computed as a function of β . The SCM was computed for VV, VH and HH polarizations separately. Their results showed that the TCR varied between the dates. For the image with largest wave height, the largest TCR was located at $\beta > 0.5$. Regarding the other images, the peak TCR had varying

location. Here they point out that the different orientation and incidence angle at the ship location could have an impact on the peak point.

4.5 Polarimetric contrast enhancement methods

Polarimetric ship detection commonly utilizes the complex elements of the polarimetric scattering matrix defined in section 2.7. This section describes the polarimetric extension of the SCM algorithm, the well known Polarimetric Whitening filter, and lastly a fusion of polarimetric channels used by the Norwegian Defence Research Establishment (NDRE).

4.5.1 Algorithm 2: Polarimetric subaperture cross-correlation magnitude

Souyris et al. [2] introduce the polarimetric extension of the SCM. This extension is based on an optimization scheme inherited from [53]. The algorithm was tested on airborne polarimetric image with the conclusion of better contrast between the ocean and target, compared to the traditional SCM approach. We define two complex target vectors representing each subapertures \mathbf{s}_1 and \mathbf{s}_2 :

$$\mathbf{s}_1 = \frac{1}{\sqrt{2}} \begin{bmatrix} s_{hh}^{(1)} + s_{vv}^{(1)} \\ s_{hh}^{(1)} - s_{vv}^{(1)} \\ 2s_{vh}^{(1)} \end{bmatrix} \quad \mathbf{s}_2 = \frac{1}{\sqrt{2}} \begin{bmatrix} s_{hh}^{(2)} + s_{vv}^{(2)} \\ s_{hh}^{(2)} - s_{vv}^{(2)} \\ 2s_{vh}^{(2)} \end{bmatrix}. \quad (4.11)$$

These are complex Pauli target vectors defined in equation 2.24, where the Reciprocity theorem is applied, and hence it is assumed that $s_{hv} = s_{vh}$. By averaging outer product of $\mathbf{S}_1 \mathbf{S}_2^H$ we get a 6×6 Hermitian positive semidefinite matrix \mathbf{H} :

$$\mathbf{H} = \left\langle \begin{bmatrix} \mathbf{S}_1 \\ \mathbf{S}_2 \end{bmatrix} \cdot [\mathbf{S}_1^H \mathbf{S}_2^H] \right\rangle = \begin{bmatrix} [\mathbf{H}_{11}] & [\mathbf{\Omega}_{12}] \\ [\mathbf{\Omega}_{12}]^H & [\mathbf{H}_{22}] \end{bmatrix}. \quad (4.12)$$

Here H represents conjugate transpose. $[\mathbf{H}_{11}]$, $[\mathbf{H}_{22}]$ and $[\mathbf{\Omega}_{12}]$ represent 3×3 complex matrixes given by:

$$[\mathbf{H}_{11}] = \langle \mathbf{s}_1 \mathbf{s}_1^H \rangle \quad (4.13)$$

$$[\mathbf{H}_{22}] = \langle \mathbf{s}_2 \mathbf{s}_2^H \rangle \quad (4.14)$$

$$[\Omega_{12}] = \langle \mathbf{s}_1 \mathbf{s}_2^H \rangle. \quad (4.15)$$

Both \mathbf{H}_{11} \mathbf{H}_{22} are standard Hermitian coherency matrices that contain the full polarimetric information of each separate image. $[\Omega_{12}]$ is a 3×3 matrix that in addition to polarimetric information, contains the interferometric *phase* relations of the different polarimetric channels between the two subapertures.

Equation 4.4.1 represented the scalar case where S_1 and S_2 represented scattering coefficients from subaperture 1 and 2. By introducing two normalized complex vectors which represents two scattering mechanisms, $\hat{\omega}_1$ $\hat{\omega}_2$, we can define new scattering coefficients:

$$\mu_1 = \hat{\omega}_1^H \mathbf{s}_1 \quad \text{and} \quad \mu_2 = \hat{\omega}_2^H \mathbf{s}_2 \quad (4.16)$$

where the scattering vectors is projected onto the normalized scattering mechanisms $\hat{\omega}_1$ and $\hat{\omega}_2$. This leads to a new expression for the polarimetric SCM ρ_{POL}^{SCM} :

$$\rho_{POL}^{SCM} = \left| \langle \mu_1 \cdot \mu_2^H \rangle \right| \quad (4.17)$$

$$= \left| \langle \hat{\omega}_1^H \mathbf{s}_1 \cdot \mathbf{s}_2^H \hat{\omega}_2 \rangle \right| \quad (4.18)$$

$$= \left| \hat{\omega}_1^H \langle \mathbf{s}_1 \cdot \mathbf{s}_2^H \rangle \hat{\omega}_2 \right| \quad (4.19)$$

$$= \left| \hat{\omega}_1^H \underline{\underline{\Omega}}_{12} \hat{\omega}_2 \right| \quad (4.20)$$

ρ_{POL}^{SCM} depends on $\hat{\omega}_1$ and $\hat{\omega}_2$, which can be tuned locally to maximize the magnitude of ρ_{POL}^{SCM} and thus increase the contrast. In order to optimize $\hat{\omega}_1$ and $\hat{\omega}_2$ we use the complex Langrangian:

$$L = \hat{\omega}_1^H \left[\underline{\underline{\Omega}}_{12} \right] \hat{\omega}_2 + \lambda_1 (\hat{\omega}_1^H \hat{\omega}_1 - 1) + \lambda_2 (\hat{\omega}_2^H \hat{\omega}_2 - 1) \quad (4.21)$$

where λ_1 and λ_2 account for the normalization constraints bearing on $\hat{\omega}_1$ and $\hat{\omega}_2$: $|\hat{\omega}_1| = |\hat{\omega}_2| = 1$. By setting the partial derivatives to zero and rearranging

the equations we end up with a eigenvalue eigenvector problem in 4.24 and 4.25:

$$\frac{\partial L}{\partial \hat{\omega}_1^H} = \left[\underline{\underline{\Omega}}_{12} \right] \cdot \hat{\omega}_1 + 2 \cdot \lambda_1 \hat{\omega}_1 = 0 \quad (4.22)$$

$$\frac{\partial L}{\partial \hat{\omega}_2^H} = \left[\underline{\underline{\Omega}}_{12} \right]^H \cdot \hat{\omega}_2 + 2 \cdot \lambda_2^* \hat{\omega}_2 = 0 \quad (4.23)$$

$$\left[\underline{\underline{\Omega}}_{12} \right] \cdot \left[\underline{\underline{\Omega}}_{12} \right]^H \hat{\omega}_1 = 4\lambda_1 \lambda_2^* \hat{\omega}_1 \quad (4.24)$$

$$\left[\underline{\underline{\Omega}}_{12} \right]^H \cdot \left[\underline{\underline{\Omega}}_{12} \right] \hat{\omega}_2 = 4\lambda_1 \lambda_2^* \hat{\omega}_2 \quad (4.25)$$

4.24 and 4.25 show that $\hat{\omega}_1$ and $\hat{\omega}_2$ are normalized eigenvectors of the Hermitian matrix $\left[\underline{\underline{\Omega}}_{12} \right]^H \cdot \left[\underline{\underline{\Omega}}_{12} \right]$ and $\left[\underline{\underline{\Omega}}_{12} \right] \cdot \left[\underline{\underline{\Omega}}_{12} \right]^H$ respectively. From the theory of Hermitian matrixes, $\left[\underline{\underline{\Omega}}_{12} \right]^H \cdot \left[\underline{\underline{\Omega}}_{12} \right]$ and $\left[\underline{\underline{\Omega}}_{12} \right] \cdot \left[\underline{\underline{\Omega}}_{12} \right]^H$ have two independent real eigenvalues, that are shown to be the same for each matrix; $v = 4\lambda_1 \lambda_2^*$.

We can show that the relation between $\hat{\omega}_1$ and $\hat{\omega}_2$ is:

$$\hat{\omega}_2 = \alpha \left[\underline{\underline{\Omega}}_{12} \right]^H \hat{\omega}_1, \quad (4.26)$$

where $\alpha = \frac{1}{\sqrt{v}}$.

This means that by computing the maximum eigenvalue v_{max} of $\left[\underline{\underline{\Omega}}_{12} \right]^H \cdot \left[\underline{\underline{\Omega}}_{12} \right]$, we find the corresponding $\hat{\omega}_{1max}$ and $\hat{\omega}_{2max} = \frac{1}{\sqrt{v_{max}}} \left[\underline{\underline{\Omega}}_{12} \right]^H \hat{\omega}_{1max}$,

and the maximum value of ρ_{POL}^{SCM} is:

$$\max(\rho_{POL}^{SCM}) = \hat{\omega}_{1max}^H \begin{bmatrix} \underline{\Omega} \\ \underline{\Omega}_{12} \end{bmatrix} \hat{\omega}_{2max} \quad (4.27)$$

$$= \frac{1}{\sqrt{v_{max}}} \hat{\omega}_{1max}^H \begin{bmatrix} \underline{\Omega} \\ \underline{\Omega}_{12} \end{bmatrix} \begin{bmatrix} \underline{\Omega} \\ \underline{\Omega}_{12} \end{bmatrix}^H \hat{\omega}_{1max} \quad (4.28)$$

$$= \sqrt{v_{max}} \quad (4.29)$$

where $(\hat{\omega}_{1max}, \hat{\omega}_{2max})$ is the eigenvector pair associated with v_{max} .

4.5.2 Algorithm 3: Polarimetric whitening filter

The polarimetric whitening filter (PWF) is defined in Novak et al. [54]. The main idea behind this whitening filter is to minimize the *CV* ratio of the image clutter. This means that the goal is to create an image with less speckle content. They assume a fully polarimetric Gaussian clutter model. Evaluation of the PWF for non-Gaussian clutter showed that the PWF is optimal when the *CV* ratio is considered.

First they define the *complex* backscatter in each polarization channel in vector \mathbf{x} :

$$\mathbf{x} = \begin{bmatrix} HH \\ HV \\ VV \end{bmatrix} \quad (4.30)$$

They wish to construct an image y of the form:

$$y = \mathbf{x}^H \underline{\underline{\mathbf{A}}} \mathbf{x} \quad (4.31)$$

where $\underline{\underline{\mathbf{A}}}$ is a Hermitian symmetric positive definite matrix. They show that in order to minimize the *CV* ratio, $\underline{\underline{\mathbf{A}}}$ represents the inverse covariance matrix Σ^{-1} of HH, HV and VV. Thus the PWF is defined as:

$$y = \mathbf{x}^H \underline{\underline{\Sigma}}^{-1} \mathbf{x} \quad (4.32)$$

In Novak et al. the PWF was used *adaptively* in terms of target detection. Here sample covariance are estimated in a neighborhood surrounding the pixel represented by \mathbf{x} . The estimator is defined as:

$$\hat{\underline{\Sigma}} = \frac{1}{n} \sum_{k=1}^n \mathbf{x}_k \mathbf{x}_k^H. \quad (4.33)$$

where n is the number of samples.

4.5.3 Algorithm 4: Aegir with fusion of polarimetric channels

The fourth algorithm is not specially designed for complex data, but similar to the PWF and POL-SCM, it fuses two polarimetric channels. This algorithm have shown good results and it is in operational use by NDRE, which have long experience in ship detection. Therefore it is natural to evaluate this algorithm against the other polarimetric algorithms.

Ever since 1998 the Norwegian authorities have used SAR to monitor ship traffic, oil spills and sea ice in the High North. Their main source of information has been from RADARSAT-1 and RADARSAT-2 satellites. NDER have developed an automatic ship detector, called Aegir [55]. Aegir analysis each polarization channel separately or combines two polarization channels to improve the ship to sea contrast. When fusing two polarimetric channels they use the following formula, developed by Eldhuset [56]:

$$y = \frac{|A_{co-pol}| \cdot |A_{cross-pol}|}{const} \quad (4.34)$$

This is a heuristic formula, where y is the output image, $|A_{co-pol}|$ is the absolute value of the co-pol amplitude image, $|A_{cross-pol}|$ is the absolute value of the cross-pol amplitude image. $const$ represents a unknown constant. In this thesis the constant is the arithmetic mean of the imageproduct: $|A_{co-pol}| \cdot |A_{cross-pol}|$. Hereafter this algorithm will be adressed as *Aegir-Pol*.

4.6 Ship detection adaption to Sentinel-1 TOPS mode

Ocean surveillance is one of the main goals of the Copernicus program and Sentinel-1 marine application potential was analyzed in Vachon et al. [57]. Their focus is on the IW mode, which is the default mode over coastal areas. In

the analysis they used a CFAR algorithm where the ocean clutter background where modeled with a K-distribution. The analysis concludes that *IW mode* is suitable for ship monitoring scenarios, but that smaller incidence angles is preferable in order to detect wakes. SLC data produces by Sentinel-1 IW mode, operates with the polarizations VV and VH. With reference to section 4.1.1 the ocean backscatter is low in VH compared to co-pol channels and thus VH is optimal for ship detection regarding ship to ocean contrast. The next sections will analyze in more detail the potential of Sentinel-1 TOPS mode ship detection regarding imaging zones where bursts overlap and limitations of the relative short dwell time.

4.6.1 Ship detection in TOPS mode overlap regions

The imaging geometry of TOPS was described in section 3.2 and illustrated in figure 3.3. When considering two successive bursts, there will be an overlap area where their ends meet in azimuth. There also exists an overlap between subswaths, where two range ends meet, but this overlap will not be evaluated here.

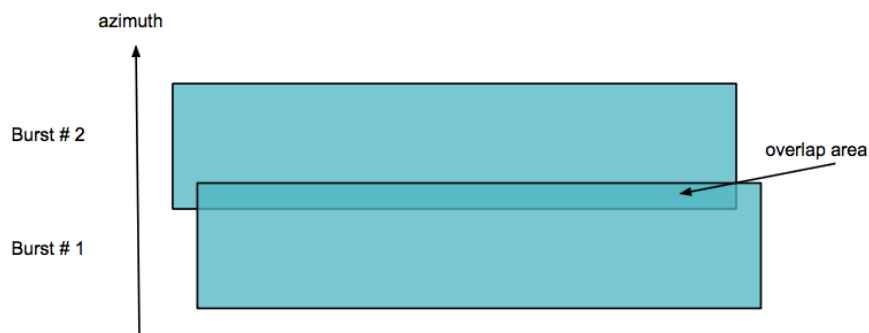


Figure 4.5: Overlap area in azimuth of two successive bursts

A target that is located in this overlap zone, is consequently illuminated twice with a time separation T_R . Greindanus et al. [8] mention the possibility of measuring the speed and course of possible targets in this region, but that only a fraction of targets in the image could make use of this effect. How to access this information was explained in section .

4.6.2 NRTSAR Processing parameters

NRTSAR allows adjustments of several processing parameters that are fixed in ESA's standard IPF processor. Generally the choice of the processing window function and window coefficients is made to satisfy a multidisciplinary scientific community. In the context of subaperture ship detection, Souyris et al. [2] mentioned the use of a prewhitening filter in order to reduce the sidelobes from strong point targets and hence remove the correlation between the pixels. Considering the CFAR algorithm, a final threshold is set based on estimating the parameters of a predefined ocean clutter distribution. By lowering the pixel to pixel correlation, we may get more accurate parameter estimates. With this in mind, it may be sensible to process an image with a Hamming window of lower coefficients than ESA IPF and investigate if this has any effect of the ship detection performance. ESA IPF uses Hamming window coefficients of 0.7 – 0.75. Referring to section 3.3.2 and table 3.2 we see that lower Hamming window coefficients, e.g., 0.65 and 0.52 yields better PSLR and ISLR at the expense of degraded resolution. A Hamming window with coefficients of 0.5, 0.65 and 0.75 is therefore used in the experimental part. Increasing the processing bandwidth B_a , results in maximum dwell time, which may be favorable in subaperture ship detection since the interlook time difference between the subapertures is increased. The effect of processing with full bandwidth is explored in the experimental part.

4.6.3 TOPS Dwell time

SAR images acquired in TOPS mode have short dwell time due to the azimuth steering which leads to a shrunken footprint compared to standard stripmap. Studies have shown that the ripple waves of open ocean need 0.05 s or less to decorrelate in a C-band SAR image, this time is also referred to as the *the ocean coherence* time by [58]. Considering this generalized case, this means that the separation between the center times T_i in each subaperture i must be longer than 0.05 in order for the ocean to decorrelate.

Ouchi et al. [58] claims that if the background scatter is modeled as a statistically white stochastic process, meaning that the speckle is Gaussian, the cross-correlation function (CCF) between the subapertures is *independent* of the sea coherence time. In this case the CCF is only dependent on the *weighting function* of the subapertures, the dwell time T_D , and the time difference between the center frequencies in each subaperture, $\Delta T = T_{i+1} - T_i$. The results show a steady decrease in the intensity cross-correlation between subapertures with increasing ΔT . Ouchi et al. further argues that if the cross-correlation function were dependent on the sea coherence time one would have experienced decorrelation at time lags of similar order. However this is not observed

in their results.

The dwell time is denoted as the synthetic aperture length Δx_a , referring to equation 2.4, divided by the sensor velocity V_s :

$$T_D \approx \frac{\Delta x_a}{V_s} \approx \frac{\lambda R_0}{V_s A_A}. \quad (4.35)$$

In equation 4.35, any squint angle is neglected, thus R_0 is the slant range in the zero Doppler plane referring to figure 2.1. The $3dB$ width of the radar beam is approximated by λ/A_A . From section ?? the TOPS antenna is illuminating a target with a footprint on the ground that is shrunk by a factor α , which means that the antenna length A_A must be multiplied by α .

$$T_D \approx \frac{\lambda R_0}{V_s \alpha A_A} = \frac{\lambda R_0}{A_A (V_s + R_0 |k_\phi|)}. \quad (4.36)$$

The dwell time can also be thought of as the time that it takes for the azimuth chirp to cover one PRF of the frequency band. In the experimental part different focusing bandwidths will be evaluated and thus it is convenient to express the dwell time in terms of the Doppler bandwidth B_a :

$$B_a = \frac{2V_s}{A_A}. \quad (4.37)$$

Also here any squint angle is neglected and the $3dB$ width of the radar beam is approximated by λ/A_A . The dwell time for a target acquired in TOPS mode can then be expressed as:

$$T_D \approx \frac{\lambda R_0}{2V_s^2 \alpha} B_a = \frac{\lambda R_0}{2V_s (V_s + R |k_\phi|)} B_a. \quad (4.38)$$

/5

Data

The data set used in this thesis come from four different scenes: Two scenes from the south-west coast of Norway, one scene from Bremerhaven, Germany and one scene from Portsmouth, England. Each scene has two data sets: one in SLC format and one in unfocused raw format. The raw data are focused by Kongsberg Spacetec NRTSAR processor to produce SLC images for the four scenes that are used in the comparison. Several subimages are extracted for the experimental part. The following sections describes the Sentinel-1 acquisition modes and data formats, and presents the four scenes and the chosen subimages.

5.1 Sentinel-1 acquisition modes

Sentinel-1 has four different acquisition modes; Stripmap, Wave mode, IW mode and EW mode shown in figure 5.1. According to Greidanus et al. [8] IW and EW will mostly be used, while stripmap is only reserved for emergencies and disasters. The data used in the experimental part will therefore only consider the IW mode which is used routinely over ocean.

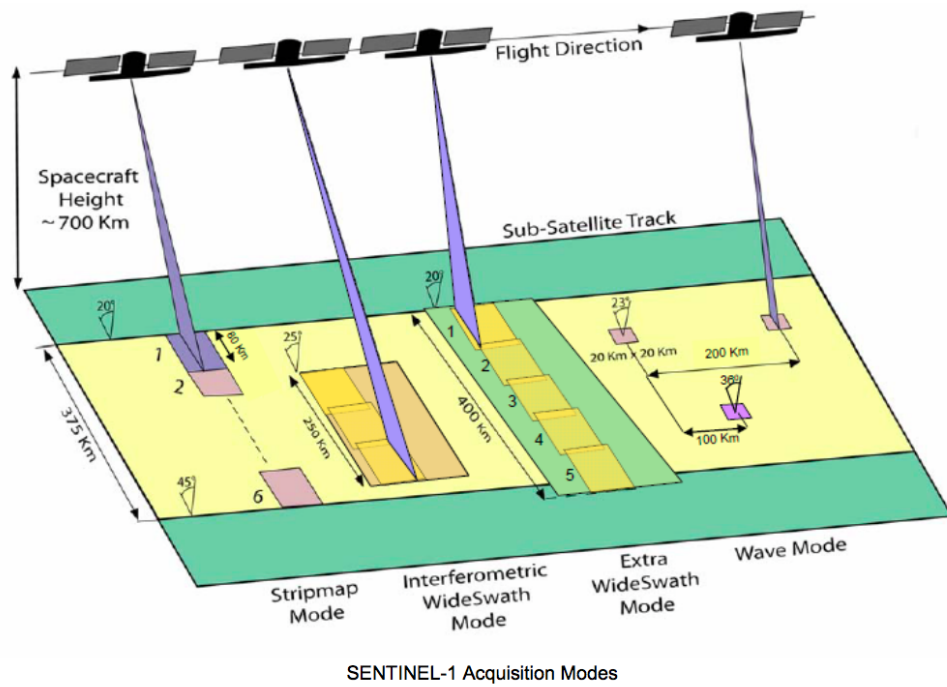


Figure 5.1: Acquisition modes for Sentinel-1, image from [59]

Sentinel-1 Payload	
System Parameter	Value
Radar Carrier Frequency	5.405 GHz
Antenna Length	12.3 m
Antenna Width	0.82 m
Azimuth Beam Steering Range	-0.9°– 0.9°
Elevation Beam Steering Range	-13°– 13°
Elevation Beam Width	3.43°
Azimuth Beam Width - θ_{open}	0.23°
Incidence Angle Range	20°– 46°
Pulse Repetition Frequency	1000 Hz – 3000 Hz

Table 5.1: System parameters for Sentinel-1, table is adapted from [60]

Sentinel-1 Acquisition Modes					
	Polarization	Swath Width [km]	Incidence Angle [°]	Azimuth Resolution [m]	Range Resolution [m]
Stripmap	Single or Dual	375	18.3 - 46.8	5	5
IW	Single or Dual	250	29.1 - 46.0	20	5
EW	Single or Dual	400	18.9 - 47.0	20	40
Wave Mode	Single	20	21.6 - 25.1 and 34.8 - 38.0	5	5

Table 5.2: Details for Sentinel-1 acquisition modes, table is adapted from [60]

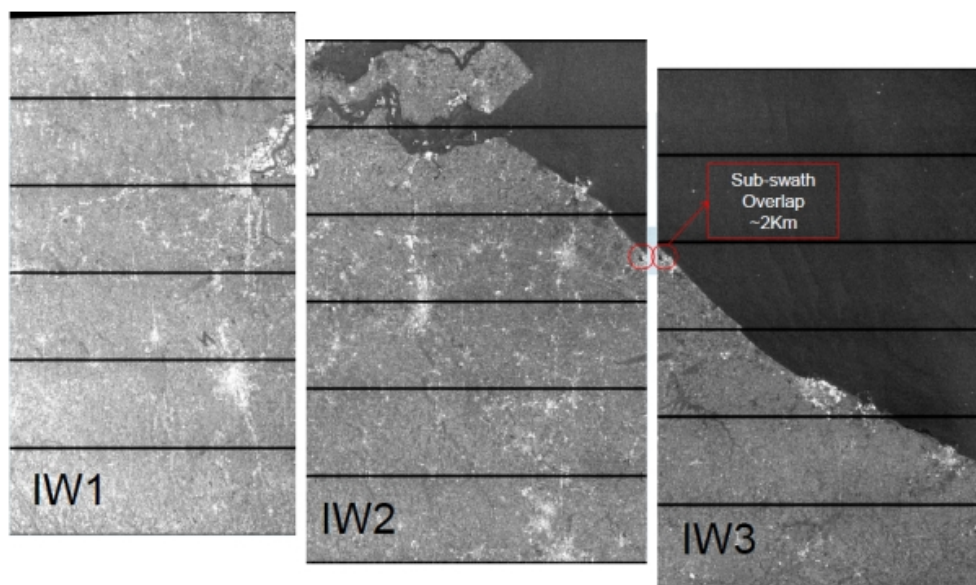


Figure 5.2: SLC image for IW mode consisting of three sub swaths with six bursts each. IW1 represents the subswath in near range, and IW3 represents the subswaths in far range. Image taken from [61]

5.2 Data formats

The data formats provided by Sentinel-1 are defined by three processing levels. The level 0 products are *raw data* products. The level 1 products are SLC images focused by the algorithm in section 3.2.3 and multilooked ground range detected (GRD) products that are irrelevant for this project.

In the SLC image each subswath consists of a series of burst, where each burst is processed as a separate SLC image. The focused bursts are assembled in azimuth time into a single subswath image with black-fill demarcation in between. Figure 5.2 shows an illustration of this effect for the IW mode. Each burst has a general dimension of 1500×20000 pixels, and for the sub images selected in the experimental part only specific bursts are considered.

5.3 Scenes

The experimental part consists of images taken from four different areas represented in table 5.3 and table 5.4. The orange shaded area shows the geographical area of the scene. The raw data area is larger than the SLC image area. This is because only parts of the data are used to form a SLC image.



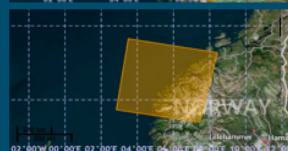
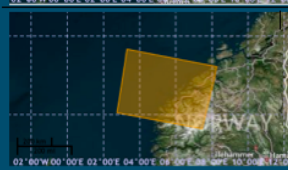
Location: The Norwegian Sea	TOPS Mode	Type	Polarization	Name:	Date	Time (Sensing)	
						Start:	Stop:
	IW	RAW	VV/VH	331F	2015-01-10	06:03:29	06:04:02
	IW	SLC	VV/VH	7BC9	2015-01-10	06:03:32	06:03:59
	IW	RAW	VV/VH	2B1B	2015-01-10	06:03:04	06:03:37
	IW	SLC	VV/VH	85B5	2015-01-10	06:03:07	06:03:34

Table 5.3: System parameters for scenes covering the Norwegian Sea. The table show details for both SLC format and raw format, Sentinel-1 IW mode. Details taken from metadata of each product. Images retrieved from ESA's Sentinel-1 Scientific Data Hub [62].

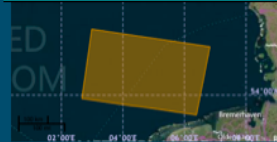


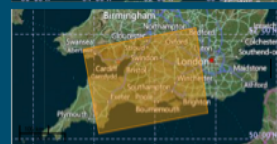
Location: Bremerhaven and Portsmouth	TOPS Mode	Type	Polarization	Name	Date	Time (Sensing)	
						Start:	Stop:
	IW	RAW	VV/VH	CBCF	2015-01-17	05:57:11	05:57:32
	IW	SLC	VV/VH	B868	2015-01-17	05:57:14	05:57:33
	IW	RAW	VV/VH	F722	2015-03-24	17:57:07	17:57:39
	IW	SLC	VV/VH	639D	2015-03-24	17:57:09	17:57:36

Table 5.4: System parameters for scenes covering Bremerhaven, Germany and Portsmouth, England. The table shows details for both SLC format and raw format, Sentinel-1 IW mode. Details taken from metadata of each product. Images retrieved from ESA's Sentinel-1 Scientific Data Hub [62]

5.4 Subimages for subaperture cross correlation magnitude analysis

Eighteen subimages containing an unidentified target are manually selected. The size of the subimages are varying between 200×200 and 100×100 pixels. Figure 5.5 and 5.4 shows four subimages with different ocean features. Large scale ocean waves are visible in figure 5.5 where subimage no. 15 and 18 are displayed. The rightmost image in figure 5.4 shows subimage no. 12, which is an example where little ocean features are visible.

Figure 5.3 shows subimage no. 3 with a centered target. The white corner squares shows the area which represents the background area, while the orange square indicates the target region. In general the background area are four times 50×50 pixels for images of size 200×200 pixels. In subimages of size 100×100 pixels, the background area is chosen to be four times 25×25 pixels. Table 5.5 shows the dimension details for the selected subimages.

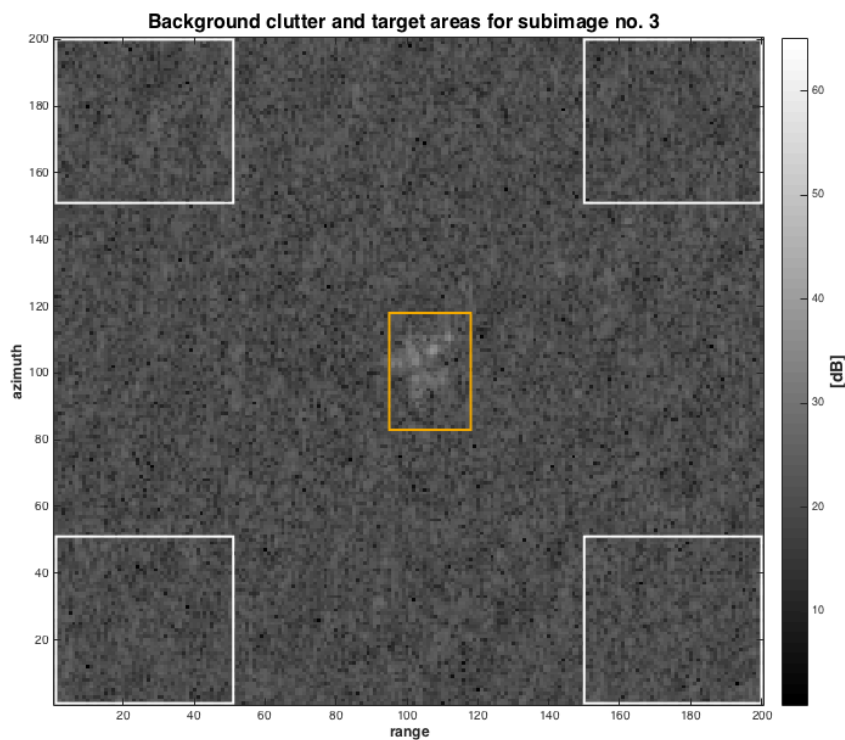


Figure 5.3

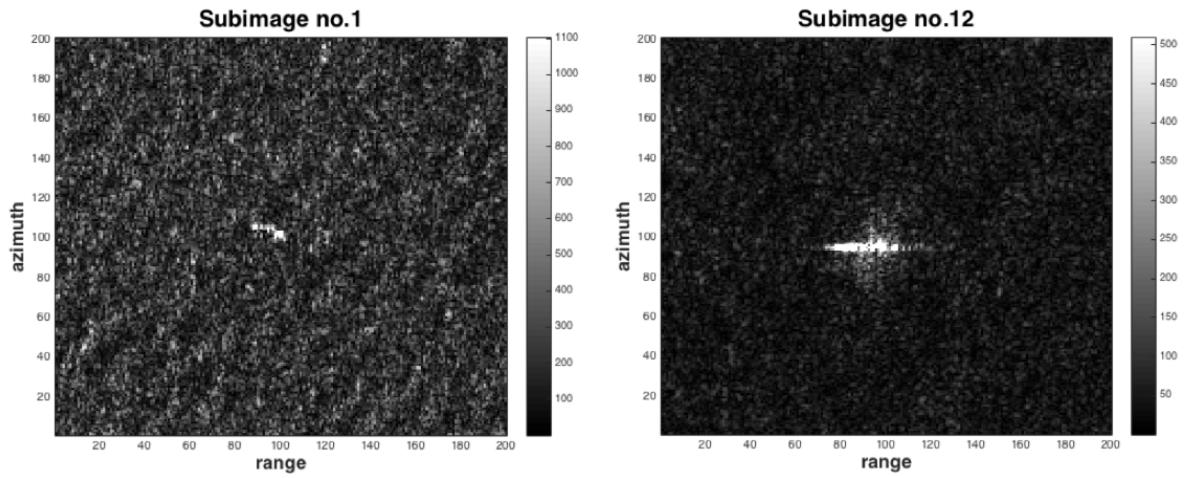


Figure 5.4: Amplitude images of VV channel representing subimage no. 1 (left) from scene B868 and subimage no. 12 (right) from scene 7BC9. The dimension of the images are 200×200 pixels and scaled such that ocean features are visible

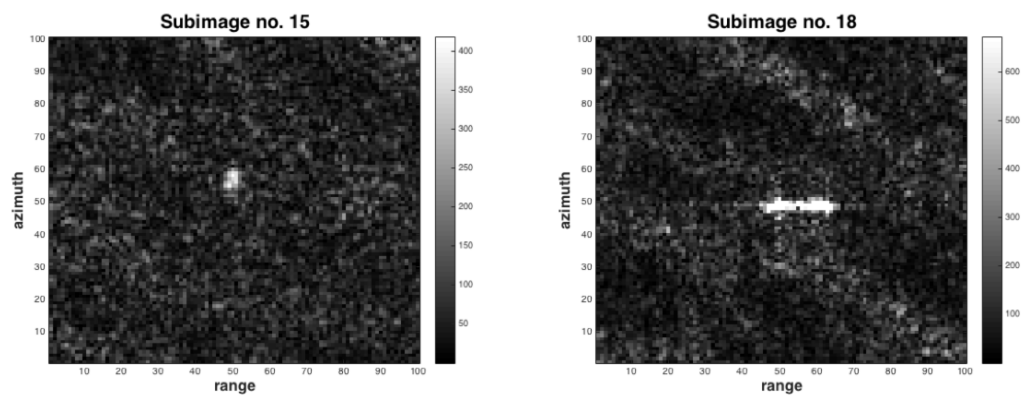


Figure 5.5: Amplitude images of VV channel representing subimage no. 15 (left) and 18 (right) from scene 85B5. The dimension of the images are 100×100 pixels and scaled such that ocean features are visible.

Scene	<i>Im</i>	Swath	B	Size Image (pixels)	Resolution (km)	Size Target (pixels)	Resolution Target (m)
B868	1	IW1	3	200 x 200	4 x 1	10 x 20	200 x 100
B868	2	IW1	3	200 x 200	4 x 1	31 x 10	620 x 50
B868	3	IW1	3	200 x 200	4 x 1	40 x 25	800 x 125
B868	4	IW1	3	200 x 200	4 x 1	35 x 15	700 x 75
B868	5	IW1	3	200 x 200	4 x 1	35 x 23	700 x 115
7BC9	6	IW2	1	100 x 100	2 x 0.5	20 x 10	400 x 50
7BC9	7	IW2	6	100 x 100	2 x 0.5	6 x 6	120 x 30
7BC9	8	IW2	6	100 x 100	2 x 0.5	10 x 10	200 x 50
7BC9	9	IW2	6	200 x 200	4 x 1	20 x 23	400 x 115
7BC9	10	IW2	6	200 x 200	4 x 1	4 x 6	80 x 50
7BC9	11	IW2	7	200 x 200	4 x 1	6 x 27	120 x 135
7BC9	12	IW3	8	200 x 200	4 x 1	8 x 20	160 x 100
7BC9	13	IW3	8	200 x 200	4 x 1	9 x 25	180 x 500
85B5	14	IW2	4	100 x 100	2 x 0.5	6 x 23	120 x 165
85B5	15	IW2	4	100 x 100	2 x 0.5	8 x 6	160 x 30
85B5	16	IW2	4	200 x 200	4 x 1	12 x 40	240 x 200
85B5	17	IW2	4	200 x 200	4 x 1	9 x 13	180 x 65
85B5	18	IW2	4	100 x 100	2 x 0.5	6 x 26	120 x 130

Table 5.5: Dimension details of subimages for subaperture cross-correlation magnitude analysis. *Im* stands for the image number and *B* is the burst number. The resolution is estimated from the pixel size.

/6

Results and Discussion

This chapter presents five experiments that try to answer the main research questions posed in this thesis.

- Experiment 1: Performance analysis of subaperture processing with TOPS data focused by ESA IPF.
- Experiment 2: Comparison of image products obtained from TOPS SLC data focused by ESA IPF.
- Experiment 3: Performance analysis of subaperture processing with TOPS SLC data focused by NRTSAR.
- Experiment 4: Comparison of image products obtained from TOPS SLC data focused by NRTSAR, with various processing bandwidths and Hamming window coefficients.
- Experiment 5: Investigation of azimuth burst overlap in TOPS SLC IW₃ data.

Each subsection starts by presenting the experiment and explain the choices made. This is followed by a result and discussion part related to each experiment.

6.1 Experiment 1: Performance analysis of subaperture processing with TOPS SLC data focused by ESA IPF.

The first experiment consists of evaluating the different subaperture algorithms described in section 4.4.1 and 4.5.1. These are processed on the 18 subimages described in table 5.5. The subimages have different size. In all scenes where there is sufficient ocean surrounding the target, the subimage is chosen to be 200×200 pixels. In situations where the target has other targets or land nearby, the subimage is chosen to be 100×100 pixels.

A polarimetric adaption of the improved SCM described in Brekke et al.[1] is done by incorporating the polarimetric extension of SCM proposed by Souyris et al. [2]. The polarimetric extension is modified to fit the dual polarization case of Sentinel-1 SLC data and a spectral prewhitening of the subapertures is explored.

The experiment is thus divided into two main stages:

- Stage 1: The SCM and POL-SCM are computed for different subaperture separations β and evaluated by TCR, PCR and CV.
- Stage 2: Prewhitening are applied to the subapertures and stage 1 is repeated.

6.1.1 Dual polarization subaperture cross-correlation magnitude

Sentinel-1 provides data with dual polarizations and the IW TOPS mode uses polarization VV and VH when acquiring SLC data. In order to get the maximum information yield from both polarizations the POL-SCM introduced in [2] and described in 4.5.1 is implemented with two-dimensional target vectors. A data fusion of the polarimetric channels VH and VV is obtained. This is done by replacing the target vectors \mathbf{S}_1 and \mathbf{S}_2 in section 4.5.1 by target vectors representing the situation of dual polarizations:

$$\mathbf{S}_{d1} = \begin{bmatrix} S_{vv}^{(1)} \\ S_{vh}^{(1)} \end{bmatrix} \quad \mathbf{S}_{d2} = \begin{bmatrix} S_{vv}^{(2)} \\ S_{vh}^{(2)} \end{bmatrix}. \quad (6.1)$$

Referring to section 4.5.1 the polarimetric SCM is computed as:

$$\rho_{POL} = \left| \hat{\omega}_1^H \underline{\underline{\Omega}}_{12} \hat{\omega}_2 \right| \quad (6.2)$$

In the dual polarization case, $\underline{\underline{\Omega}}_{12}$ represents the 2×2 complex matrix containing the interferometric phase relations to the VH and VV channels between subaperture 1 and 2. Both Pauli- and Lexciographic basis sets were investigated. Since both basis sets are linear combinations of the Sinclair matrix, the results are expected to be similar. This experiment was computed for both cases. The results showed that defining target vectors for VH and VV with Lexciographic basis yielded highest TCR for SCM-POL. One example of the TCR for subimage no. 13 is shown in the Appendix section 8.2. Equation 4.15 reduces to:

$$\underline{\underline{\Omega}}_{12} = \left\langle \left[\begin{array}{c} S_{vv}^{(1)} \\ S_{vh}^{(1)} \end{array} \right] \cdot [S_{vv}^{(2)} S_{vh}^{(2)}] \right\rangle \quad (6.3)$$

$$= \left[\begin{array}{cc} \langle S_{vv}^{(2)} \cdot S_{vv}^{(2)*} \rangle & \langle S_{vv}^{(1)} \cdot S_{vh}^{(2)*} \rangle \\ \langle S_{vh}^{(1)} \cdot S_{vv}^{(2)*} \rangle & \langle S_{vh}^{(1)} \cdot S_{vh}^{(2)*} \rangle \end{array} \right] \quad (6.4)$$

Having a closer look at $\underline{\underline{\Omega}}_{12}$ we see that the diagonal elements in the matrix are equivalent to the scalar SCM described in 4.4.1. $\underline{\underline{\Omega}}_{12}$ is not Hermitian, but real eigenvalues are obtained for the Hermitian matrix $\underline{\underline{\Omega}}_{12}^H \cdot \underline{\underline{\Omega}}_{12}$.

6.1.2 Contrast and speckle measures

In order to evaluate the resulting SCM image, TCR, PCR and CV measurements are compared for the singlelook intensity images SLI, and SLI+ and the SCM images. SLI+ is the product of the algorithm in figure 4.3 where each subaperture covers the entire available bandwidth, but the last spatial averaging step is excluded. As presented in section 5.4 and shown in figure 5.3 the background information is computed from the white corner squares and the target information is computed from the centered orange square. Both the target and background area are manually selected.

The results from the SCM analysis is presented in table 6.1. Table 6.1 shows the contrast measures TCR and PCR computed for normalized subaperture overlap β , in the range $[0.1 - 1]$. The label VH indicates that the SCM algorithm is computed only for the VH polarimetric channel, VV indicates that the SCM is

computed for the VV channel and POL indicates the polarimetric SCM algorithm which combines VH and VV. From now on the algorithms are addressed as $SCM - VH$, $SCM - VV$ and $SCM - POL$. Only the overall highest TCR and PCR for each subimage is recorded in table 6.1. Here β_{TCR} and β_{PCR} are given for the β at which the highest contrast was measured. SCM_{TCR} and SCM_{PCR} indicate which algorithm that achieved the contrast.

Scene	Im	TCR [dB]	β_{TCR}	SCM_{TCR}	PCR [dB]	β_{PCR}	SCM_{PCR}
B868	1	24.0468	0.73	VH	33.9200	0.73	VH
B868	2	12.0175	0.51	VH	20.6397	0.49	VH
B868	3	30.3606	0.69	VH	45.4718	0.69	VH
B868	4	14.5558	0.71	VH	23.3863	0.69	VH
B868	5	23.3692	0.75	VH	35.4794	0.45	VH
7BC9	6	22.8931	0.675	POL	33.1308	0.705	POL
7BC9	7	18.6380	0.705	POL	25.7442	0.705	POL
7BC9	8	17.1471	0.42	VH	26.3551	0.45	VH
7BC9	9	21.7655	0.69	VH	37.5838	0.69	POL
7BC9	10	27.3124	0.69	VH	30.5108	0.69	VH
7BC9	11	18.8381	0.71	POL	25.8677	0.71	POL
7BC9	12	34.9511	0.72	VH	42.1646	0.41	VH
7BC9	13	25.4432	0.72	VH	31.1111	0.735	VH
85B5	14	13.6893	0.69	VH	19.7495	0.69	VH
85B5	15	18.2415	0.75	POL	21.9458	0.77	POL
85B5	16	11.7884	0.71	VH	19.0171	0.72	VH
85B5	17	14.4258	0.69	VH	20.1549	0.39	VH
85B5	18	33.2724	0.675	VH	38.7828	0.675	VH

Table 6.1: TCR and PCR measurements for the SCM algorithms. VH means that the $SCM - VH$ algorithm provided best contrast measure, and POL means that the $SCM - POL$ provided best contrast measure. β is the normalized subaperture overlap ranging from $[0.1 - 1]$.

In order to visualize the PCR and TCR as a function of β , the results from two well representative subimages are shown in the following subsections. The dwell time and incidence angle measured at the center of each subimage are shown in table 6.3.

6.1.3 Contrast and speckle measurements for subimage no. 1

Figure 6.1 shows the SLC subimages corresponding to image number 1. Both images are represented in decibels in order to make it easier to visually compare the features in various subimages. The right image show the VH channel of

the subimage, while the left image show the VV channel of the subimage. It is evident that there is more ocean structure visible in the VV channel, and that the contrast between the target and the ocean is greater in the VH channel.

Recalling that the CV is a measurement of heterogeneity, the computation is done from the background region, which is represented by the white corner squares in figure 6.1. Considering figure 6.2, which shows the development of CV as a function of β , SCM-VV and SCM-POL behaves equally while SCM-VH remains at a lower CV value. This is consistent with the fact that the VV image contains more ocean structures. This also implies that the POL-SCM is strongly influenced by the scatter contribution of VV, as this trend is seen in all eighteen subimages. Compared to the CV values computed for the SLI images, all SCM algorithms greatly suppress speckle at all β . This was observed for all eighteen subimages and is consistent with the findings of Brekke et al. [1].

Regarding figure 6.3 and 6.4 both the TCR and PCR have similar behavior as a function of β . As expected, the SCM-VH reaches significantly higher contrast measures compared to SCM-VV. Naturally the PCR is higher than the TCR, since the latter accounts for the whole region of scatters within the target, while the PCR only considers the highest pixel value in the target region. In the same manner as CV, it is observed that both TCR and PCR experience a decay after $\beta = 0.73$.

The amplitude profile of the original VH subimage is shown in figure 6.5. Here we observe three peaks belonging to the target. This figure shows that initially, the VH channel provides good contrast between the target area and the ocean. Figure 6.6 shows how the result of SCM-VH with an normalized subaperture overlap $\beta = 0.73$. We now observe two peaks in the target region, and the speckle level is reduced. In the $\beta = 0.73$ case, the resolution is degraded as a consequence of narrower bandwidth and the smoothing filters; averaging and lowpass filter.

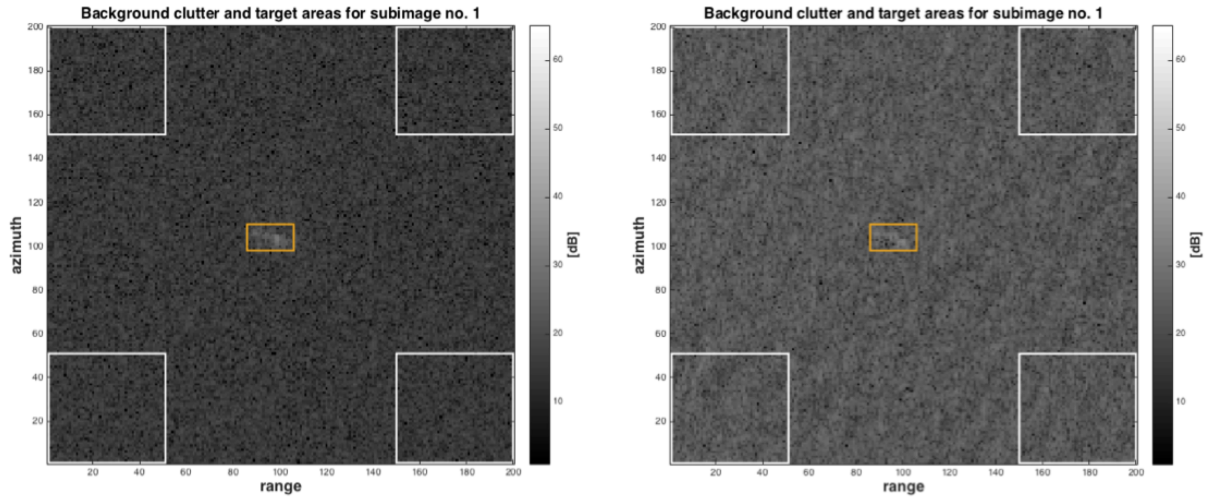


Figure 6.1: VH and VV channel of subimage no. 1:
 Resolution subimage: 4×1 km.
 Resolution target region: 200×100 m.

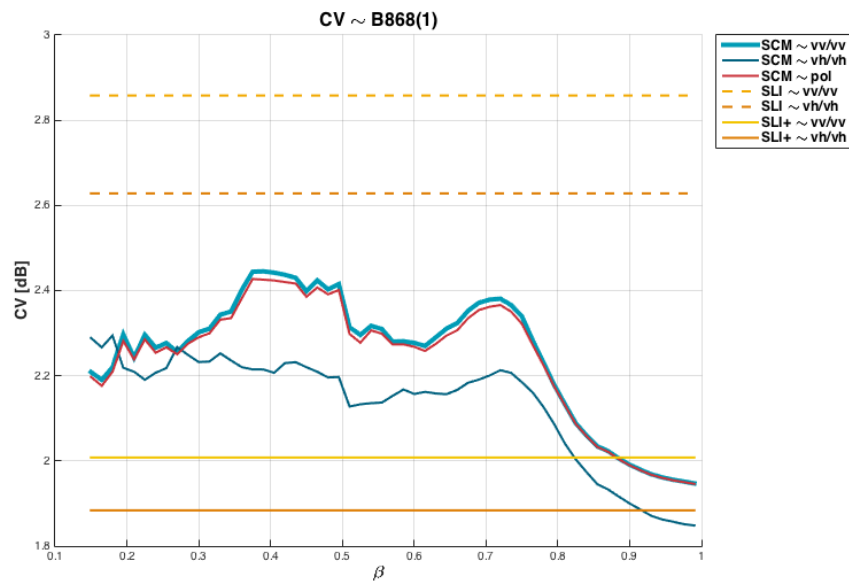


Figure 6.2: CV for subimage no. 1.

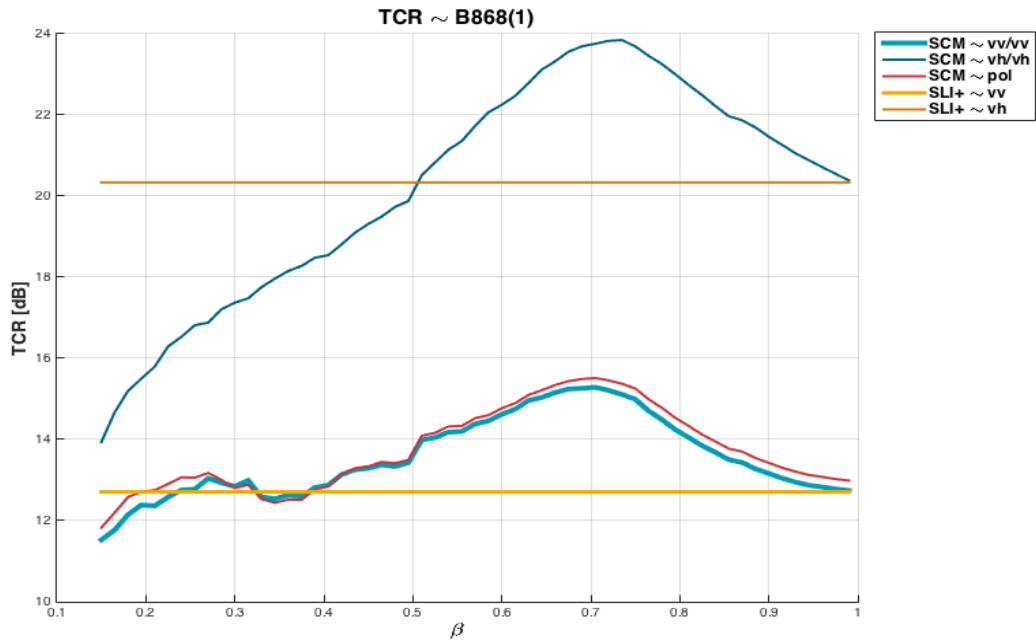


Figure 6.3: TCR for subimage no. 11. Peak observed at $\beta = 0.73$.

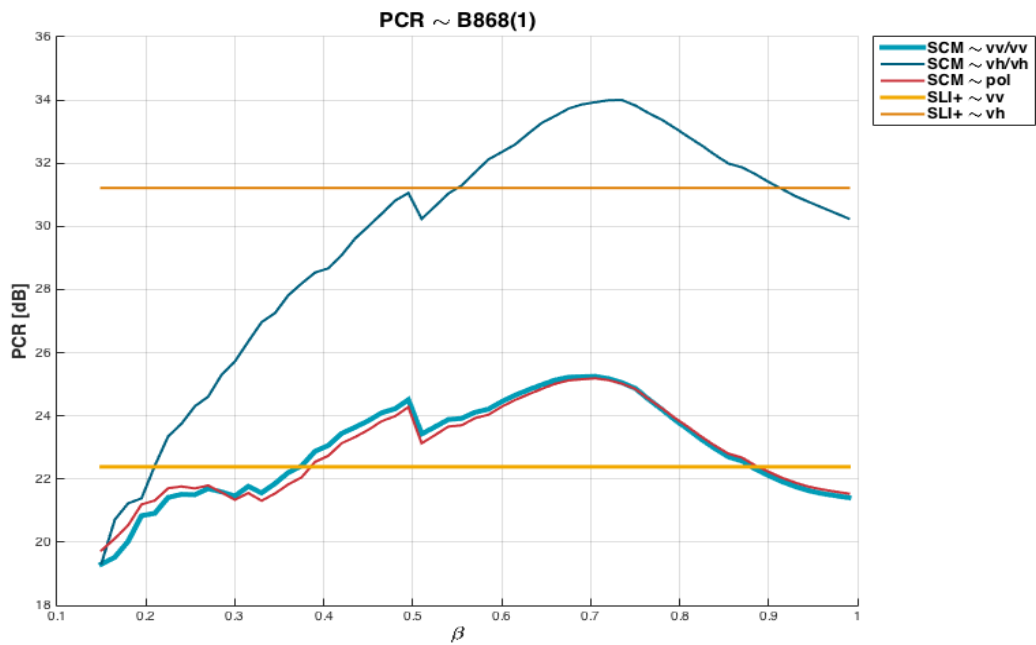


Figure 6.4: PCR for image no. 11. Peak observed at $\beta = 0.73$.

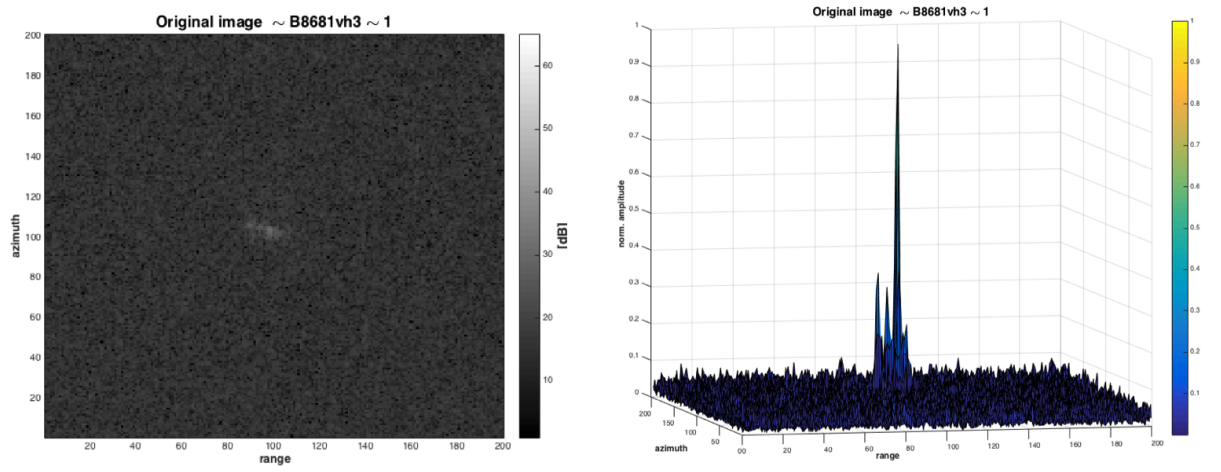


Figure 6.5: Original subimage no. 1:
 left: VH image before SCM algorithm.
 right: Normalized amplitude surface plot.

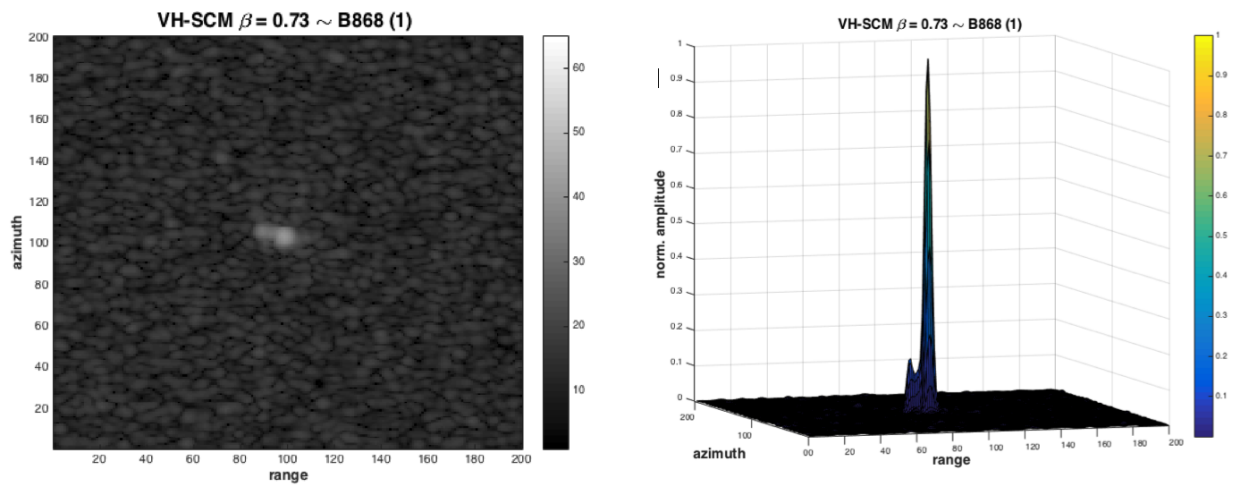


Figure 6.6: Submage no. 11:
 left: SCM-VH image with $\beta = 0.73$.
 right: Normalized amplitude surface plot, SCM-VH $\beta = 0.73$.

6.1.4 Contrast and speckle measurements for subimage no. 11

The following figures: 6.7 to 6.12 represent subimage no. 11. The original subimages displayed in figure 6.8 show that there is slightly higher contrast in the VH image compared to the VV image. In comparison with subimage no. 1, the VV image contains less ocean structures. In contrast to the CV results from section 6.1.3 we now observe that SCM-VV and SCM-VH yields lower CV values than SCM-VH. The reason for this may be that the sea is calm and that the backscatter in the VH channel is hidden below the noise floor.

The TCR and PCR are displayed in figure 6.9 and 6.10. In contrast to the previous results, referring to section 6.1.3 we now observe that all SCM algorithms behaves similarly yielding contrast at comparable levels. The SCM-VH is displayed in the middle of SCM-POL and SCM-VV regarding TCR, while SCM-VH yields the lowest PCR of all SCM algorithms.

Figure 6.11 and 6.12 show the amplitude profile of the original VH-image and the POL-SCM image at $\beta = 0.7$. The speckle level is reduced in image 6.12. Figure 6.11 shows several dominating peak amplitudes in the target region. The background region contains more noise compared to figure 6.5. This may be an effect of the signal being hidden below the noise floor. Figure 6.12 shows that the noisy background region is smoothed. Here three dominant targets are evident. It seems as though the contrast between the ocean and the center target is lowered, but this is only because the rightmost target amplitude is amplified. This illustrates that targets with low backscatter may not be visible in the VH-channel, but they stand out in the SCM-POL image.

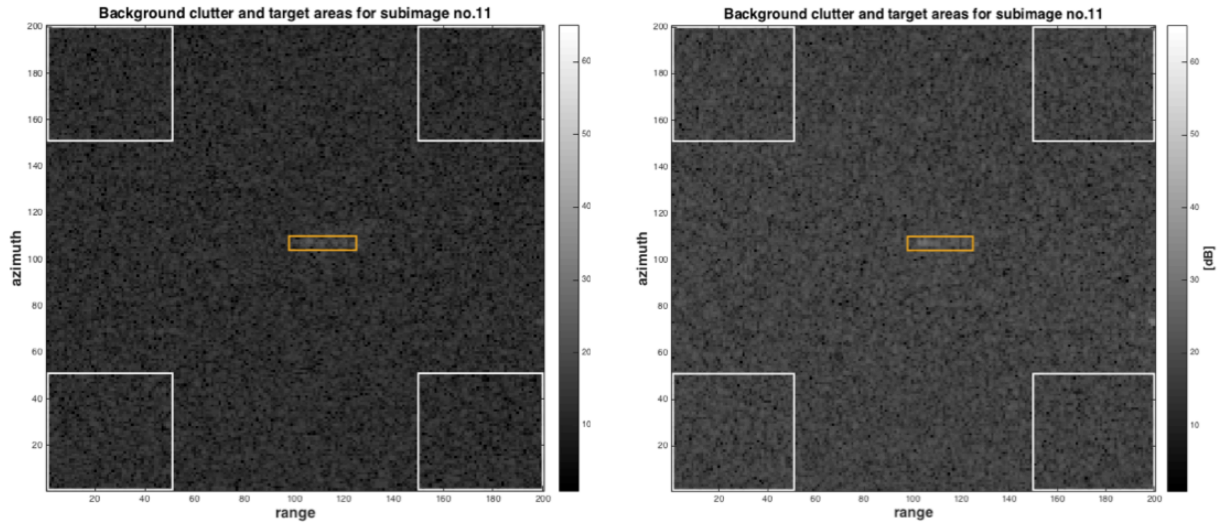


Figure 6.7: VH and VV channel of subimage no. 11:
 Resolution subimage: 4×1 km.
 Resolution target region: 129×135 m.

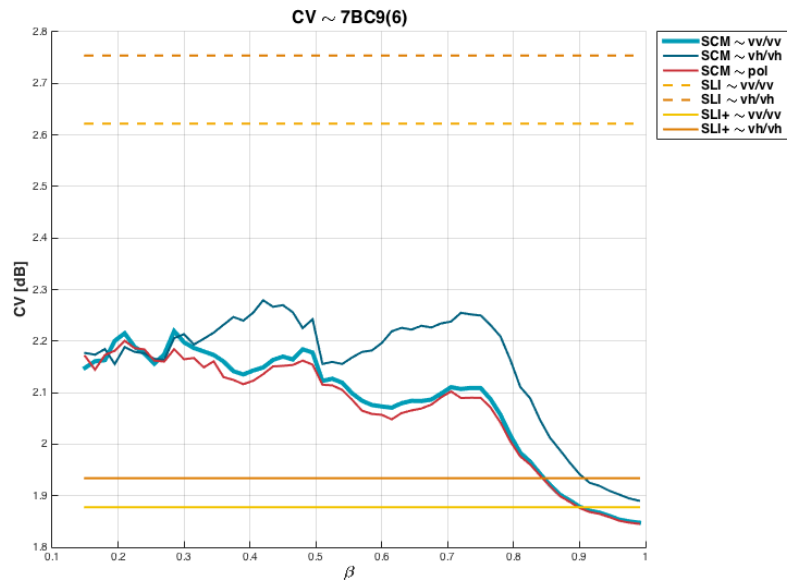


Figure 6.8: CV for subimage no. 11.

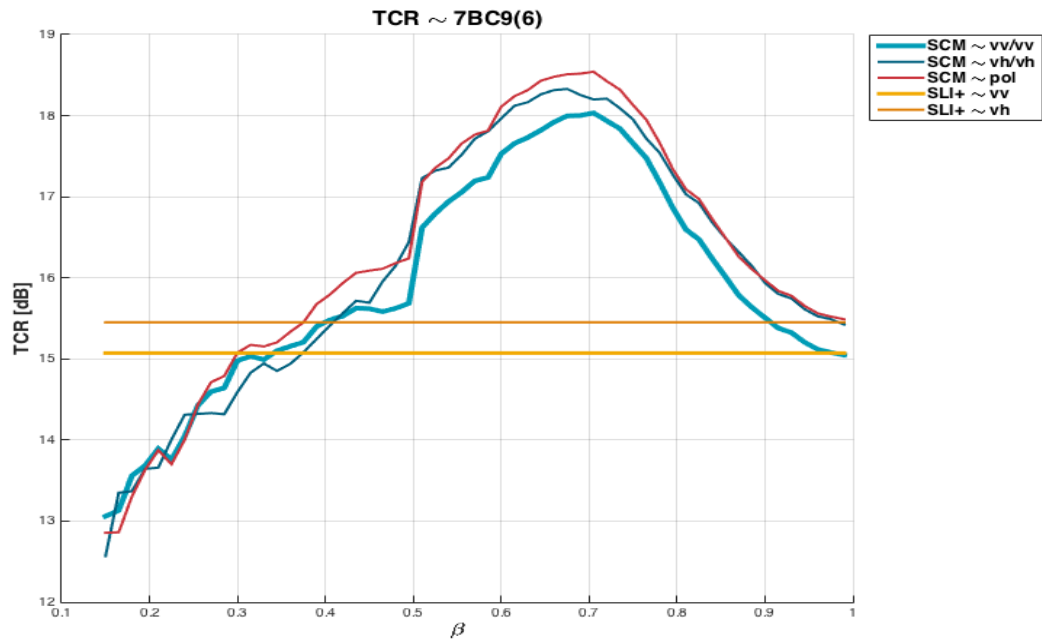


Figure 6.9: TCR for subimage no. 11. Peak observed at $\beta = 0.71$.

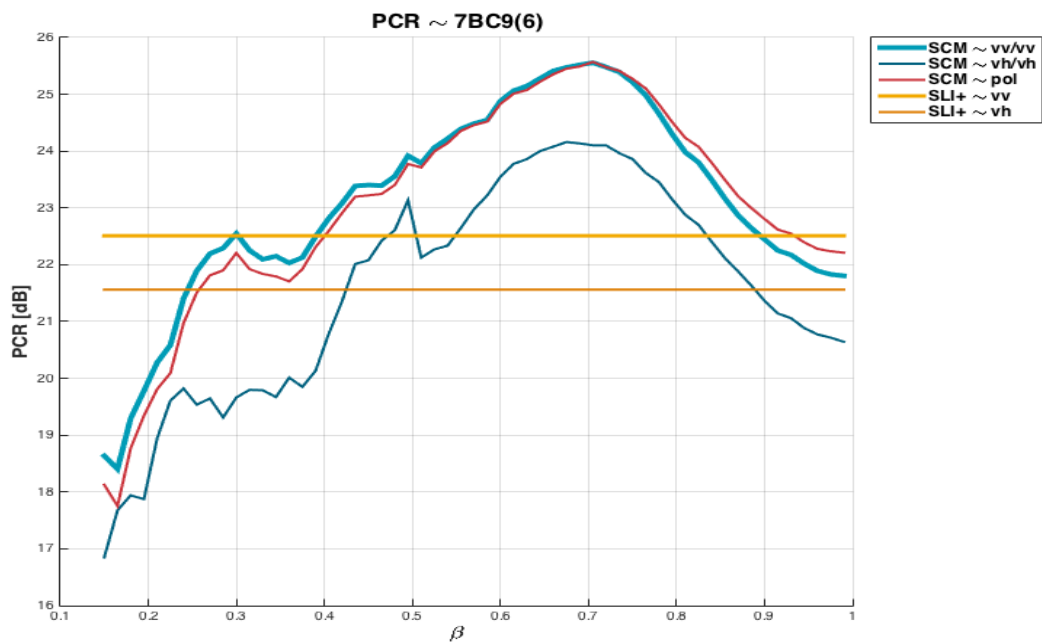


Figure 6.10: PCR for subimage no. 11. Peak observed at $\beta = 0.71$.

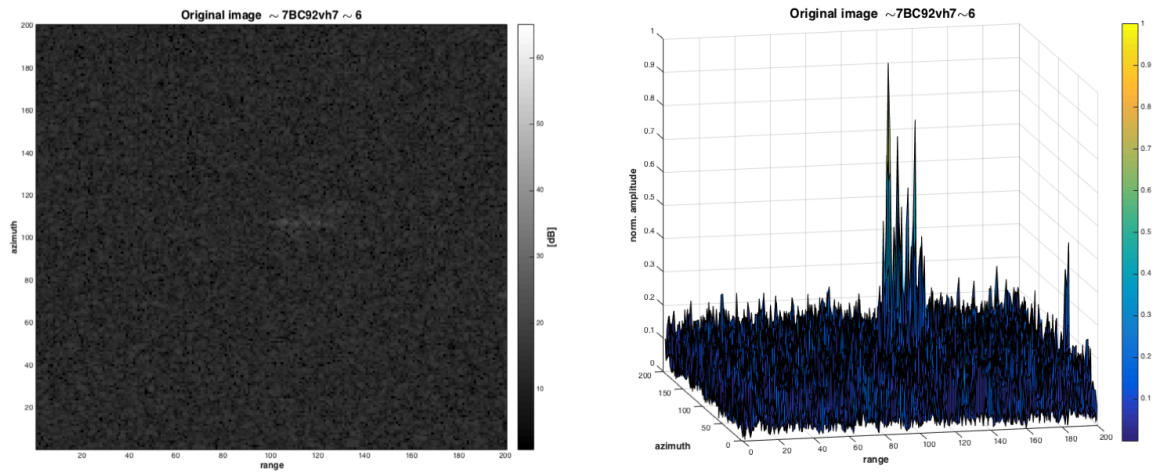


Figure 6.11: Original subimage no. 11:
 left: VH image before SCM algorithm.
 right: Normalized amplitude surface plot.

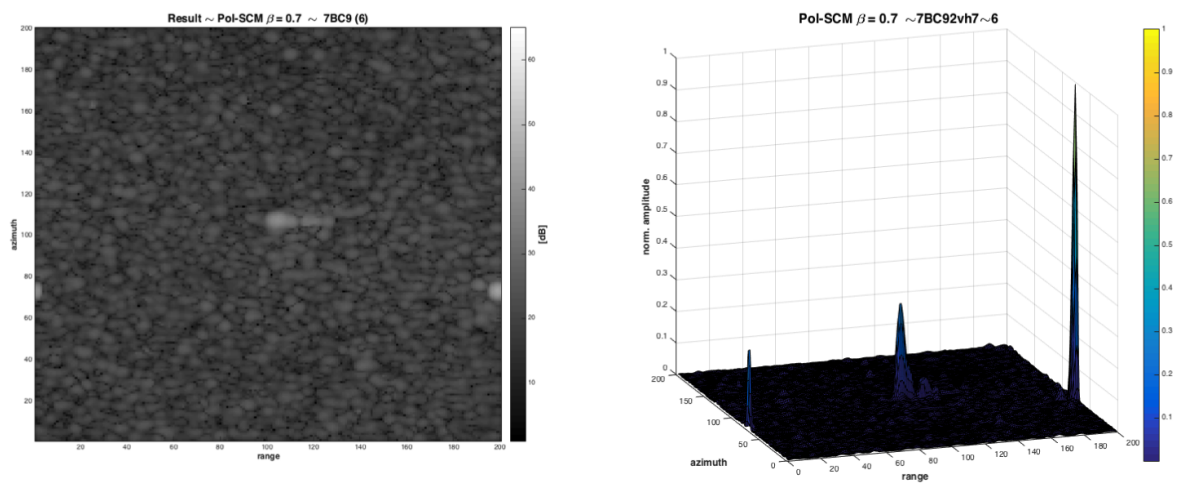


Figure 6.12: Subimage no. 11:
 left: SCM-POL image with $\beta = 0.7$.
 right: Normalized amplitude surface plot, SCM-POL $\beta = 0.7$.

6.1.5 Prewhitening of the subapertures

Souyris et al. [2] mention the need for a spectral *prewhitening* procedure to reduce side lobe effects and remove spatial correlation between neighboring pixels as a result of the antenna weighting function.

The effect of this prewhitening filter is explored by multiplying the azimuth and range spectra with the *inverse* of the antenna weighting functions. The weighting functions are specified in the metadata of each SLC image. Experience has shown that the spectrum does not get the desired flat signature by using the specified Hamming window. This may be due to the noted artifacts in the SLC spectrum from ESA IPF. Therefore, the antenna weighting function was estimated locally by using a moving average filter on the mean frequency spectrum in both azimuth and range. Figure 6.13 shows an example of how the spectrum is prewhitened.

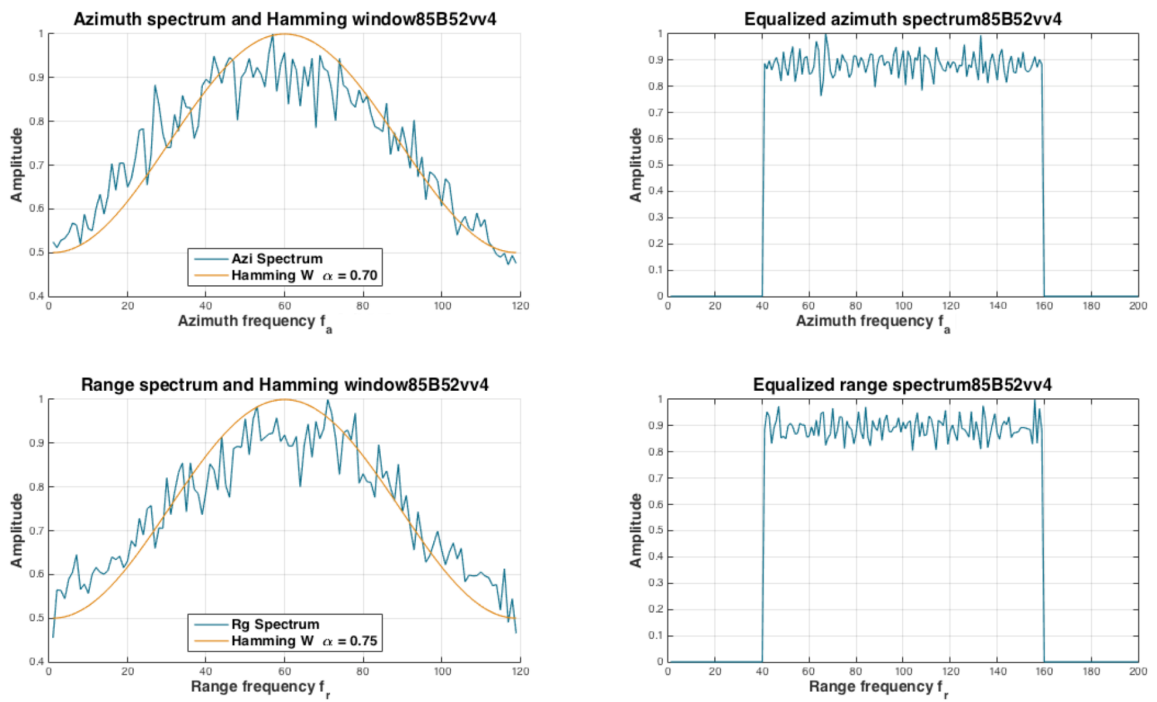


Figure 6.13: Prewhitening of azimuth spectra; Original frequency spectra to the left, and prewhitened frequency spectra to the right. The upper row show the prewhitening of the VV channel and the bottom row show the prewhitening of the VH channel.

The results of the prewhitening is presented in table 6.2. Here the column

named $\Delta TCR - PreWhite$ and $\Delta PCR - PreWhite$ represent the difference in max value of TCR and PCR. Overall there is very little difference, and in most cases the prewhitening worsens both the PCR and TCR by a small amount. In some cases, the peak TCR and PCR occur at a larger β value. Visual examination of the PCR and TCR shows that the prewhitening closely follows the trend of the nonwhitened behavior of PCR and TCR as a function of β , only lowered or raised by a small amount. This is illustrated in figure 6.14, where TCR of subimage 1 is displayed. The dotted lines represent the results when prewhitening is used. We observe that the prewhitening of the subapertures yields a approximately equal or slightly lower CV, which means that the speckle level is unchanged or lowered for all subimages.

Scene	Im	TCR [dB]	$\Delta TCR - PreWhite$ [dB]	β_{TCR}	SCM_{TCR}	PCR [dB]	$\Delta PCR - PreWhite$ [dB]	β_{PCR}	SCM_{PCR}
B868	1	23.6573	-0.3895	0.730	VH	33.4704	-0.4496	0.730	VH
B868	2	11.7025	-0.3150	0.730	VH	20.4258	-0.2139	0.490	VH
B868	3	30.2305	-0.1301	0.630	VH	45.2674	-0.2044	0.670	VH
B868	4	14.2672	-0.2886	0.710	VH	23.0566	-0.3297	0.690	VH
B868	5	23.3201	-0.0491	0.750	VH	35.4693	-0.0101	0.675	VH
7BC9	6	22.1890	-0.7041	0.660	POL	32.3305	-0.8003	0.660	POL
7BC9	7	18.3642	-0.2738	0.705	POL	25.4217	-0.3225	0.735	POL
7BC9	8	17.2604	0.1133	0.765	VH	26.1471	-0.2080	0.450	VH
7BC9	9	22.5648	0.7993	0.705	VH	37.2343	-0.3495	0.690	POL
7BC9	10	26.2836	-1.0288	0.690	VH	29.5475	-0.9633	0.690	VH
7BC9	11	19.6656	0.8275	0.705	POL	26.6950	0.8273	0.720	POL
7BC9	12	33.4685	-1.4826	0.720	VH	39.8007	-2.3639	0.405	VH
7BC9	13	25.8355	0.3923	0.720	VH	31.6084	0.4973	0.705	VH
85B5	14	12.8012	-0.8881	0.69	VH	19.3253	-0.4242	0.705	VH→VV
85B5	15	16.5355	-1.7060	0.765	POL	19.8147	-2.1311	0.765	POL
85B5	16	11.5964	-0.1920	0.750	VH	18.4286	-0.5885	0.720	VH
85B5	17	13.9839	-0.4419	0.690	VH	19.7177	-0.4372	0.390	VH
85B5	18	32.2381	-1.0343	0.675	VH	37.5979	-1.1849	0.675	VH

Table 6.2: TCR and PCR measurements for the SCM algorithms when *prewhitening* is performed. The yellow mark labels the cases where prewhitening have a positive effect on TCR and PCR as well as where there is a difference in β value.

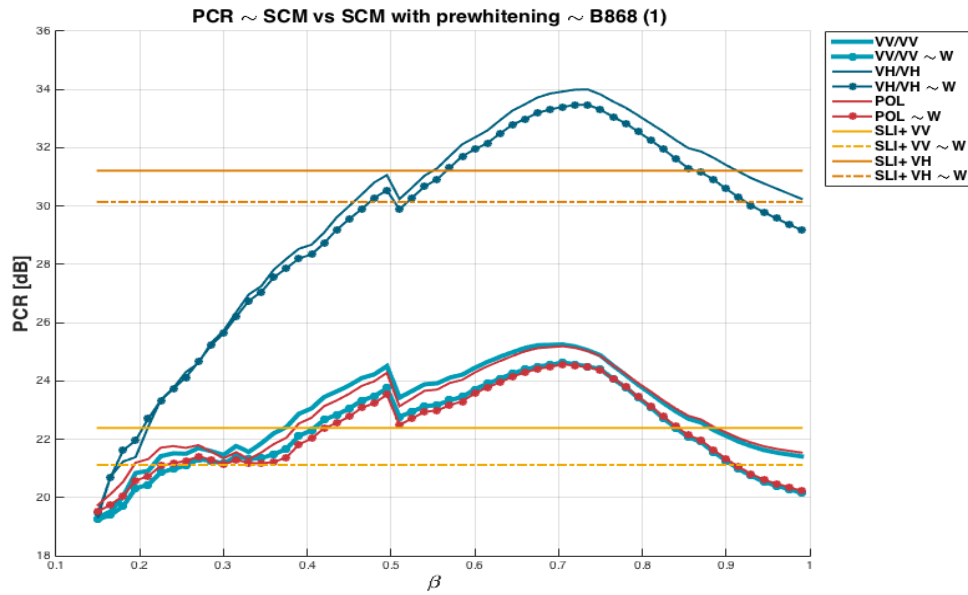


Figure 6.14: PCR with, and without prewhitening for subimage no. 1. Dotted lines represents the results when prewhitening is used

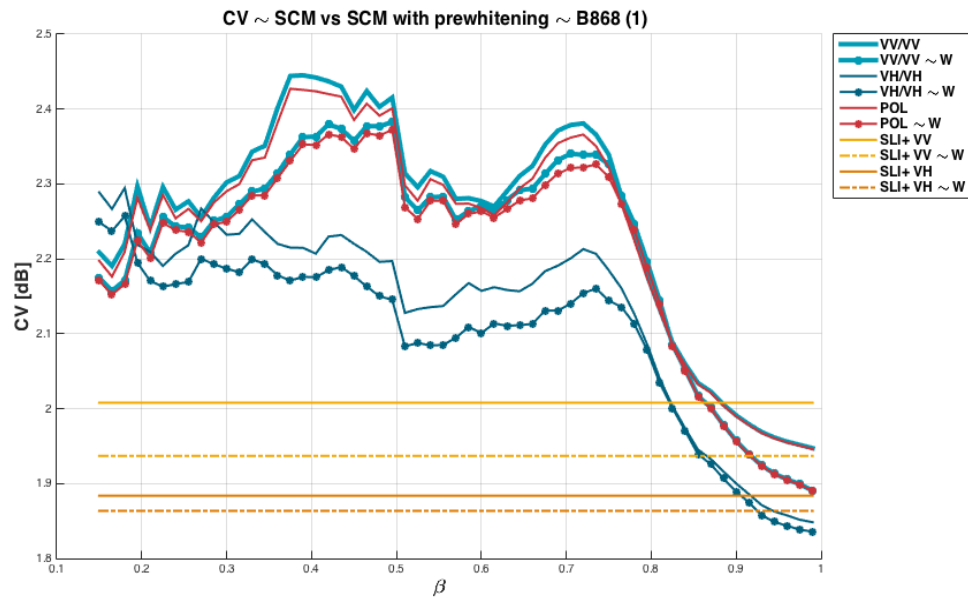


Figure 6.15: CV with, and without prewhitening for subimage no. 1. Dotted lines represents the results when prewhitening is used.

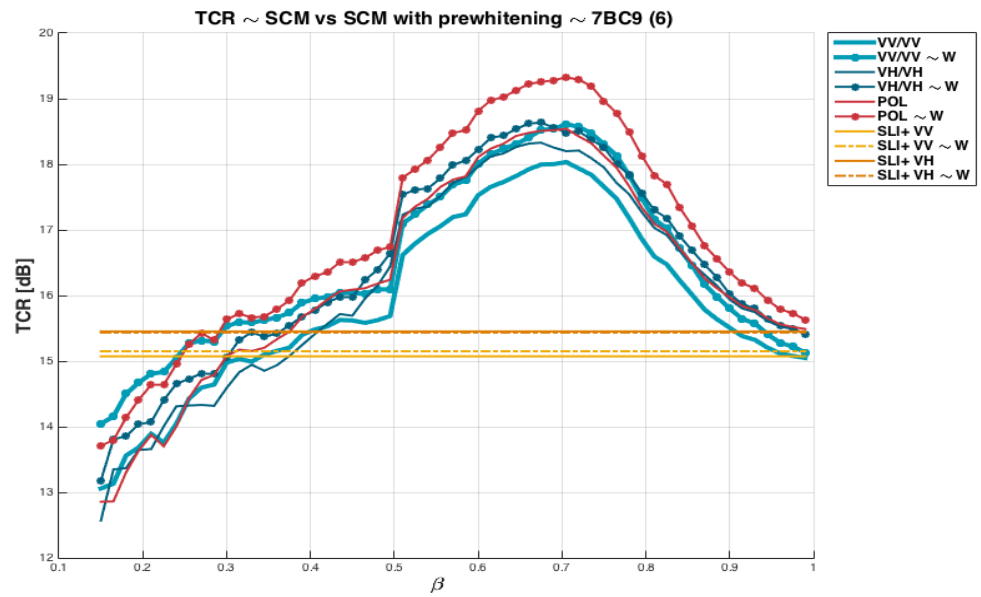


Figure 6.16: PCR with, and without prewhitening for subimage no. 11. Dotted lines represents the results when prewhitening is used.

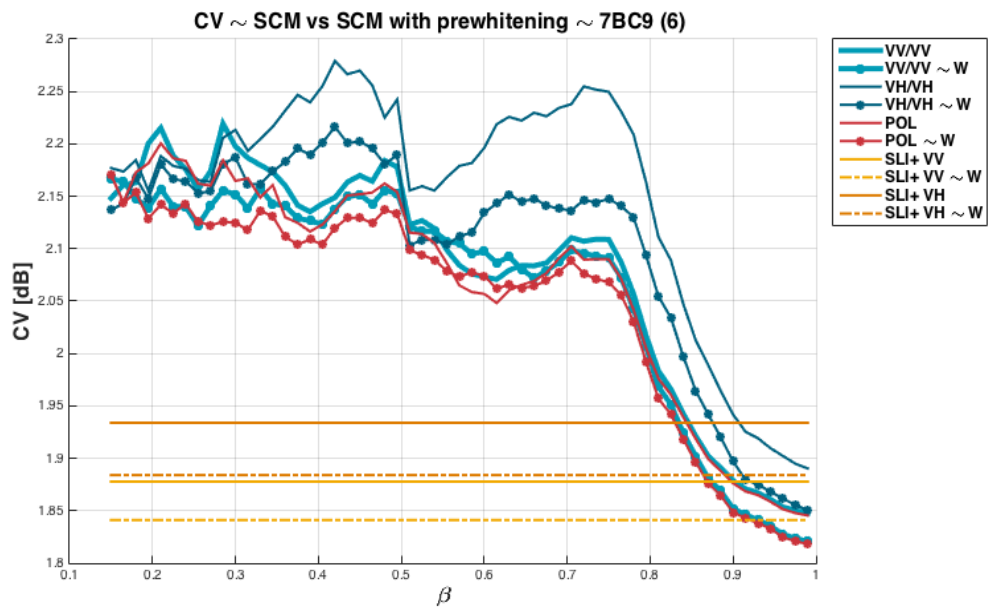


Figure 6.17: CV with, and without prewhitening for subimage no. 11. Dotted lines represents the results when prewhitening is used.

6.1.6 Dwell time and center time difference between subapertures.

Table 6.3 shows the incidence angle, dwell time and center of subaperture time difference ΔT for each subimage evaluated in the SCM analysis. According to Ouchi et al. [58] the decorrelation of speckle patterns between subapertures is independent of sea surface coherence time. The dependency only lies within the weighting function of the subapertures, the T_D and ΔT as long as the speckle is modeled as Gaussian. As ΔT decreases, the correlation between subapertures increases, and consequently we expect less speckle decorrelation. The dwell time of the data used in [58] ranged from 0 to 0.8 seconds. The TOPS IW SLC data yield significantly lower time differences between the subapertures. This is because of the short dwell time, and it makes it difficult to compare the results with those given in Ouchi et al.

Considering the Peak PCR an TCR, in most cases they occurred for $\beta \approx 0.7$. In table 6.3 we see that for $\beta \approx 0.7$, $\Delta T \approx 0.001$ s. For C-band SAR the ocean coherence time is proposed to be less than 0.05 s. However since most of the results gave highest contrast measurements when only the VH channel is used, it is difficult to draw any conclusions based on the sea state. Additional weather data and in situ measurements are needed to fully evaluate this effect. In the analysis in section 6.3, images with larger bandwidth are evaluated, and thus the dependency of sea conditions can be further investigated. If the decorrelation is dependent on the sea surface signature, and hence decorrelates at a certain ΔT , we expect to observe TCR and PCR at a higher β since the ΔT is then increased between subapertures.

We observe a steady decrease in TCR and PCR after $\beta \approx 0.7$ in all eighteen subimages. This might be the effect described in [58] where $\Delta T < 0.001$ s and the correlation between subapertures rapidly increases for $\beta > 0.7$. However, the CV also decreases in the same range as TCR and PCR, which means that both the speckle and the target response is reduced for this β value. The same behavior of CV was observed in Brekke et al.[1], They explain the decrease in CV level by considering the clutter mean μ_c and clutter standard deviation σ_c . They argue that μ_c follows the degree of correlation, and thus is expected to increase with β .

Scene	Im	θ_i	T_D [s]	β_{maxTCR}	ΔT_β [s]	β_{maxPCR}	ΔT_β [s]
B868	1	30.74°	0.0308733	0.7	0.0093	0.7	0.0093
B868	2	32.74°	0.0308734	0.5	0.0154	0.5	0.0154
B868	3	35.10°	0.0308734	0.7	0.0093	0.7	0.0093
B868	4	35.31°	0.0308734	0.7	0.0093	0.7	0.0093
B868	5	35.74°	0.0308734	0.7	0.0093	0.5	0.0154
7BC9	6	31.76°	0.0407922	0.7	0.0122	0.7	0.0122
7BC9	7	36.95°	0.0407908	0.7	0.0122	0.7	0.0122
7BC9	8	38.84°	0.0407909	0.4	0.0245	0.4	0.0245
7BC9	9	37.96°	0.0407908	0.7	0.0122	0.7	0.0122
7BC9	10	36.21°	0.0407907	0.7	0.0122	0.7	0.0122
7BC9	11	42.30°	0.0407908	0.7	0.0122	0.7	0.0122
7BC9	12	42.04°	0.0324810	0.7	0.0097	0.4	0.0195
7BC9	13	44.86°	0.0324811	0.7	0.0097	0.7	0.0097
85B5	14	36.03°	0.0407944	0.7	0.0122	0.7	0.0122
85B5	15	41.10°	0.0407947	0.8	0.0082	0.8	0.0082
85B5	16	36.04°	0.0407944	0.7	0.0122	0.7	0.0122
85B5	17	36.12°	0.0407944	0.7	0.0122	0.4	0.0245
85B5	18	36.95°	0.0407945	0.7	0.0122	0.7	0.0122

Table 6.3: Dwell time T_D , incidence angle θ_i and time difference between subapertures ΔT_β at normalized subaperture bandwidth β

6.1.7 Summary of performance analysis of subaperture processing with TOPS data from ESA IPF.

The results of sections 6.1.1-6.1.6 showed that overall, *SCM – VH* gives best contrast regarding both TCR and PCR. Referring to section 4.1 we expect *SCM – VH* to have the highest contrast since the VH image capture little ocean backscatter compared to the VV image. There were also some cases where *SCM – POL* gave better contrast than *SCM – VH*. When evaluating the cases where *SCM – POL* dominated, a possible explanation could be calm ocean conditions, and as a consequence, the backscatter in VH was hidden below the noise floor.

A prewhitening procedure of the subapertures were performed and the results showed that CV, TCR and PCR decreased in most cases. This indicates that the decorrelation is dependent on the weighting function of the subaperture, as claimed in Ouchi et al. [58].

Similar to what was found in the study of Brekke et al.[1], the CV value is reduced compared to the SLI image for all β values. The overall trend is that the CV decreases as a function of β . It is observed that when not including the low-pass filter, three peaks are still visible in the $\beta = 0.7$ image in figure 6.6. This indicates that the low-pass filter can be more fine tuned to preserve target resolution.

6.2 Experiment 2: Comparison of image products obtained from TOPS SLC data.

The second analysis is a comparison of the SCM algorithm against the PWF and the Aegir-POL algorithm. The various stages in the analysis is as follows:

- Stage 1: The Aegir-Pol is computed and evaluated by TCR PCR.
- Stage 2: The appropriate window size for PWF is evaluated against TCR and PCR.
- Stage 3: PWF is evaluated by its TCR, PCR.
- Stage 4 : Comparison of SCM, PWF and Aegir-POL images with respect to TCR and PCR.

6.2.1 Dual polarization PWF

The PWF was derived for full polarimetric SAR data, but can be adapted for use with a subset of polarimetric channels. When considering the polarizations available in Sentinel-1; VV and VH, the covariance matrix for the scattering vector is given by:

$$\underline{\underline{\Sigma}} = \begin{bmatrix} \langle S_{vv}^{(2)} \cdot S_{vv}^{(2)*} \rangle & \langle S_{vv}^{(1)} \cdot S_{vh}^{(2)*} \rangle \\ \langle S_{vh}^{(1)} \cdot S_{vv}^{(2)*} \rangle & \langle S_{vh}^{(1)} \cdot S_{vh}^{(2)*} \rangle \end{bmatrix}. \quad (6.5)$$

Novak et al. [54] estimated $\underline{\underline{\Sigma}}^{-1}$ for 64 samples. In this experiment the covariance matrix for a given target vector is estimated from a neighborhood of pixels by using a moving window. This is a computationally simple and fast method where the covariance estimator is denoted as:

$$\underline{\underline{\hat{\Sigma}}} = \frac{1}{n} \sum_{k=1}^n \mathbf{S}_{d1_k} \mathbf{S}_{d2_k}^H. \quad (6.6)$$

Here n is the number of samples. This estimator is also called the Gaussian distributed Maximum Likelihood estimator (G-ML). This estimator is computationally fast and simple, but it does not account for possible *texture* features

in the scene. It is also shown to fail in situations where we have rough ocean clutter [63].

Other *iterative* covariance estimators which includes texture assumptions and estimations of pdf parameters exists in the literature. Tao et al.[63] compares different covariance matrix estimators for sea clutter. The comparison is done with respect to computation efficiency and accuracy. They conclude that the iterative *M-estimator* is a good alternative to the G-ML estimator in situations with a lot of ocean texture.

In this experiment, only the GL-ML estimator is considered, but the number of samples in the estimation is investigated. The investigation is done by evaluating the size of a moving window, which estimates the covariance locally. The window has dimension [window size \times window size] = n . Different window sizes was investigated with respect to TCR and PCR in order to obtain the highest possible ship to ocean contrast.

Figure 6.19 show the TCR as a function of window size for all subimages. Here we see that the TCR and PCR increases with higher window size. When the window size increases, more samples are included in estimating the local covariance matrix. Increase of window size also means that the clutter samples are included in several estimation windows, and that fewer estimates are based on clutter, alone. We observe that there is little variation in TCR and PCR for window size above 25. In the following analysis the PWF is thus performed by measuring the $\underline{\underline{\Sigma}}$ from $27 \times 27 = 729$ subsamples.

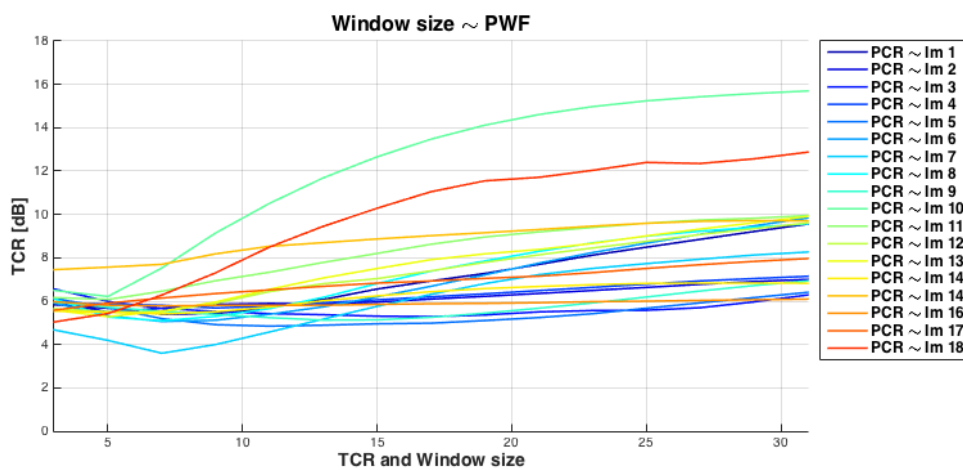


Figure 6.18: Window size as a function of TCR.

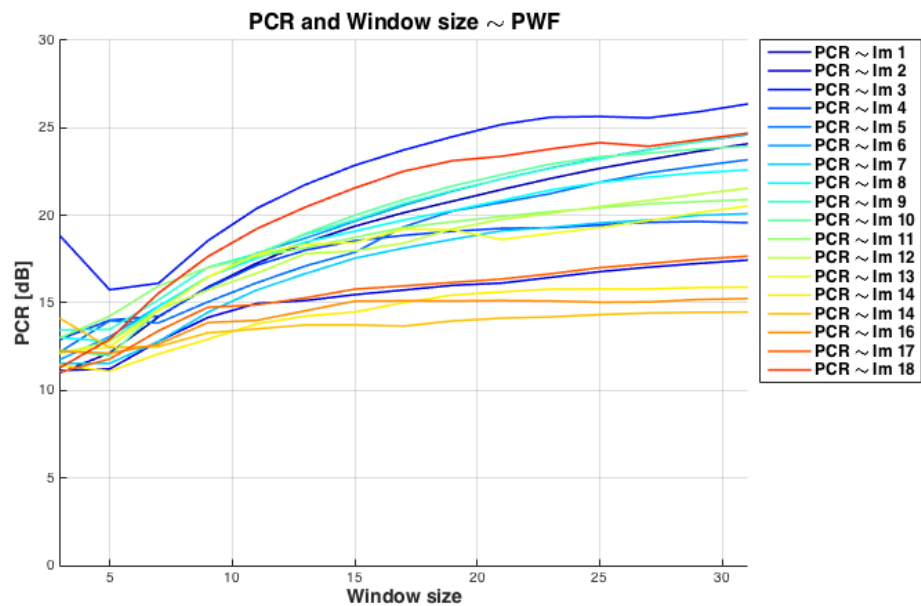


Figure 6.19: Window size as a function of PCR.

Table 6.4 show the highest TCR and PCR measured from the SCM image, the PWF image and Aegir-Pol image. The yellow color mark in the table highlights the highest contrast measure. Comparing the different algorithms, one sees that when it comes to TCR, the SCM algorithm yields the highest contrast regarding all eighteen subimages. Considering the PCR, we observe that Aegir-Pol gave higher contrast than the SCM for some sub-images.

Figure 6.20 shows the output image after Aegir-Pol (right) and PWF (left) is processed on subimage 1. We observe that the target response has increased in the Aegir-Pol image compared to the original VH-image shown in figure 6.21. In both the PWF- and Aegir-Pol image we observe visible ocean structure. In the PWF image it we observe that the ocean clutter is smoothed around the target within a area comparable to the estimation window. This is observed for all eighteen subimages. This means that including clutter in the estimation window have a positive effect on local TCR and PCR.

The resolution differs between the Aegir-POL, PWF and the SCM image. Regarding both Aegir-Pol and PWF, the resolution is unchanged compared to the original image. In contrast the resolution in the SCM image is degraded as consequence of decreased bandwidth and filtering.

Figure 6.24 shows the surface plot of the Aegir-POL image (right) and PWF

Scene	Im	TCR- SCM [dB]	TCR- PWF [dB]	TCR- Aegir-Pol [dB]	PCR-SCM [dB]	PCR-PWF [dB]	PCR- Aegir-Pol [dB]
B868	1	24.0468	8.8517	15.6238	33.9200	23.1836	28.9387
B868	2	12.0175	6.7758	9.0908	20.6397	17.0419	20.0079
B868	3	30.3606	5.6977	21.0110	45.4718	25.5731	43.0462
B868	4	14.5558	6.9317	11.3182	23.3863	19.6050	23.5906
B868	5	23.3692	5.9202	19.8083	35.4794	22.4331	39.4607
7BC9	6	22.8931	9.0853	17.0544	33.1308	23.7594	30.6249
7BC9	7	18.6380	7.9346	13.8544	25.7442	19.7374	26.5793
7BC9	8	17.1471	9.2288	14.3701	26.3551	22.1902	28.5596
7BC9	9	21.7655	6.4679	19.5661	37.5838	23.7375	38.9120
7BC9	10	27.3124	15.4295	22.3503	30.5108	23.5499	31.6617
7BC9	11	18.8381	9.7413	15.4145	25.8677	20.6622	26.4115
7BC9	12	34.9511	9.0739	29.3080	42.1646	20.8590	40.0593
7BC9	13	25.4432	9.3278	20.2603	31.1111	19.7039	30.1060
85B5	14	13.6893	6.8312	10.9582	19.7495	15.7984	20.2038
85B5	15	18.2415	9.6860	16.2734	21.9458	14.4239	22.1830
85B5	16	11.7884	6.0339	9.3326	19.0171	15.0587	19.0357
85B5	17	14.4258	7.6813	10.2450	20.1549	17.2466	19.6653
85B5	18	33.2724	12.3510	26.7042	38.7828	23.9483	37.3599

Table 6.4: TCR and PCR measurements for SCM, PWF, and Aegir-Pol

image (left) computed for subimage 11. Compared to the original VH image, we observe that the speckle level is reduced in both images. In the Aegir-POL image we see that the peak of the center target is amplified, in contrast to the PWF image where the opposite has occurred. Recalling that three possible targets were visible in the SCM-POL image, only two targets is present in both the Aegir-POL image and PWF image. Based on these results the SCM-VH image and SCM-POL image seems to represent the best candidates for ship detection products when TOPS SLC data are used.

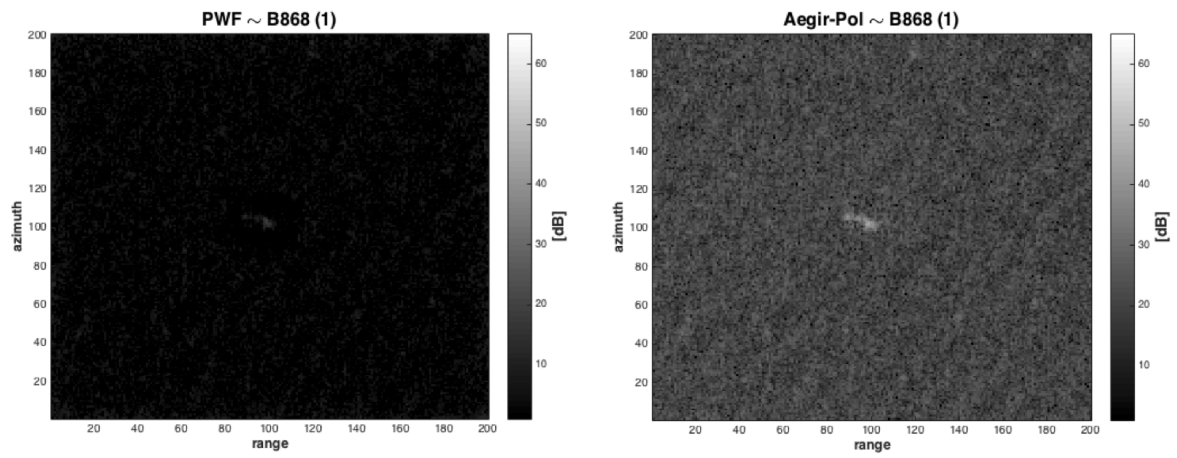


Figure 6.20: Polarimetric Whitening Filter (left) and Aegir-Pol (right), subimage no. 1.

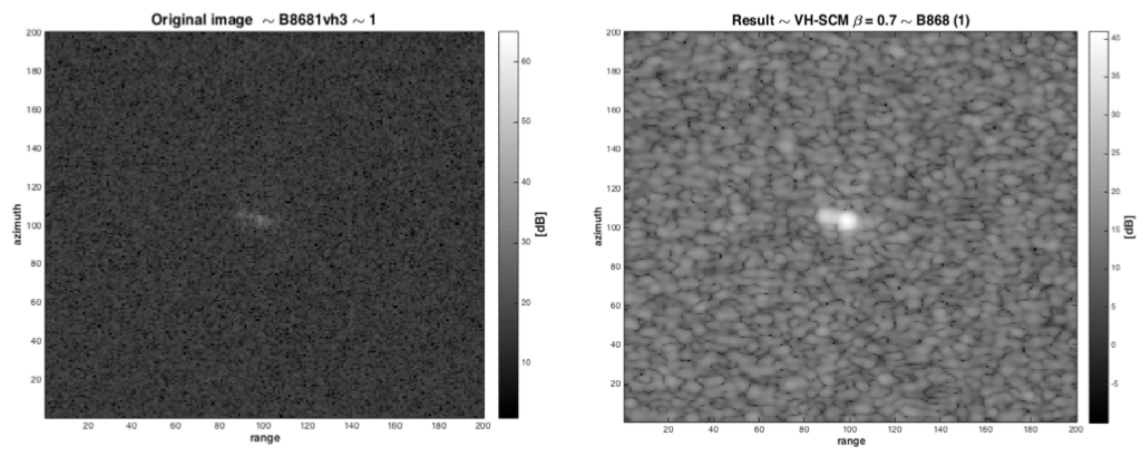


Figure 6.21: Original amplitude image of VH (left) SCM-VH for $\beta = 0.7$ (right), on subimage no. 1

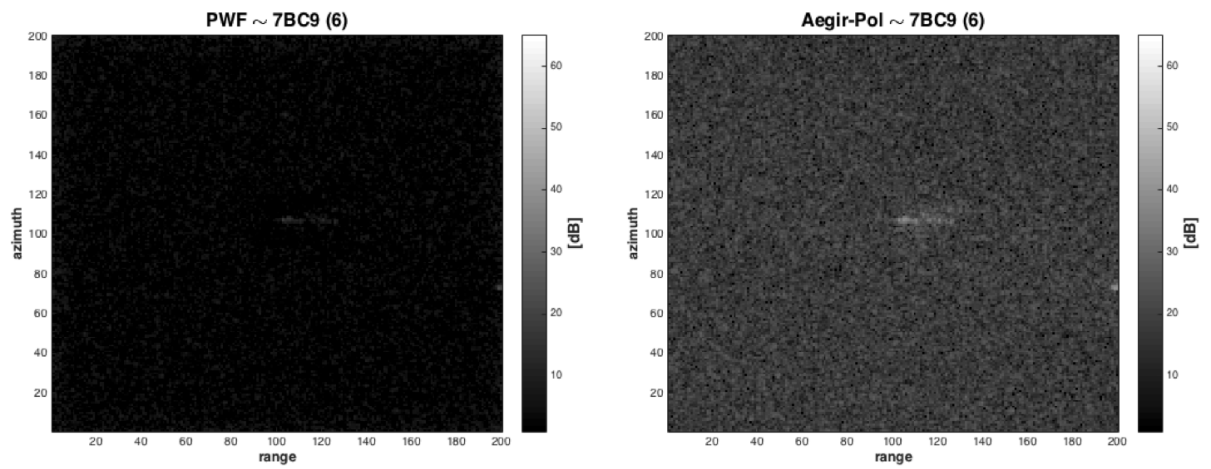


Figure 6.22: Polarimetric Whitening Filter (left) and Aegir-Pol (right) on subimage no. 11.

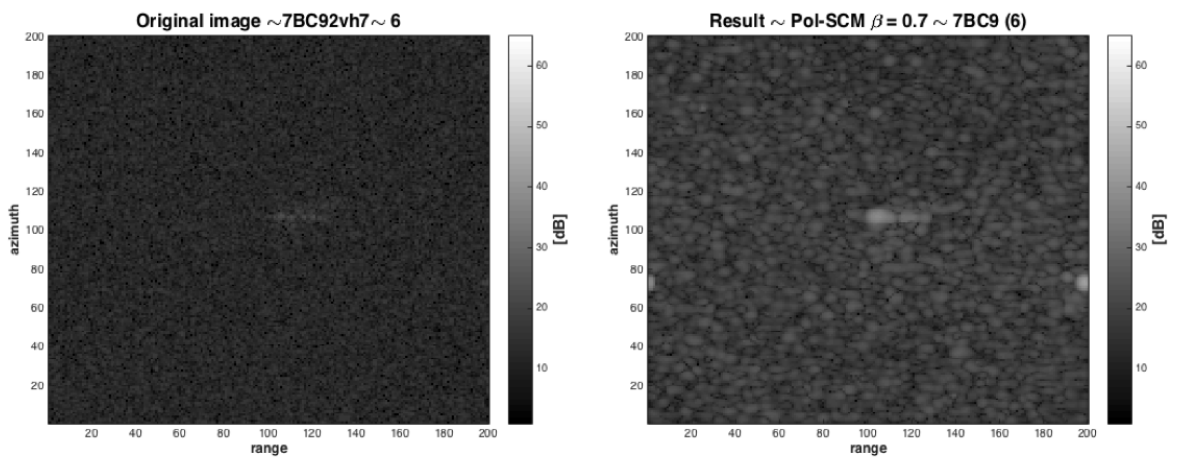


Figure 6.23: Original amplitude image of VH (left) SCM-VH for $\beta = 0.7$ (right), subimage no. 11.

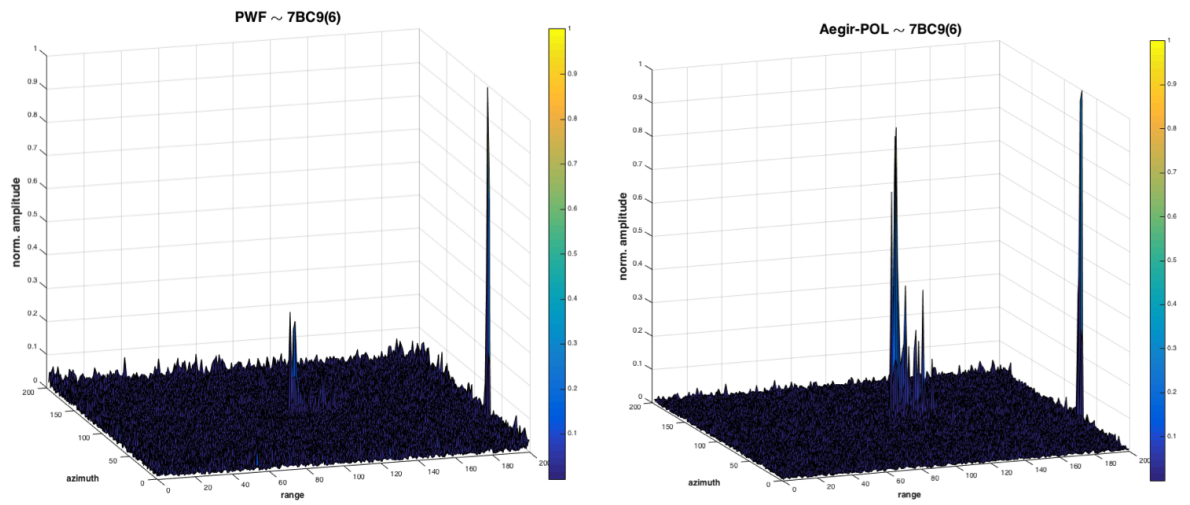


Figure 6.24: Surface plot of Polarimetric whitening filter (left) and Aegir-POL image (right), representing subimage no. 11.

6.3 Experiment 3: Performance analysis of subaperture processing with TOPS data, focused by NRTSAR.

This analysis considers the second main goal of the thesis: How will the processing of TOPS data with a different focusing scheme affect the ship detection product? The raw data of the scene corresponding to three subimages is focused by NRTSAR with varying processing bandwidths and Hamming window coefficients. Hereafter Hamming window coefficient is denoted as HWC. The NRTSAR prototype gives output with narrower azimuth dimension than ESA IPF. When varying the bandwidth, this means that some information is cut off in either azimuth direction. This problem, limits the choice of subimages to be processed, and thus subimage no. 1, 13 and 18 are chosen.

Figure 6.26 shows the three different Hamming windows used in the focusing. Window coefficients of 0.75, 0.65 and 0.5 is explored. The focusing is done with three different bandwidths shown in table 6.5. Since the focusing bandwidth is different for each subswath, the three bandwidth options is chosen such that the interval between ESA IPF and NRTSAR is approximately the same. Bandwidth option 1 represents the full bandwidth available in NRTSAR processor. Option 2 represents a bandwidth in between the available bandwidth and the bandwidth used in ESA IPF. Bandwidth option 3 is the bandwidth used by ESA IPF. The outline of the processing options for each scene is shown in figure 6.25. Here we can see that nine new images from each subimage is produced.

Swath	Azimuth Bandwidth [Hz]		
	1	2	3
IW1	373	350	327
IW2	373	340	313
IW3	373	340	314

Table 6.5: Bandwidths used in azimuth focusing with NRTSAR

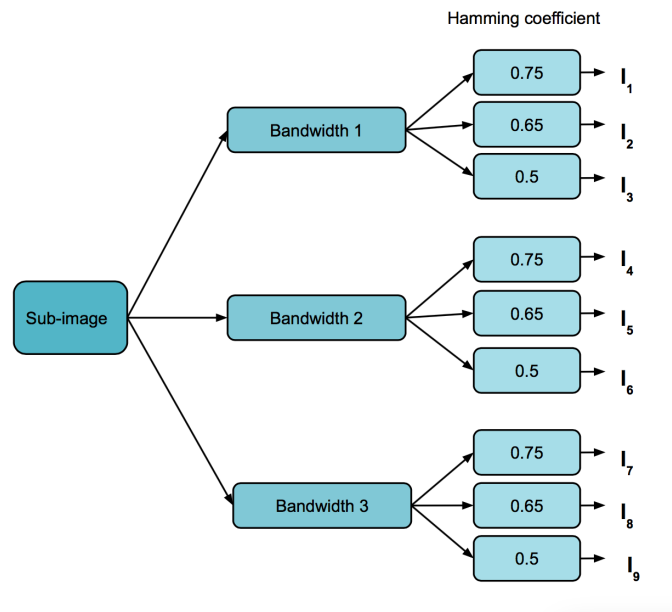


Figure 6.25: Outline of bandwidth and Hamming window coefficient options chosen for focusing with NRTSAR

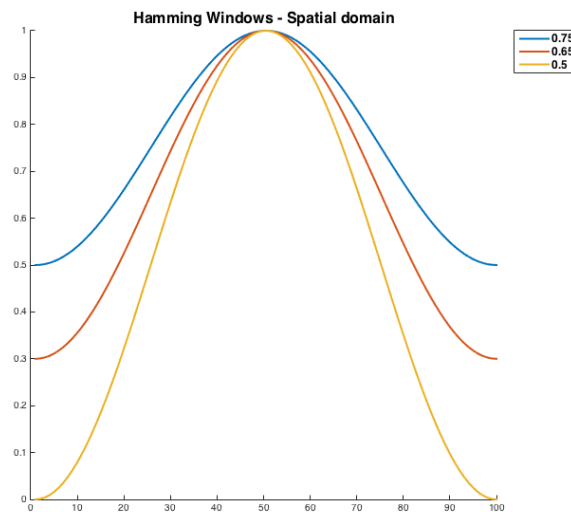


Figure 6.26: Hamming windows with different coefficients;
 yellow ~ 0.5 ,
 red ~ 0.65 ,
 blue ~ 0.75

As mentioned in section 3.4.1 the SLC data focused with ESA IPF, have undergone additional pattern corrections applied to the frequency spectra. This is not accounted for in the NRTSAR processing and therefore a direct comparison of the performances is not valid.

Figure 6.27 and 6.28 shows two examples of SLC data focused with ESA IPF and SLC data focused with NRTSAR with equal processing parameters. The difference in CV is depicted in figure 6.27. Considering the SCM-VH, we observe that the CV measurement is slightly lower regarding the SCM image focused by NRTSAR compared to the SCM image focused with ESA IPF.

Figure 6.28 show the variation of PCR measurements for NRTSAR and ESA IPF. The *SLI - VH* image from NRTSAR gave higher PCR than the *SLI - VH* image from ESA IPF. In contrast, we observe no variation considering the *SLI - VV* images. Overall we observe a decrease in both PCR and TCR for all SCM images processed with NRTSAR compared to the SCM images processed with ESA IPF. This may be the effect of the various corrections applied in ESA IPF.

In the next section, only NRTSAR SLC products are evaluated in terms of varying bandwidth and HWC. This is because it gives a better basis for comparison.

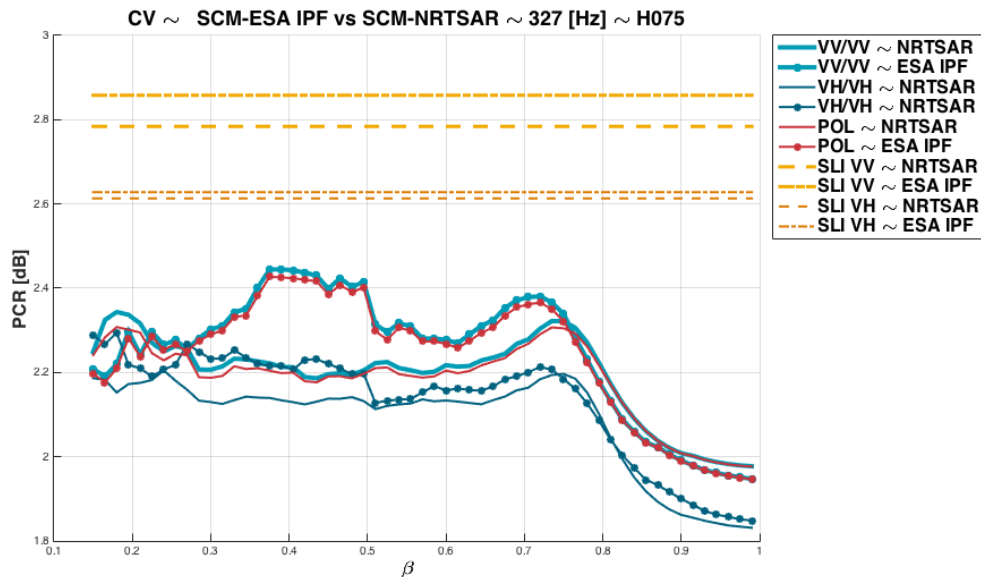


Figure 6.27: SCM computed for subimage no. 1 showing the CV result from ESA IPF in the dotted lines, and NRTSAR in the smooth lines.

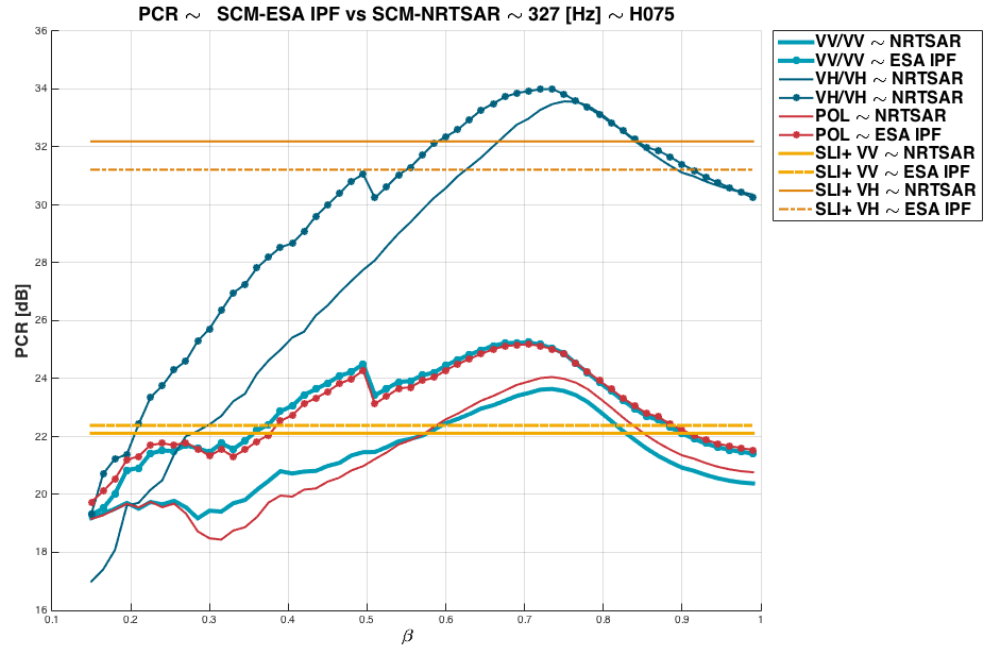


Figure 6.28: SCM computed for subimage no. 1 showing the PCR result from ESA IPF in the dotted lines, and NRTSAR in the smooth lines.

6.3.1 Comparison of subaperture image products focused by NRTSAR with varying processing bandwidth and Hamming window coefficients.

This section presents the impact on the SCM algorithm by varying the processing bandwidth and HWC. Recalling from section 3.3.2 and 4.6.1 HWC 0.5 yield the lowest PSLR and ISLR but will give an image with degraded resolution because of the widened IRW. HWC 0.75 gives the best resolution but at the expense of higher PSLR and ISLR. In the following only the main characteristics are presented, with relevant excerpts from all the results. Tables with detailed information from this analysis can be found in the Appendix section 8.3. The evaluation will first consider the CV measurement from the SCM images, and then evaluate TCR and PCR, respectively.

Considering the CV measurements we observe that all subimages yield similar measurements regarding both bandwidth and HWC. However there is a small difference between the various SCM-images. The trend is clear when it comes to the SCM-VH image. We only consider, CV values for $\beta > 0.6$ as this is where the highest contrast measurements is observed. Full processing bandwidth of

373 Hz and HWC 0.75 yields the lowest CV for the SCM-VH image. Regarding the SCM-VV image and SCM-POL image the CV yielded various results. We observe that the lowest CV values occurs for both 340- and 350 Hz and 313- and 327 Hz regarding SCM-VV and SCM-POL. This is in contrast to the SCM-VH image where we observed the lowest CV value at 373 Hz.

Figure 6.29 shows an example of the difference between the SCM-VH and SCM-VV/POL in terms of CV. Here the SCM algorithm is computed for fixed HWC 0.75 and varying focusing bandwidth for subimage no. 18. Only considering $\beta > 0.6$ we see that 314 Hz gives lowest CV value for SCM-VV and SCM-POL, while 373 Hz yields lowest CV for SCM-VH.

It is worth noticing that the differences between the bandwidths and HWC are minimal in all cases, which means less than 0.1 dB. This will most likely not influence the result of ship detection.

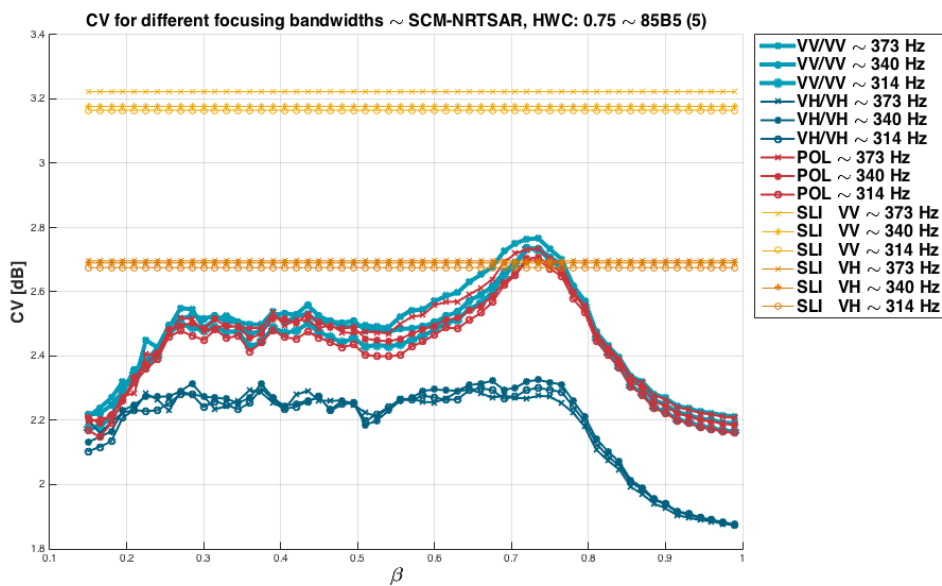


Figure 6.29: SCM computed for subimage no. 18 representing the CV results from NRTSAR with varying processing bandwidth and fixed Hamming window coefficient 0.75.

The results showed that considering all SCM images a processing bandwidth of 340 – 50 Hz and 373 Hz, gave highest PCR and TCR regardless of HWC. However it is observed for subimage no. 13 that the variation of PCR and TCR is higher as a function of HWCs when a processing bandwidth of 313 Hz is used. The variation is illustrated in figure 6.30. Here we see that a HWC of 0.5

yields lowest PCR for SCM-VH, SLI-VH, SCM-VV and SLI-VV. This is as expected since a lower bandwidth plus HWC 0.5 gives the worst possible resolution in this context, and therefore the peak value will be less defined.

Figure 6.31 show the PCR results from subimage no. 13 with processing bandwidth of 340 Hz. In contrast to figure 6.30 we now see little variation in PCR as a function of HWC. These results may indicate that in some cases, raising the processing bandwidth makes the choice of HWC become more arbitrary. We also observe that the maximum value of PCR and TCR occurs at slightly lower β value when processing with 313 – 327 Hz compared to 340 – 373 Hz. Measuring the PCR and TCR may not be the optimal way to evaluate the effect of different HWC, their influence will most likely be seen when considering the area in the neighborhood of the target. Here the degree of sidelobes will vary.

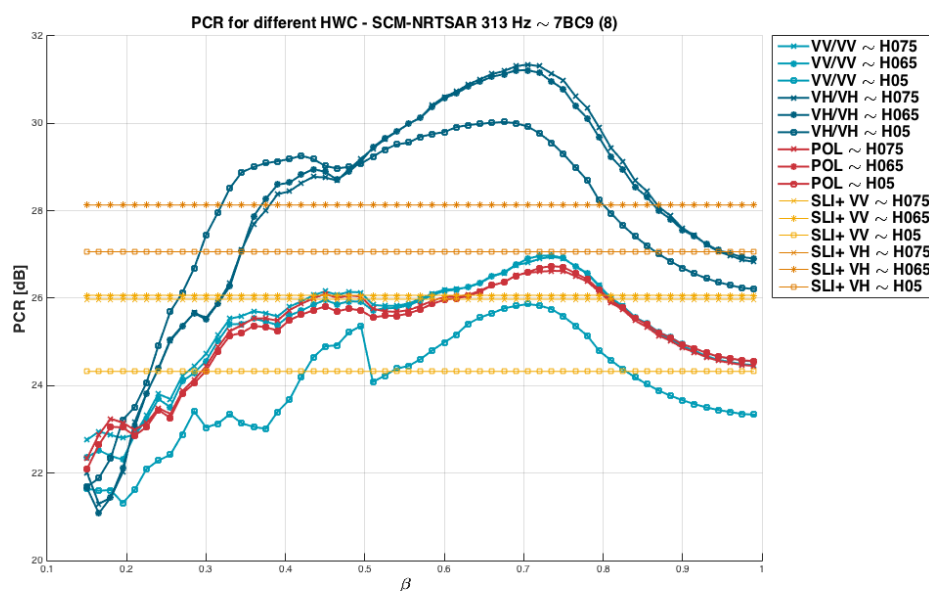


Figure 6.30: PCR results for SCM images obtained from subimage no. 13 focused by NRTSAR with processing bandwidth 313 Hz and varying Hamming window coefficients.

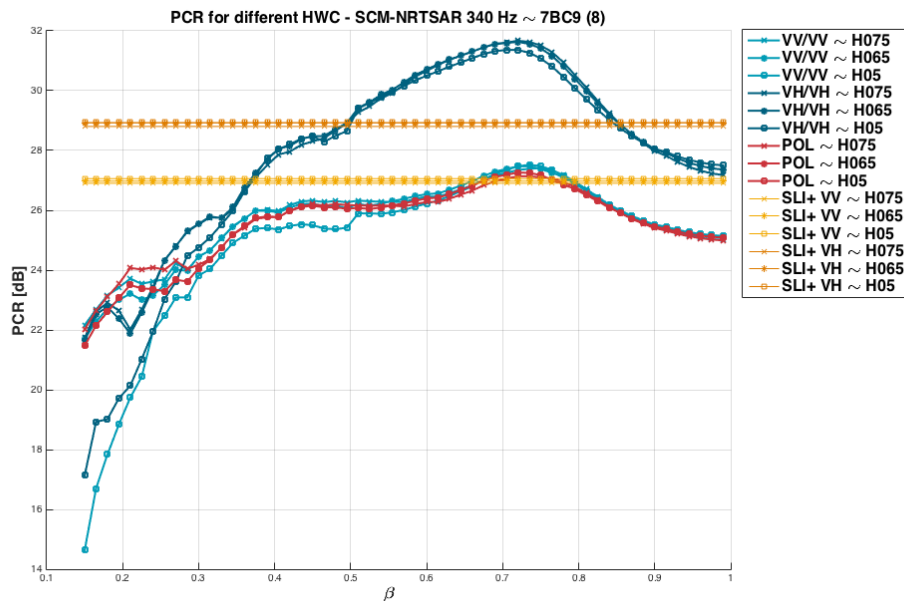


Figure 6.31: PCR results for SCM images obtained from subimage no. 13 focused by NRTSAR with processing bandwidth 340 Hz and varying Hamming window coefficients

Increasing the focusing bandwidth yielded higher TCR and PCR for all SCM images. When increasing the focusing bandwidth, the ΔT is also increased between the subapertures. The largest range between the focusing bandwidths were 313 – 373 Hz. Subimage no. 13 was focused with this range of bandwidths and the consequently range in ΔT at $\beta = 0.7$ is then [0.00972 – 0.01158]s which is an increase of 0.00186 seconds. Comparing the β values at the peak TCR and PCR with focusing bandwidth 373 and 313, we observe a minor decrease in β value, which means that ΔT is even higher at this point of the peak TCR and PCR. This implies that the optimal TCR and PCR is not dependent on a certain ΔT value and that other factors may be the cause. However this must be further investigated by processing more subimages with supporting weather data.

6.4 Experiment 4: Comparison of image products obtained from TOPS SLC data focused by NRTSAR, with varying Hamming window coefficients and focusing bandwidths

This analysis evaluates the TCR and PCR from PWF images and Aegir-Pol images when focusing TOPS SLC data with varying HWC and bandwidths. The evaluation will start with the result obtained from the Aegir-Pol images considering each subimage separately. Then the evaluation continues with the results obtained from the PWF images.

The maximum values of TCR and PCR from the Aegir-Pol images is recorded in table 6.6. The results from image no 1 show that both PCR and TCR increased with lowering HWC, when each bandwidth is considered separately. When only considering the limiting bandwidth of 327 Hz and the full bandwidth 373 Hz, we observe that a minimal increase in both TCR and PCR when using a processing bandwidth of 327 Hz. The maximum TCR is observed at 327 Hz with HWC 0.5, while the maximum PCR is observed at 350 Hz and HWC 0.5.

Overall, Image no. 13 also reports a minimal increase in both TCR and PCR when using a processing bandwidth of 314 Hz, regardless of HWC. One exception is observed for HWC 0.75. Here the PCR experience a small decrease when lowering the processing bandwidth. Referring to table 6.6 we see that the maximum TCR and PCR occurs for 314 Hz, and HWC 0.5.

Regarding image no. 13, and considering bandwidth 373 and 313 Hz, we observe a minor decrease in TCR and PCR for 313 Hz. There is one exception for the TCR with HWC 0.5, here we observe a minor increase. Overall, both TCR and PCR increases with decreasing HWC. The maximum values of TCR and PCR occurs for full bandwidth 373 and at HWC 0.5 and 0.75, respectively.

The maximum values of TCR and PCR from the PWF image are recorded in table 6.7. Regarding image no. 1, the highest PCR were observed for focusing bandwidth 373 Hz, with HWC 0.75. The highest TCR were observed with focusing bandwidth 350 Hz, and HWC 0.65. When evaluating each bandwidth separately, we observe that TCR have a minor increase with waning HWC. The opposite is observed for PCR, here the results show a minor decrease with waning HWC.

Considering subimage no. 13, and comparing with subimage 1 the opposite trend of TCR and PCR is observed. The TCR decreases with decreasing HWC, while the PCR increase with waning HWC. This is observed for all three

bandwidths. Table 6.7 show that the highest PCR were observed for focusing bandwidth 314 Hz, with HWC 0.75. The highest TCR were observed for 373 Hz and HWC 0.75.

Regarding subimage no. 18, no apparent trend is observed. The highest PCR and TCR were observed for focusing bandwidth 313 Hz with HWC 0.5 and HWC 0.65, respectively.

Aegir-Pol				
Im	TCR _{MAX}		PCR _{MAX}	
	Bandwidth [Hz]	HWC	Bandwidth [Hz]	HWC
1	327	0.5	350	0.5
13	313	0.5	313	0.5
18	373	0.5	373	0.75

Table 6.6: Maximum values of TCR and PCR when using the Aegir-POL algorithm, representing the three selected subimages. HWC represents the Hamming window coefficient

PWF				
Im	TCR _{MAX}		PCR _{MAX}	
	Bandwidth [Hz]	HWC	Bandwidth [Hz]	HWC
1	350	0.65	373	0.75
13	375	0.75	313	0.75
18	314	0.65	314	0.5

Table 6.7: Maximum values of TCR and PCR when using the PWF algorithm, representing three selected sub-images. HWC represents the Hamming window coefficient

Only three subimages were considered in this analysis, and therefore no strict conclusions can be made. Regarding the TCR and PCR results for the PWF and Aegir-POL images no particular trend was observed for all three images. It is worth noticing that the overall effect on TCR and PCR when adjusting the focusing bandwidth and HWC is minimal.

6.5 Experiment 5: Investigation of azimuth burst overlap in TOPS SLC IW₃ data.

The fifth experiment is a brief exploration of the azimuth overlap between two bursts. As mentioned earlier, both target speed and direction can be derived in this area. Due to time constraints the analysis is limited. With focus on the single polarization SCM algorithm, the additional information from the overlap area is used as an alternative combination when two subapertures are considered. A TOPS IW scene from Portsmouth England is used. First the difference in overlap area for TOPS SLC data focused by NRTSAR and ESA IPF is presented. Then the subimages used in this analysis are presented and the experiment stages are explained.

6.5.1 Azimuth burst overlap acquired from focusing with ESA IPF and NRTSAR

ESA IPF focuses the SLC data such that it results in a minimal overlap between two successive bursts. An experiment is done on the prototype NRTSAR where the total bandwidth B_T referring to figure 3.5 is expanded to include the gray shaded areas in the spectrogram. This means that the overlap area in each burst is widened. The overlap area will suffer from not being seen by the total antenna pattern, and thus we expect lower intensities in these areas. Figure 6.32 and 6.33 show two successive burst over the same area, processed by ESA IPF and NRTSAR, respectively. The overlap areas are marked with a yellow rectangle, and cover an area of approximately 2.2 km in azimuth regarding figure 6.32 and approximately 11 km in azimuth regarding 6.33.

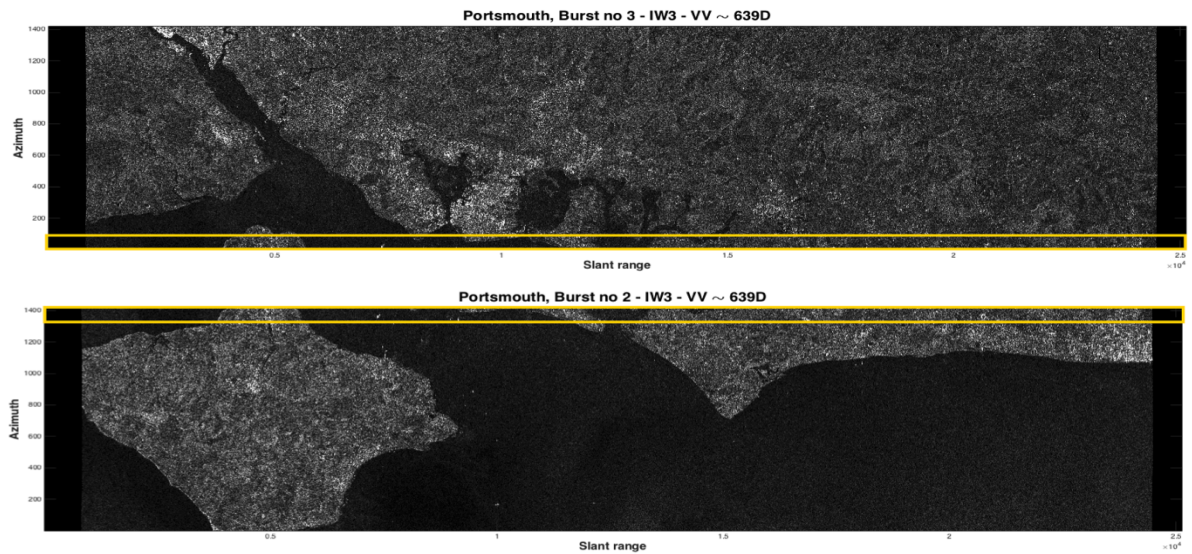


Figure 6.32: Burst no 2 and 3 from IW3 Portsmouth, England, processed with ESA IPF. Overlap area is showed in yellow rectangle. Burst dimension: 1400×25122 pixels. Dimension overlap is approximately 100×25122 pixels, azimuth: 2,2 km

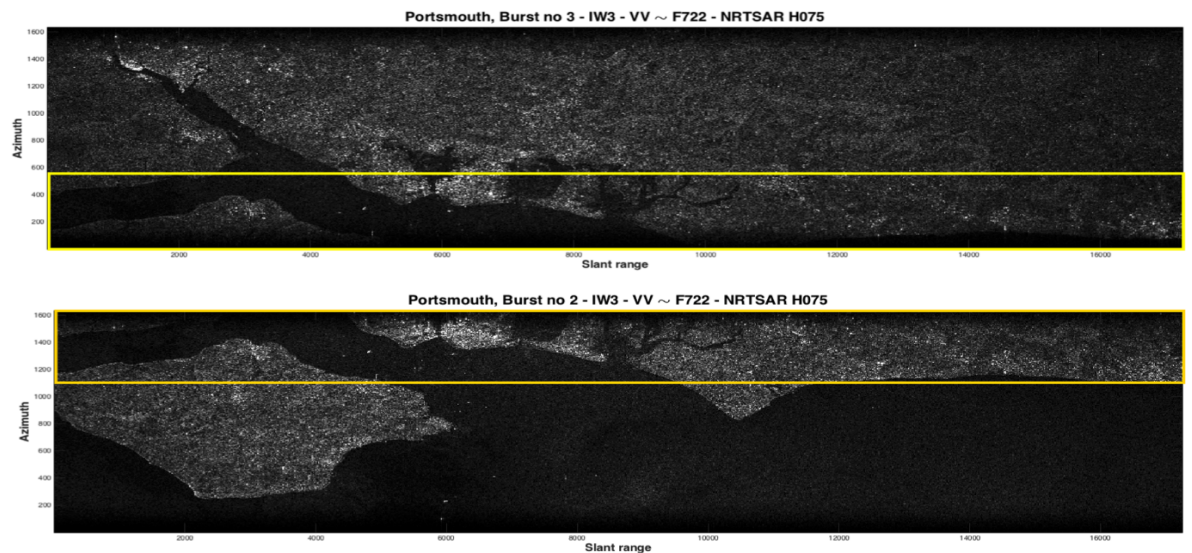


Figure 6.33: Burst no. 2 and 3 from IW3 Portsmouth, England, processed with NRTSAR, showing overlap area in yellow rectangle. Burst dimension: 1600×25122 pixels. Dimension overlap is approximately 500×25122 pixels, azimuth: 11 km

6.5.2 Subaperture cross correlation magnitude on overlap subimages

The overlap areas shown in figure 6.32 and 6.33 cover one of England's most busy ports, a subimage of 130×180 pixels is chosen with high possibility of ship targets. Because the NRTSAR prototype did not yield correct time stamps in azimuth when allowing maximum overlap, the subimage had to be manually selected in each overlap region. The subimage selected from burst no. 2 is denoted as I_1 and the subimage representing burst 3 is denoted as I_2 . Figure 6.34 and 6.35 shows the location of where the subimages are collected. When each polarization is considered, this results in four subimages covering the same scene. Hereafter these subimages are denoted as: $I_{1VV}, I_{1VH}, I_{2VV}$ and I_{2VH} . Here I_{1VV} and I_{1VH} represents the VV and VH channel for subimage acquired from burst no 2, and I_{2VV} and I_{2VH} represents burst no. 3.

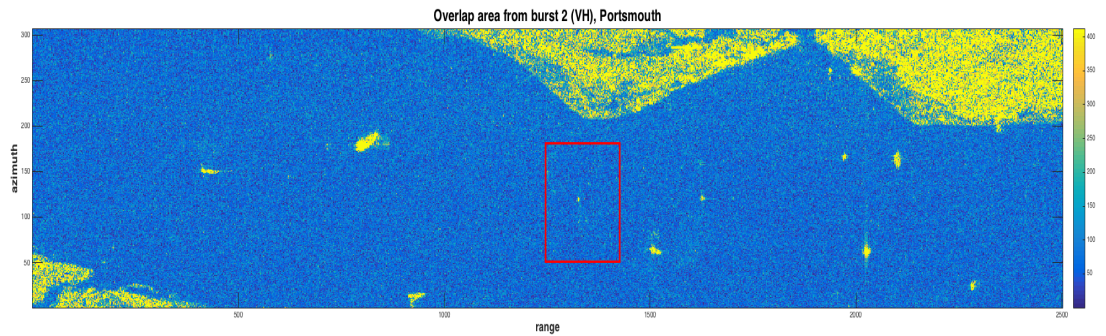


Figure 6.34: Overlap area of burst no. 2 and the selected subimage area is shown in red rectangle.

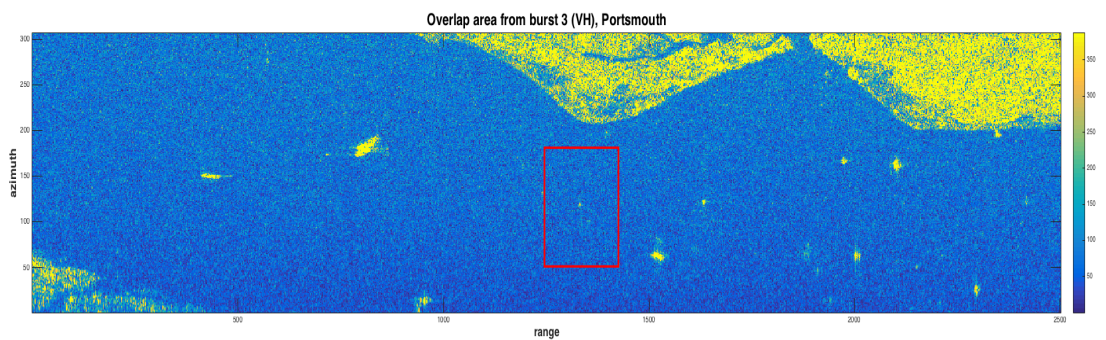


Figure 6.35: Overlap area of burst no. 3 and the selected subimage area is shown in red rectangle.

We want to investigate if computing the cross-correlation magnitude between images from each overlap area will improve the speckle level in the image when computing the SCM images. Intuition tells us that the target displacement will corrupt both TCR and PCR measurements and therefore these computations are omitted. However, the CV measurements yield information about the potential for speckle decorrelation in this area. The analysis is thus divided into the following stages:

- Stage 1: Computing reference images: SCM images are computed for each overlap region separately. The procedure is equivalent to experiment 1.
- Stage 2: SCM images are computed with two subapertures considering each polarization separately and evaluated with CV.

In stage 2, four possible ways of combining subimages exist for each polarization. The combinations are illustrated in figure 6.36. Here we see that 1) and 2) represent the situation where each subaperture is extracted from the left and right with increasing bandwidth. 4) represents the situation where the subaperture from I_1 is extracted from the left and the subaperture from I_2 is extracted from the right. 4) is the opposite situation of 3).

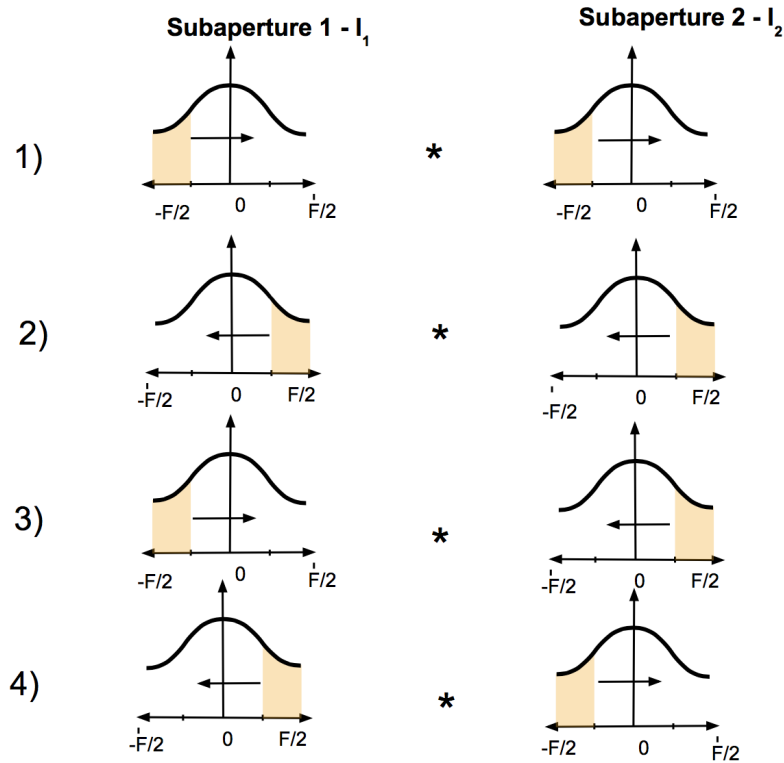


Figure 6.36: Combinations of extracting each subaperture from subimage I_1 and subimage I_2 .

- CV 1) Each subaperture is extracted from the left with increasing size
 2) Each subaperture is extracted from the right with increasing size
 3) Left subaperture from I_1 is combined with right subaperture from I_2
 4) Right subaperture from I_1 is combined with left subaperture from I_2

6.5.3 Speckle measurements in overlap area

Figure 6.37 and 6.38 show how speckle reduces with β when the SCM is computed for each overlap subimage. We observe the same decrease in CV with β as for the previous experiments. Figure 6.39 shows the CV development with β when the SCM-VV was computed with subaperture combination 3) and 4), referring to figure 6.36. Here we observe that the CV does not experience a decay after $\beta \approx 0.7$ as for the reference computations. In this case the subapertures are separated with approximately 2 seconds, and therefore the ΔT is much higher. Hence the correlation is considerably lower compared to the reference.

The results showed that combination 4) with the VV channel provided the lowest CV. This occurred for $\beta = 0.81$, but in comparison with the reference

CV, an improvement is not observed. When examining the various surface plots for increasing β a nearly flat area was observed in the low azimuth, meaning in the lower part of the subimage. This effect were observed for both polarizations but only when extracting the subapertures with combination 3) with $\beta \in [0.01 - 0.3]$. Figure 6.40 shows the mean amplitude profile in azimuth direction. We observe that the flat area is obscured with increasing β . This could be the combination of low resolution and that the overlap area suffers from low intensity. However, since this effect did not occur with the other subaperture extraction combinations, the time spacing between the subapertures may play a role, and thus the possibility that larger ocean waves might have decorrelated is also present.

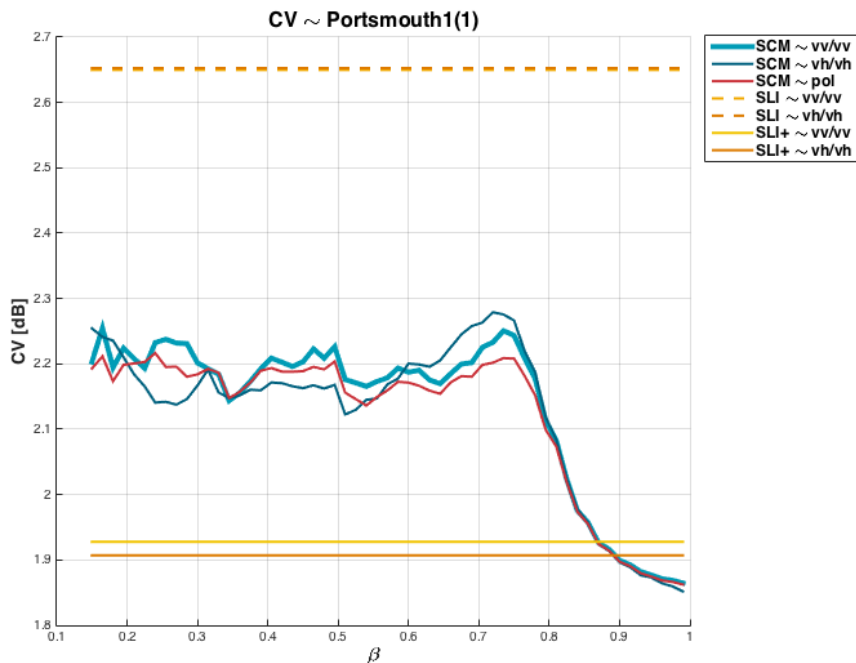


Figure 6.37: CV measurements from overlap subimage I_1 .

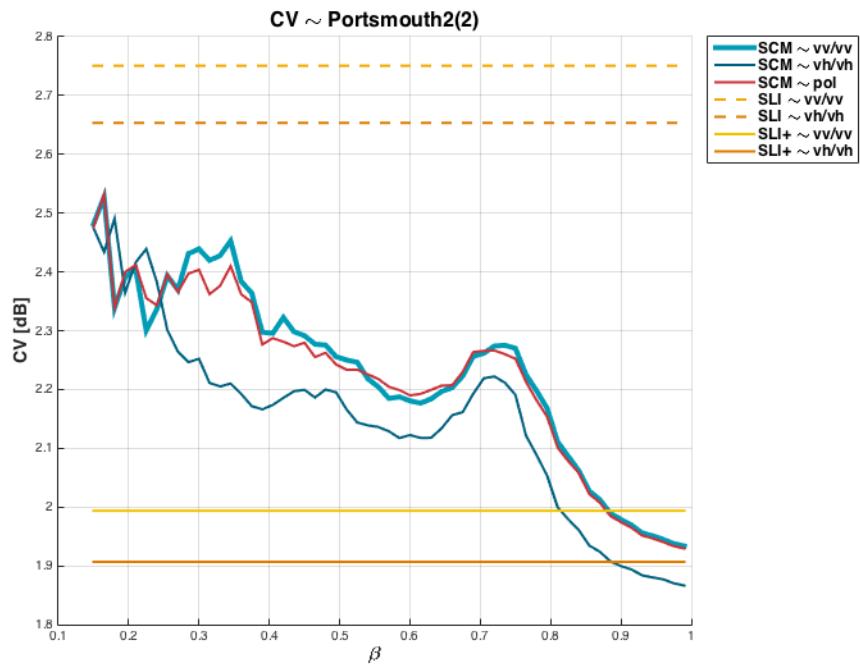


Figure 6.38: CV measurements from overlap subimage I_2 .

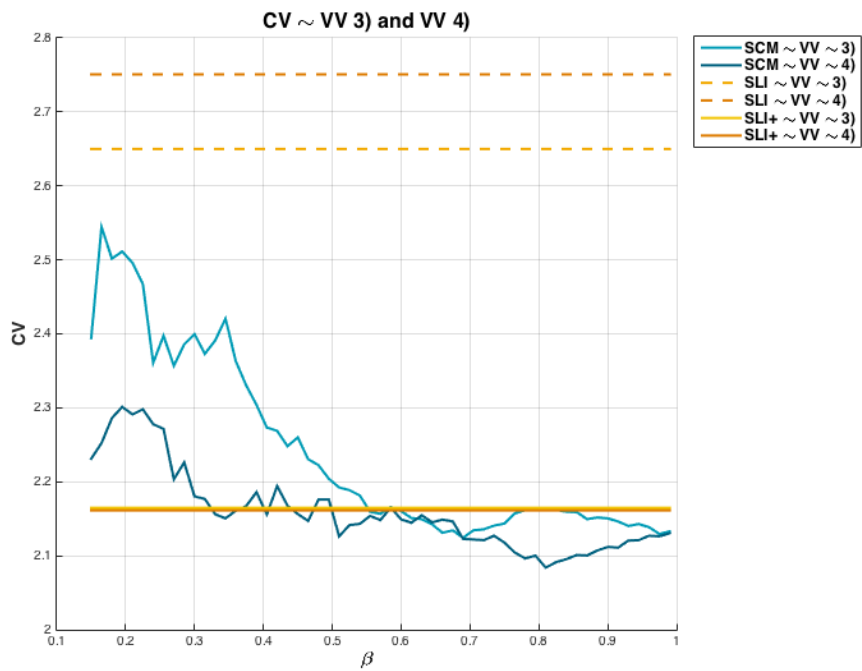


Figure 6.39: CV measurements from SCM-VV computations from combination 3) and 4). Lowest CV value occurred for $\beta = 0.81$.

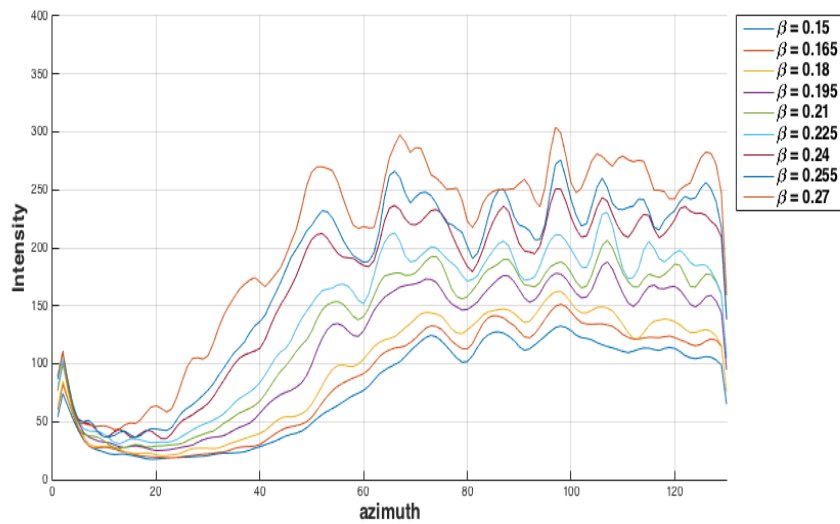


Figure 6.40: Intensity profile in azimuth for SCM-VV image from subaperture extraction combination number 3.



Conclusions

This chapter concludes the findings in this thesis and gives suggestions about future work. This thesis had two overall goals. Number one was to investigate how contrast enhancement algorithms suitable for SLC data can be adapted to complex data acquired in TOPS mode. The second goal was to investigate if processing the TOPS raw data with a different focusing scheme will affect the performance of the algorithms.

The analysis in this thesis showed that all contrast enhancement algorithms were adaptable to SLC data in TOPS mode. The polarimetric extension of the SCM proposed by Souyris et al.[2] were adjusted to fit the dual polarization case with the VV- and VH channel. This adjustment was incorporated in the improved SCM algorithm from Brekke et al.[1], and denoted as SCM-POL. A *prewhitening* of the frequency spectra were performed in conjunction with the extraction of the subapertures. The results showed that the prewhitening had a minor effect on the TCR, PCR and CV.

In conjunction with the theory that speckle decorrelates in relation to the ocean coherence time, the TOPS SLC dwell time in this thesis was in the range 0.03 – 0.04 s. In general, studies have shown that open ocean needs 0.05 s or less to decorrelate for C-band SAR. However a direct association with the sea state can not be made due to lack of weather data. The focusing bandwidth was increased, and consequently the time separation between the subapertures increased as well. Minor differences to the TCR and PCR were observed but no firm conclusion about the dependency of the sea state can be made.

Overall the SCM-VH images gave the highest TCR and PCR. However situations were the SCM-POL yielded highest TCR and PCR also occurred. The SCM images were compared to other contrast enhancement products obtained from the PWF and Aegir-Pol algorithm. In this relation the SCM images yielded highest TCR for all subimages evaluated. The algorithm which gave the highest PCR varied between the SCM algorithm and Aegir-Pol algorithm.

TOPS SLC data were processed by NRTSAR with adjustable processing parameters with respect to window function and focusing bandwidth. The window function was chosen to be a Hamming window, with three different coefficients, and three focusing bandwidths were used.

The SCM image products experienced a minor increase in TCR and PCR with increasing bandwidth.

This means that better SCM products can be processed by fine tuning the focusing bandwidth. The results also indicated that the choice of HWC in the context of TCR and PCR had more effect for lower bandwidths. No particular trend was observed for the PWF and the Aegir-POL products. The SCM image gave the highest TCR and PCR when compared to the PWF and Aegir-Pol products. The results showed that overall, a normalized subaperture overlap with $\beta \approx 0.7$ gave optimal TCR and PCR. Thus:

The SCM-VH image and SCM-POL image with $\beta \approx 0.7$ is further recommended as suitable ship detection products for TOPS SLC data.

Lastly an investigation of the azimuth burst overlap in TOPS SLC data were evaluated. The additional information from the overlap area was used as an alternative combination when two subapertures were considered for the single polarization SCM. No improvement of CV were observed.

7.1 Further work

This thesis evaluated image products suitable for ship detection. These image products may serve as a test statistic in future ship detection. Further work should concern modeling the ocean background and derive test hypothesis for these particular products. The superiority of the SCM approach over conventional CFAR should also be stated by comparing detection results with CFAR applied to the original products.

Further improvements of the SCM algorithms should also be studied. Here the lowpass filter used when subapertures overlap needs an evaluation. The latest research have shown that a subaperture approach which detects coherent targets, named the *generalized likelihood ratio test* GLRT have yielded *better* target detection results than the SCM approach. In this study the GLRT were processed with 30 subapertures with 96% overlap. This was compared to a SCM algorithm with two subapertures with a small overlap were used [64][65]. Therefore the SCM-VH and SCM-POL with a small overlap, e.g., $\beta = 0.7$ should be compared to the GLRT algorithm.

The overlap area between the burst should be investigated further, both in range and azimuth. The possibility of using the overlap area as an *additional* subaperture, and incorporate it in the SCM-POL should also be investigated. Speed and heading of ship can be studied aswell as information about the ocean conditions in this area. A threshold for how much overlap yields useful information should also be set in order to optimize the processing time for NRTSAR.

Bibliography

- [1] C. Brekke, S. N. Anfinsen, and Y. Larsen, "Subband extraction strategies in ship detection with the subaperture cross-correlation magnitude," *Geoscience and Remote Sensing Letters, IEEE*, vol. 10, no. 4, pp. 786–790, 2013.
- [2] J.-C. Souyris, C. Henry, and F. Adragna, "On the use of complex sar image spectral analysis for target detection: Assessment of polarimetry," *Geoscience and Remote Sensing, IEEE Transactions on*, vol. 41, no. 12, pp. 2725–2734, 2003.
- [3] J. Tournadre, "Anthropogenic pressure on the open ocean: The growth of ship traffic revealed by altimeter data analysis," *Geophysical Research Letters*, vol. 41, no. 22, pp. 7924–7932, 2014.
- [4] B. S. Halpern, S. Walbridge, K. A. Selkoe, C. V. Kappel, F. Micheli, C. D'Agrosa, J. F. Bruno, K. S. Casey, C. Ebert, H. E. Fox, *et al.*, "A global map of human impact on marine ecosystems," *Science*, vol. 319, no. 5865, pp. 948–952, 2008.
- [5] R. Torres, P. Snoeij, D. Geudtner, D. Bibby, M. Davidson, E. Attema, P. Potin, B. Rommen, N. Floury, M. Brown, *et al.*, "Gmes sentinel-1 mission," *Remote Sensing of Environment*, vol. 120, pp. 9–24, 2012.
- [6] Z. Malenovsky, H. Rott, J. Cihlar, M. E. Schaepman, G. García-Santos, R. Fernandes, and M. Berger, "Sentinels for science: Potential of sentinel-1, -2, and -3 missions for scientific observations of ocean, cryosphere, and land," *Remote Sensing of Environment*, vol. 120, pp. 91–101, 2012.
- [7] "Sentinel esa homepage:
<https://sentinel.esa.int/web/sentinel/home>," December 2014.
- [8] H. Greidanus and C. Santamaria, "First analyses of sentinel-1 images for maritime surveillance:
<http://publications.jrc.ec.europa.eu/repository/bitstream/jrc92666/lbna2>

7031enn.pdf,” 2014.

- [9] “Logo sentinel-1:
http://download.esa.int/multimedia/mission_logos/eo/sentinel-1_logo/sentinel-1.jpg,” May 2015.
- [10] E. Chuvieco, A. Huete, *et al.*, *Fundamentals of Satellite Remote Sensing*. Taylor and Francis Group, LLC, 2010.
- [11] C. Elachi and J. J. Van Zyl, *Introduction to the physics and techniques of remote sensing*, vol. 28. John Wiley & Sons, second ed., 2006.
- [12] I. G. Cumming and F. H. Wong, *Digital processing of synthetic aperture radar data: algorithms and implementation*. Artech House, 1 ed., 2005.
- [13] C. Wu, “A digital system to produce imagery from sar data,” in *Proc. of the AIAA Systems Design Driven by Sensors Conference*, p. 6, 1976.
- [14] I. Cumming and J. R. Bennett, “Digital processing of seasat sar data,” in *Acoustics, Speech, and Signal Processing, IEEE International Conference on ICASSP’79.*, vol. 4, pp. 710–718, IEEE, 1979.
- [15] C. Thain, “Sentinel-1 detailed algorithm definition:
<https://sentinel.esa.int/documents/247904/349449/sentinel-1+level-1+detailed+algorithm+definition+1.6/a75d3699-95f9-4bc4-9901-ba2f207ef513;jsessionid=7ec6c82a06045f308478f1447e971b40.eodisp-prod4040?version=1.3>,” March 28 2014.
- [16] J.-S. Lee and E. Pottier, *Polarimetric radar imaging: from basics to applications*. CRC Press, Taylor & Francis Group, 2009.
- [17] “Fundamentals of remote sensing, natural resources canada, tutorial:
<http://www.nrcan.gc.ca/earth-sciences/geomatics/satellite-imagery-air-photos/satellite-imagery-products/educational-resources/9311>,” December 2014.
- [18] R. Moore, J. Claassen, and Y. Lin, “Scanning spaceborne synthetic aperture radar with integrated radiometer,” *Aerospace and Electronic Systems, IEEE Transactions on*, vol. 17, no. 3, pp. 410–420, 1981.
- [19] F. De Zan and A. Monti Guarnieri, “Topsar: Terrain observation by progressive scans,” *Geoscience and Remote Sensing, IEEE Transactions on*, vol. 44, no. 9, pp. 2352–2360, 2006.

- [20] A. Currie and M. A. Brown, "Wide-swath sar," in *IEE Proceedings F (Radar and Signal Processing)*, vol. 139, pp. 123–135, IET, April 1992.
- [21] W. Yang, J. Chen, H. Zeng, J. Zhou, P. Wang, and C.-S. Li, "A novel three-step image formation scheme for unified focusing on spaceborne sar data," *Progress In Electromagnetics Research*, vol. 137, pp. 621–642, 2013.
- [22] C. Prati, A. M. Guarnieri, and F. Rocca, "Spot mode sar focusing with the ω -k technique," *Proceedings of the 1991 IEEE International Geoscience and Remote Sensing Symposium (IGARSS)*, pp. 631–634, 1991.
- [23] P. Prats, R. Scheiber, J. Mittermayer, A. Meta, A. Moreira, and J. Sanz-Marcos, "A sar processing algorithm for tops imaging mode based on extended chirp scaling," in *Geoscience and Remote Sensing Symposium, 2007. IGARSS 2007. IEEE International*, pp. 148–151, IEEE, 2007.
- [24] G. Engen and Y. Larsen, "Efficient full aperture processing of tops mode data," in *Synthetic Aperture Radar (EUSAR), 2010 8th European Conference on*, vol. 49, pp. 1–4, VDE, October 2010.
- [25] A. Meta, P. Prats, U. Steinbrecher, J. Mittermayer, and R. Scheiber, "Terrasar-x topsar and scansar comparison," in *Synthetic Aperture Radar (EUSAR), 2008 7th European Conference on*, pp. 1–4, VDE, 2008.
- [26] "Esa webpage:
<https://earth.esa.int/handbooks/asar/cnr5-2.htm>," May 2015.
- [27] F. J. Harris, "On the use of windows for harmonic analysis with the discrete fourier transform," *Proceedings of the IEEE*, vol. 66, no. 1, pp. 51–83, 1978.
- [28] G. Thomas, B. C. Flores, and J. Sok-Son, "Sar sidelobe apodization using the kaiser window," in *Image Processing, 2000. Proceedings. 2000 International Conference on*, vol. 1, pp. 709–712, IEEE, 2000.
- [29] J. Li and P. Stoica, "An adaptive filtering approach to spectral estimation and sar imaging," *Signal Processing, IEEE Transactions on*, vol. 44, no. 6, pp. 1469–1484, 1996.
- [30] G. Engen, Y. Larsen, and G. L. Rasmussen, "Summary report, extension of eetf for tops mode," Tech. Rep. ESTEC-FR-KSPT-TOPS-8134, Kongsberg Spaceteq AS, June 2009.
- [31] "Mda product description:
http://gs.mdacorporation.com/products/sensor/radarsat2/rs2_product

_description.pdf,” 5 MAY 2014.

- [32] E. N. Miranda, “Esa-mission overview: http://earth.eo.esa.int/pub/polsarpro_ftp/radarpol_course11/wednesday19/sentinel-1_overview.pdf,” 2013.
- [33] nuno miranda, “Definition of the tops slc deramping function for products generated by the s-1 ipf.,” January 2014.
- [34] P. Prats and M. Rodrigues-Cassola, “Investigations with sentinel-1 iw data: http://seom.esa.int/insarap/files/insarap-2014_investigations_with_sentinel-1_iw.pdf,” December 2014.
- [35] D. J. Crisp, “The the state-of-the-art in ship detection in synthetic aperture radar imagery,” tech. rep., DTIC Document, 2004.
- [36] P. Vachon, J. Campbell, C. Bjerkelund, F. Dobson, and M. Rey, “Ship detection by the radarsat sar: Validation of detection model predictions,” *Canadian Journal of Remote Sensing*, vol. 1, no. 23, pp. 48–59, 1997.
- [37] I. S. Robinson, *Satellite oceanography: an introduction for oceanographers and remote-sensing scientists*. Chichester, UK: Ellis Horwood Ltd, 1985.
- [38] J. van der Sanden, P. Budkewitsch, D. Flett, R. Landry, T. Lukowski, H. McNairn, T. Pultz, V. Singhroy, J. Sokol, R. Touzi, *et al.*, “Applications potential of planned c-band sar satellites: leading to radarsat-2,” in *Geoscience and Remote Sensing Symposium, 2001. IGARSS’01. IEEE 2001 International*, vol. 1, pp. 488–492, IEEE, 2001.
- [39] C. Howell, J. Youden, K. Lane, D. Power, C. Randell, and D. Flett, “Iceberg and ship discrimination with envisat multipolarization asar,” in *Geoscience and Remote Sensing Symposium, 2004. IGARSS ’04. Proceedings. 2004 IEEE International*, vol. 1, 2004.
- [40] M. I. Skolnik, *Introduction to radar. Radar Handbook 2*, vol. 2. 1962.
- [41] M. Jeremy, J. Campbell, K. Mattar, and T. Potter, “Ocean surveillance with polarimetric sar,” *Canadian Journal of Remote Sensing*, vol. 27, no. 4, 2001.
- [42] P. W. Vachon and J. Wolfe, “Validation of ship signatures in envisat asar ap mode data using aislive,” tech. rep., 2008.
- [43] C. Brekke and S. N. Anfinsen, “Ship detection in ice-infested waters based

- on dual-polarization sar imagery,” *Geoscience and Remote Sensing Letters, IEEE*, vol. 8, no. 3, 2011.
- [44] L. L. Scharf, *Statistical signal processing*, vol. 98. Addison-W, 1991.
- [45] C. Oliver and S. Quegan, *Understanding synthetic aperture radar images*. SciTech Publishing, 2004.
- [46] H. Rohling, “Radar cfar thresholding in clutter and multiple target situations,” *Aerospace and Electronic Systems, IEEE Transactions on*, pp. 608–621, July 1983.
- [47] D. Tao, S. N. Anfinsen, and C. Brekke, “A ship detection algorithm based on truncated statistics,” in *EUSAR 2014; 10th European Conference on Synthetic Aperture Radar; Proceedings of*, pp. 1–4, VDE, 2014.
- [48] S. N. Anfinsen and C. Brekke, “Statistical models for constant false alarm rate ship detection with the sublook correlation magnitude,” *IEEE, IGARSS*, pp. 5626–5629, 2012.
- [49] A. Arnaud, “Ship detection by sar interferometry,” *IEEE*, 1999.
- [50] K. Ouchi, S. Tamaki, H. Yaguchi, and M. Iehara, “Ship detection based on coherence images derived from cross correlation of multilook sar images,” *IEEE GEOSCIENCE AND REMOTE SENSING LETTERS*, vol. 1, no. 3, pp. 184–187, 2004.
- [51] C. Henry, J.-C. Souyris, and P. Marthon, “Target detection and analysis based on spectral analysis of a sar image: A simulation approach,” in *INTERNATIONAL GEOSCIENCE AND REMOTE SENSING SYMPOSIUM*, vol. 3, 2003.
- [52] H. Johnsen and Y. L. Larsen, “A novel method for spaceborne sar vessel detection using complex radar backscatter,” tech. rep., Norut Informasjonsteknologi AS, European Space Agency, 2006.
- [53] S. R. Cloude and K. P. Papathanassiou, “Polarimetric sar interferometry,” *Geoscience and Remote Sensing, IEEE Transactions on*, vol. 36, no. 5, pp. 1551–1565, 1998.
- [54] L. M. Novak and M. C. Burl, “Optimal speckle reduction in polarimetric sar imagery,” *Aerospace and Electronic Systems, IEEE Transactions on*, vol. 26, no. 2, pp. 293–305, 1990.

- [55] T. N. A. Hannevik, "Multi-channel and multi-polarisation ship detection," in *Geoscience and Remote Sensing Symposium (IGARSS), 2012 IEEE International*, pp. 5149–5152, 2012.
- [56] E. K. H. O. B. C. B. Olsen, Richard, "Analysis of options for mariss services extension," mariss-report, mariss-ffi-tn2-tn-015, FFI, 2009.
- [57] P. W. Vachon, J. Wolfe, and H. Greidanus, "Analysis of sentinel-1 marine applications potential," in *Geoscience and Remote Sensing Symposium (IGARSS), 2012 IEEE International*, pp. 1734–1737, IEEE, July 2012.
- [58] K. Ouchi and H. Wang, "Interlook cross-correlation function of speckle in sar images of sea surface processed with partially overlapped subapertures," *Geoscience and Remote Sensing, IEEE Transactions on*, vol. 43, no. 4, pp. 695–701, 2005.
- [59] E. S. Online, "https://sentinel.esa.int/web/sentinel/user-guides/sentinel-1-sar/acquisition-modes/interferometric-wide-swath," December 2014.
- [60] M. Aular-Macher, "Sentinel-1 product definition: http://ec.europa.eu/researchparticipantsportal4doccallfp7/fp7-space-2012-131656-s1-rs-md-a-52-7440product_definition_2_3_en.pdf," March 2011.
- [61] N. Miranda, "Sentinel-1 mission overview: https://earth.esa.int/documents/10174/669756/sentinel-1_system_data.pdf/a3a56776-9cbb-487a-94a9-11bd20579d79."
- [62] ESA, "Esa scientific data hub, <https://scihub.esa.int/dhus/>."
- [63] D. Tao, S. N. Anfinsen, and C. Brekke, "A comparative study of sea clutter covariance matrix estimators," *Geoscience and Remote Sensing Letters, IEEE*, vol. 11, no. 5, pp. 1010–1014, 2014.
- [64] A. Marino, M. J. Sanjuan-Ferrer, I. Hajnsek, and K. Ouchi, "Ship detection with spectral analysis of synthetic aperture radar: A comparison of new and well-known algorithms," *Remote Sensing*, vol. 7, no. 5, pp. 5416–5439, 2015.
- [65] A. Marino, M. J. Sanjuan-Ferrer, I. Hajnsek, and K. Ouchi, "Ship detectors exploiting spectral analysis of sar images," in *Geoscience and Remote Sensing Symposium (IGARSS), 2014 IEEE International (978-981, ed.)*, IEEE, 2014.

/ 8

Appendix

8.1 Graphical representation of the correlation between the time-frequency support and aquisition geometry, TOPS

The "explanation" of the TFD support slope marked in red in figure 8.1 is that when the radar is moving in opposite direction to where the antenna is pointing this induces negative frequency f_- , and when the antenna is pointing in the same direction as the radar, the frequency is positive f_- . Regarding the doppler histories for each target marked in orange, the doppler shift is positive f_+ as the radar approaches P, it then decreases to zero and becomes negative f_- when the radar is moving away.

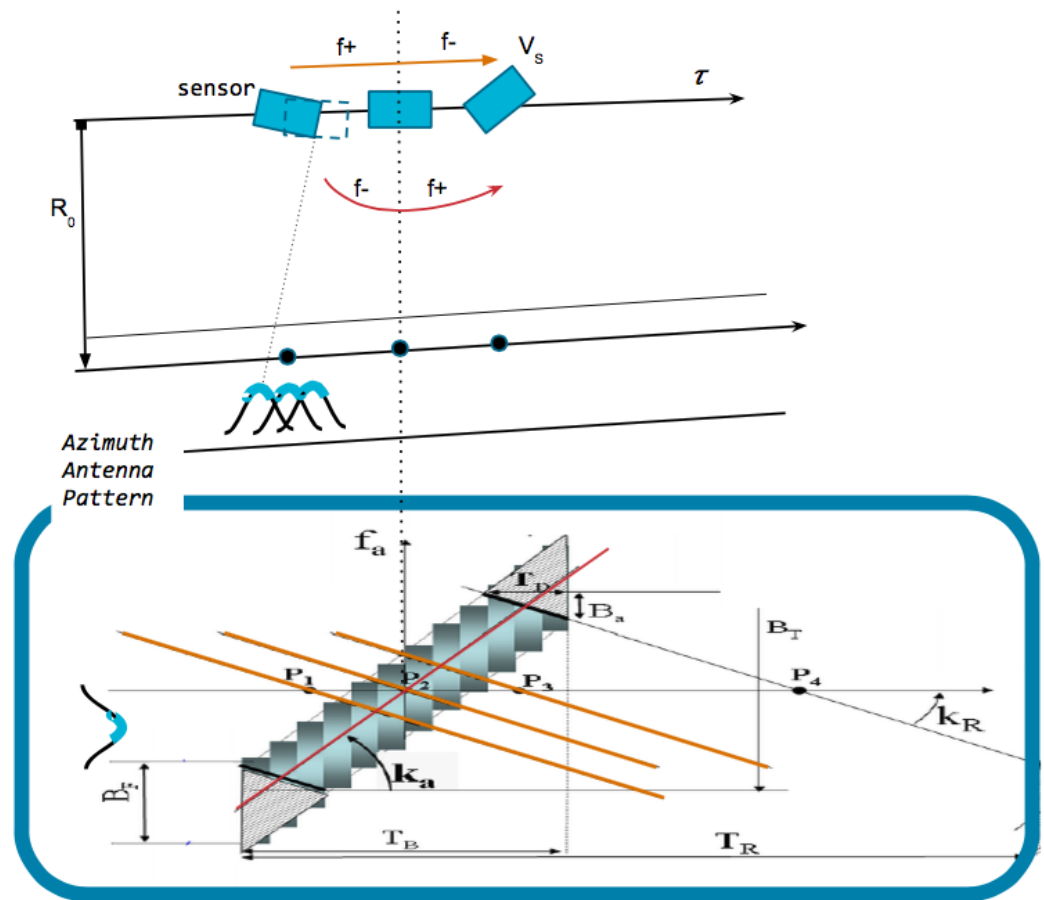


Figure 8.1: Graphical representation of the correlation between figure 3.3 and 3.5

8.2 Target to clutter ratio and peak to clutter ratio computed with target vectors from Pauli baseses

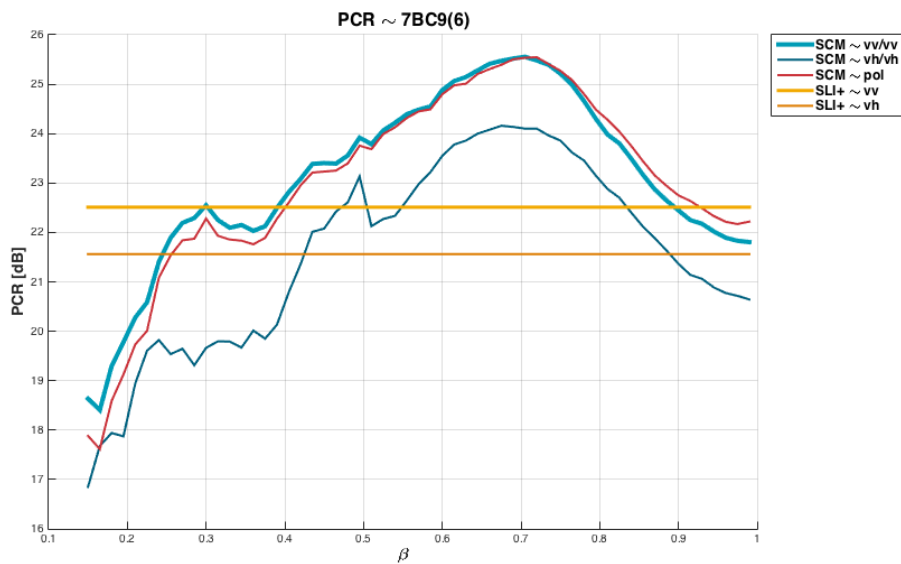


Figure 8.2: Peak to clutter ratio computed with target vectors from Pauli baseses. Peak to clutter ratio for SCM-POL is unchanged compared to Lexciographic based target vectors.

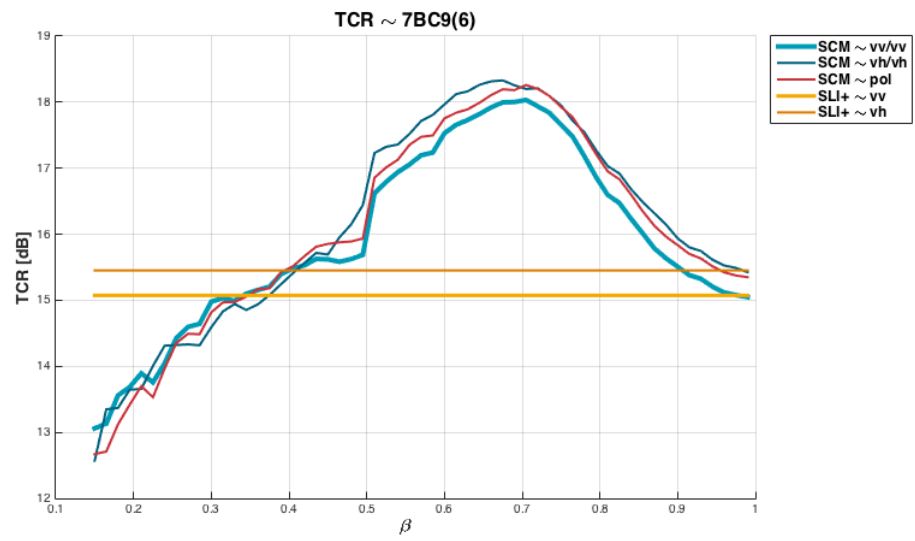


Figure 8.3: Target to clutter ratio computed with target vectors from Pauli bases. Target to clutter ratio is lowered compared to Lexicographic based target vectors.

8.3 Subaperture cross correlation magnitude impact of varying processing bandwidth and Hamming window coefficient.

SCM _{MAX} ~ Im 1												
HWC	373 [Hz]				350 [Hz]				327 [Hz]			
	TCR [dB]	β	PCR [dB]	β	TCR [dB]	β	PCR [dB]	β	TCR [dB]	β	PCR [dB]	β
0.75	22.3136	0.750	33.7183	0.750	22.3291	0.750	33.7456	0.735	22.0820	0.765	33.5729	0.750
0.65	22.3463	0.750	33.7886	0.750	22.8108	0.735	33.8372	0.735	22.2646	0.750	33.6932	0.750
0.5	22.4664	0.750	33.8254	0.750	22.4960	0.735	33.8198	0.735	22.4956	0.735	33.7292	0.750

Table 8.1: Subaperture cross correlation magnitude, TCR and PCR when varying Hamming window coefficient and bandwidth, representing subimage 1.

Aegir-Pol ~ Im 1						
HWC	373 [Hz]		350 [Hz]		327 [Hz]	
	TCR [dB]	PCR [dB]	TCR [dB]	PCR [dB]	TCR [dB]	PCR [dB]
0.75	15.0456	29.1996	15.0298	29.1536	15.1756	29.3086
0.65	15.2711	29.5317	15.5533	29.5423	15.3398	29.4275
0.5	15.5250	29.8328	15.5377	29.8428	15.6336	29.5526

Table 8.2: Aegir-POL, TCR and PCR when varying Hamming window coefficient and bandwidth, representing subimage 1.

PWF ~ Im 1						
HWC	373 [Hz]		350 [Hz]		327 [Hz]	
	TCR [dB]	PCR [dB]	TCR [dB]	PCR [dB]	TCR [dB]	PCR [dB]
0.75	8.8809	23.7789	8.8538	23.7199	8.8520	23.7406
0.65	8.8967	23.6554	9.1642	23.5737	8.8601	23.5895
0.5	8.9047	23.3213	8.8583	23.2301	8.8750	23.2021

Table 8.3: PWF, TCR and PCR when varying Hamming window coefficient and bandwidth, representing subimage 1.

SCM _{MAX} ~ Im 13												
HWC	373 [Hz]				340 [Hz]				313 [Hz]			
	TCR [dB]	β	PCR [dB]	β	TCR [dB]	β	PCR [dB]	β	TCR [dB]	β	PCR [dB]	β
0.75	23.7205	0.720	31.7745	0.720	23.6840	0.720	31.6695	0.720	23.7457	0.705	31.3452	0.705
0.65	23.7522	0.720	31.7594	0.720	23.7007	0.720	31.6293	0.720	23.7345	0.705	31.2160	0.705
0.5	23.7256	0.720	31.5764	0.720	23.6498	0.705	31.3621	0.705	23.3076	0.660	30.0312	0.675

Table 8.4: Subaperture cross correlation magnitude, PCR and TCR when varying Hamming window coefficient and bandwidth, representing subimage 13.

Aegir-Pol ~ Im 13						
HWC	373 [Hz]		340 [Hz]		313 [Hz]	
	TCR [dB]	PCR [dB]	TCR [dB]	PCR [dB]	TCR [dB]	PCR [dB]
0.75	18.3077	30.7331	18.3512	30.6540	18.4077	30.6373
0.65	18.4355	30.8868	17.4454	30.7150	18.5085	30.9797
0.5	18.6017	30.9985	18.6406	30.9733	18.6748	31.0095

Table 8.5: Aegir-Pol, PCR and TCR when varying Hamming window coefficient and bandwidth, representing subimage 13.

PWF ~ Im 13						
HWC	373 [Hz]		340 [Hz]		313 [Hz]	
	TCR [dB]	PCR [dB]	TCR [dB]	PCR [dB]	TCR [dB]	PCR [dB]
0.75	8.8462	20.2579	8.8117	20.1504	8.7931	20.1930
0.65	8.8031	20.2424	8.8089	20.1964	8.7279	20.2390
0.5	8.7386	20.4919	8.7111	20.4936	8.6882	20.5126

Table 8.6: PWF, PCR and TCR when varying Hamming window coefficient and bandwidth, representing subimage 13.

SCM _{MAX} ~ Im 18												
HWC	373 [Hz]				340 [Hz]				314 [Hz]			
	TCR [dB]	β	PCR [dB]	β	TCR [dB]	β	PCR [dB]	β	TCR [dB]	β	PCR [dB]	β
0.75	31.2656	0.750	38.1306	0.750	30.7679	0.765	37.9707	0.735	30.4817	0.750	37.8961	0.750
0.65	31.3007	0.750	38.1449	0.735	30.8176	0.750	38.0038	0.735	30.4433	0.735	37.9093	0.735
0.5	31.2683	0.750	38.0460	0.735	30.8179	0.735	37.9255	0.735	30.5444	0.735	37.9111	0.735

Table 8.7: Subaperture cross correlation magnitude, TCR and PCR when varying Hamming window coefficient and bandwidth, representing subimage 18.

Aegir-Pol ~ Im 18						
HWC	373 [Hz]		340 [Hz]		314 [Hz]	
	TCR [dB]	PCR [dB]	TCR [dB]	PCR [dB]	TCR [dB]	PCR [dB]
0.75	25.1350	34.4555	24.9426	34.4036	24.2866	34.3486
0.65	25.2495	34.4170	25.0526	34.2787	24.4333	34.2483
0.5	25.3842	34.1056	25.1816	33.9718	24.5793	33.9524

Table 8.8: Aegir, TCR and PCR when varying Hamming window coefficient and bandwidth, representing subimage 18.

PWF ~ Im 18						
HWC	373 [Hz]		340 [Hz]		314 [Hz]	
	TCR [dB]	PCR [dB]	TCR [dB]	PCR [dB]	TCR [dB]	PCR [dB]
0.75	12.5338	21.7281	12.5428	21.7578	11.9686	21.7521
0.65	12.5799	21.6791	12.5822	21.7034	12.7435	21.0575
0.5	12.6479	21.8783	12.6314	21.9128	12.1190	21.9563

Table 8.9: PWF, TCR and PCR when varying Hamming window coefficient and bandwidth, representing subimage 18.

